THESIS FOR THE DEGREE OF DOCTOR OF PHILOSOPHY

Unlocking Graphene Functionalization: Synthesis of Photo- and Redox-Active Pyrene Derivatives for Advanced Energy Storage and Optoelectronic Applications

Cheng Peng

Department of Chemistry and Chemical Engineering

CHALMERS UNIVERSITY OF TECHNOLOGY

Gothenburg, Sweden 2025

Unlocking Graphene Functionalization: Synthesis of Photo- and Redox-Active Pyrene Derivatives for Advanced Energy Storage and Optoelectronic Applications

CHENG PENG

ISBN: 978-91-8103-171-3

Doktorsavhandlingar vid Chalmers tekniska högskola

Ny serie nr 5629

ISSN: 0346-718X

Department of Chemistry and Chemical Engineering

Chalmers University of Technology

SE-412 96 Gothenburg

Sweden

Telephone + 46 (0)31-772 1000

Cover: *Unlocking graphene functionalization*

Printed by Chalmers digitaltryck

Gothenburg, Sweden 2025

Unlocking Graphene Functionalization: Synthesis of Photo- and Redox-Active Pyrene Derivatives for Advanced Energy Storage and Optoelectronic Applications

Cheng Peng

Department of Chemistry and Chemical Engineering

Chalmers University of Technology

Abstract

The unique properties of two-dimensional (2D) materials, particularly graphene, have garnered significant research interest across various interdisciplinary fields and hold promise for applications in areas such as field-effect transistors, biological systems, water purification, and energy storage devices. Functionalizing graphene mitigates its tendency to reaggregate, while introducing functional groups imparts new properties, effectively expanding the range of its applications. It has proven to be a powerful strategy for enhancing graphene's versatility and potential across diverse technological domains.

The extensive use of fossil fuels has led to significant environmental challenges and raised concerns over the depletion of fossil energy resources, highlighting the urgent need for sustainable alternative energy sources. Lithium-ion batteries (LIBs), widely used as primary energy storage devices in daily life, offer the advantage of high energy density. However, their application in large-scale energy storage is constrained by limitations in power density, safety concerns, and reliance on finite resources. Aqueous supercapacitors incorporating 2D materials present a promising solution to these challenges. In this thesis, we have developed aqueous supercapacitors using pyrenetetraone derivative-functionalized graphene as cathode materials and thermal treated $Ti_3C_2T_x$ as the anode material. The as-assembled supercapacitor can deliver an excellent energy density of 38.1 Wh kg^{-1} at a power density of 950 W kg^{-1}. Moreover, various spectroscopic analyses reveal distinct interaction behaviors among differently functionalized 2D materials, offering valuable insights for the development of organic-based electrode materials.

In addition, donor-acceptor (D-A) systems based on pyrenetetraone derivatives have been designed and synthesized for the noncovalent functionalization of graphene. The interaction between the D-A molecules and graphene was studied using different characterization techniques. The structure–property relationship in the nonlinear optical response of the hybrids will be further explored.

Keywords: 2D materials, graphene, organic functionalization, aqueous energy storage, optoelectronics, nonlinear optics

List of publications

This thesis is based on the following publications:

I. A Novel Aqueous Asymmetric Supercapacitor based on Pyrene-4,5,9,10-Tetraone Functionalized Graphene as the Cathode and Annealed $Ti_3C_2T_x$ MXene as the Anode.
M. Shi, C. Peng, X. Zhang
Small. **2023**, 19, 2301449.

II. Aqueous Asymmetric Supercapacitors with Pyrenetetraone-Derived Pseudocapacitive Polymer-Functionalized Graphene Cathodes Enabling a 1.9 V Operating Window.
C. Peng, C. Guo, Y. Wang, Y. Li, X. Zhang
Adv. Energy Sustainability Res. **2024**, 5, 2300217.

Publication by the author not included in the thesis:
Chemical Functionalization of Graphene Nanoplatelets with Hydroxyl, Amino, and Carboxylic Terminal Groups.
C. Peng, X. Zhang
Chemistry. **2021**, 3, 873-888.

Contribution report

Paper I: Synthesis of pyrenetetraone, XPS, and SEM measurements of the resulting nanocomposites.

Paper II: Synthesis of the polymers, characterization of the materials, fabrication and electrochemical tests of the electrodes and full-cell devices, data analysis, and manuscript drafting. Theory calculations were performed by the collaborator.

Chapter 4: Synthesis, characterization, and purification of the D-A molecules, preparation of graphene, steady-state photophysical measurements, and experimental data analysis.

Table of Contents

Abbreviations

ASC	Asymmetric supercapacitor
EES	Electrical energy storage
EDLC	Electric double-layer capacitor
NLO	Nonlinear optics
GO	Graphene oxide
rGO	Reduced graphene oxide
CV	Cyclic voltammetry
GCD	Galvanostatic charge-discharge
PAH	Polycyclic aromatic hydrocarbon
PYT	4,5,9,10-pyrenetetraone

1. Introduction and background of graphene and pyrene derivatives

1.1 Graphene:

Carbon is one of the 14 elements that was known before the scientific revolution. It is the 15th most abundant element in the earth's crust and the fourth most abundant element in the observable universe. Carbon also serves as a common element of our life. It is the second most abundant element by mass in the human body occupying an 18.5% mass ratio.[1] Carbon also serves as a common element in our daily life. The diversity of carbon includes various organic compounds and allotropes such as diamond, graphite, graphene, carbon nanotubes, and fullerenes. Among them, as the first discovered 2D material, graphene is the thinnest and strongest material and possesses excellent thermal and electrical conductivity.[2] In addition, the unique band structure endows graphene with outstanding physical properties such as ballistic transport, quantum hall effect, and high carrier mobility, which have drawn significant research interest.

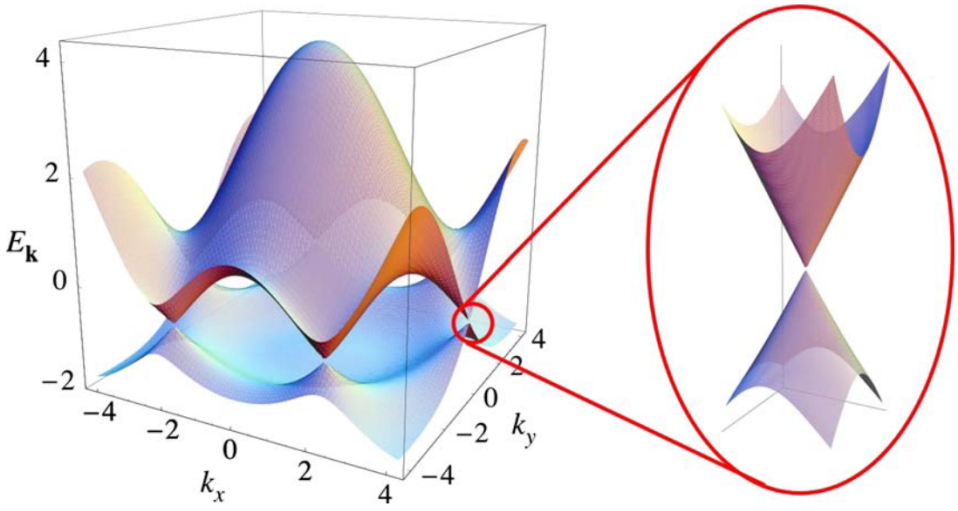

Figure 1.1. *Band structure of graphene. Adapted with permission from ref.[3] Copyright 2009, American Physical Society.*

Graphene consists of two sp^2 carbon atoms in each unit cell, resulting in two conical points K and K′ in a Brillouin region (Figure 1.1). The conduction band and the valence band of graphene are tangential at each cross point, which makes graphene a zero bandgap material.[4] This unique

electronic structure limits the applicability of graphene in semiconductors. Chemical functionalization of graphene via covalent or noncovalent approaches have been proven as a feasible strategy to open a bandgap for graphene.[5] Additionally, introducing functional groups on the surface of graphene can impart diverse properties, broadening its range of applications.[6-8]

1.2 Pyrene chemistry

1.2.1 Electron structure of pyrene

Pyrene is a simple polycyclic aromatic hydrocarbon (PAH) that was first isolated from coal tar by Laurent.[9] It is believed to form via the combustion of organic compounds. About one hundred and twenty years later, pyrene has become an abundant, inexpensive building block for dye chemistry, due to the development of industrial chemistry.

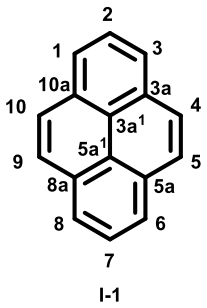

I-1

Figure 1.2. *The atom numbering of pyrene according to IUPAC.*

Pyrene consists of 14 carbons in the same plane. The planarity allows the π-electrons to be fully delocalized on both sides of the carbon backbone. According to the IUPAC recommendation in 1998, the carbon atoms in pyrene can be labeled as shown in Figure 1.2.[10] There is also a common expression for the 4, 5, and 9, 10 positions as K-region to distinguish the reactivity from other non-K-regions.

To understand the differences in reactivity at various positions, two different models of pyrene have been introduced in this chapter: Clar's rule[11] and Frontier Molecular Orbital theory.[12]

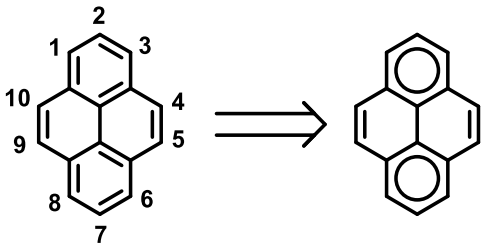

Figure 1.3. *Model of pyrene according to Clar's rule.*

Figure 1.3 describes the model of pyrene based on Clar's rule. Pyrene can be considered as two ethenyl groups attached at the 2,2' and 6,6' of a biphenyl group. Consequently, the carbon atoms in the K-region exhibit alkene-like characteristics.

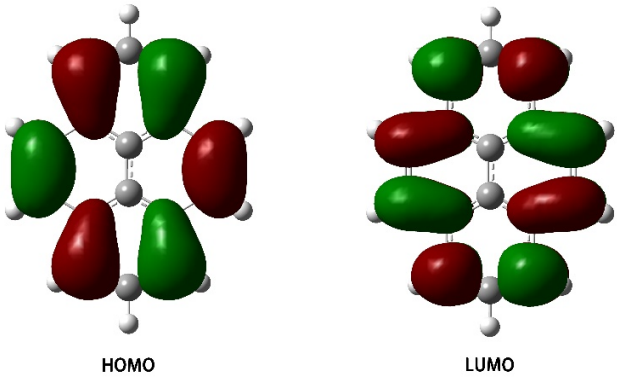

Figure 1.4. *Frontier orbitals of pyrene (HOMO left, LUMO right) calculated by DFT B3LYP (6-31GD).*

A similar conclusion can be obtained according to the Frontier Molecular Orbital Theory (Figure 1.4). Based on the result from the DFT calculation, the frontier orbitals show a significant nodal plane passing through the 2,7 positions of pyrene, indicating a low reactivity at these two positions. In contrast, the 1, 3, 6, and 8 positions as well as the 4, 5, 9, and 10 positions are regions with large orbital lobs, making functionalization at these positions much easier.

1.2.2 Functionalization at the 1,3,6,8 positions

Considering the distribution of pyrene's HOMO, the reactivity of electrophilic aromatic substitution at the 1,3,6,8 positions is the highest. Bromination is an important path to initiate the functionalization of pyrene. The C-Br bond can be easily converted into the C-N or C-O bonds via transition metal-catalyzed coupling reactions. By controlling the stoichiometric equivalent of bromine, pyrene can be converted into 1-bromo- (**I-2**), 1,6-dibromo- (**I-3**) and 1,8-dibromo- (**I-4**),

1,3,6-tribromo- (**I-5**), and 1,3,6,8-tetrabromopyrene (**I-6**), respectively.[13] As a key precursor for introducing functional groups onto pyrene, bromopyrenes have been deployed to construct different kinds of highly efficienct D-A luminescent materials via Suzuki coupling,[14] Sonogashira coupling,[15] Heck coupling,[16] as well as Buchwald-Hartwig amination.[17]

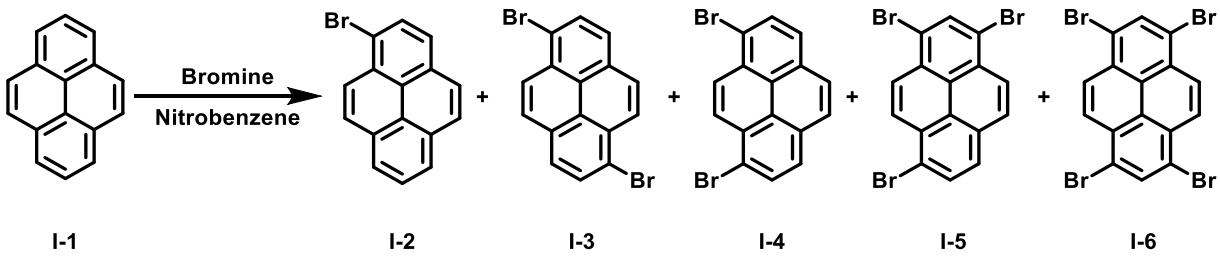

Figure 1.5. *Bromination of pyrene.*

Beyond the bromination of pyrene, functionalization at the 1-position with carbaldehyde (**I-7**) can be synthesized via the Vollmann approach[13] or in the presence of a Lewis acid, with a good yield (Figure 1.6).[18] Subsequently, 1-methylpyrene (**I-8**) can be obtained using the Wolff-Kishner-Huang reduction, with an 80% yield.

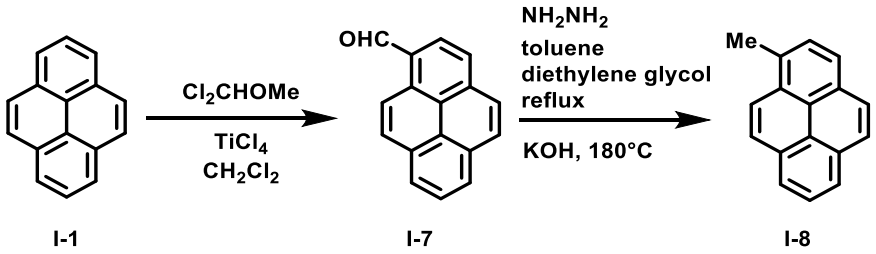

Figure 1.6. *Formylation of pyrene via Lweis acid approach and Wolff-Kishner-Huang reduction.*

It is worth mentioning that building blocks such as **I-2** are widely used when pyrene is deployed as the π-binding anchor for the functionalization of graphene/carbon nanotubes,[19-21] organometallic complexes,[22-23] and conjugated polymers.[24] In contrast, owing to the symmetry, **I-6** is frequently used as the precursor for constructing the central building blocks for metal-organic frameworks.[25-26]

1.2.3 Functionalization at the 4,5,9,10 positions

As mentioned in the previous section (Figure 1.3), Clar's sextet rule is meaningful to understand the selectivity of the functionalization of the K-region (4,5,9,10 positions of pyrene). The alkene-

like character of the K-region enables it to react with reagents such as palladium on charcoal[27] and osmium tetraoxide.[28]

The oxidization of pyrene in the K-region to afford diketones (**I-9**) and tetraketones (**I-10**) was firstly reported using OsO_4 and was later extended to RuO_4.[29] In 2005, Harris' group developed a novel oxidation method with $RuCl_3/NaIO_4$ (Figure 1.7).[30] The abundant ketone groups enable diketones and tetraketones to play an important role in energy storage and further functionalization into acenes and heteroacenes. Our work begins with 4,5,9,10-pyrene tetraone (**I-10**), which will be discussed in detail in the later chapters.

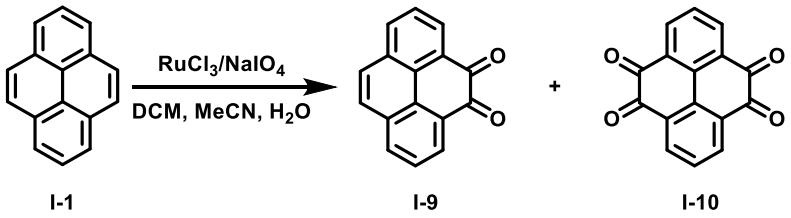

Figure 1.7. *Oxidation of pyrene to afford diketones and tetraketones.*

Interestingly, the regioselectivity of functionalization can be controlled by introducing bulky groups at the 2 and 7 positions, which effectively block the attack from the electrophiles at the 1, 3, 6, 8 positions. Yamato group selectively functionalized the 4,5,9,10 positions of pyrene with bromine and iron (III) in the presence of bulky *tert*-butyl groups at the 2,7 positions.[31] Thus, the tetrabromo product **I-12** can be converted into the 2,7-*tert*-butyl-4,5,9,10-pyrenetetraone **I-15**.

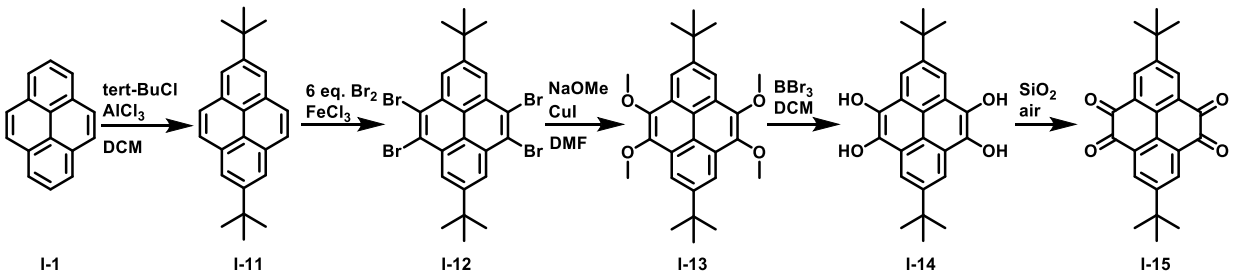

Figure 1.8. *Yamato's 2,7-bistertbutylpyrene-4,5,9,10-tetraone synthesis.*

1.2.4 Functionalization at the 2,7 positions

As mentioned in Chapter 2.1, functionalization at the 2.7 positions is challenging since the frontier orbital nodal plane passes through these positions of pyrene. Different strategies have been devised

to address the issue: a) introducing groups with high steric demand; b) the total synthesis of pyrene; c) eliminating the nodal plane of pyrene. The strategies will be discussed in the paragraphs below.

As shown in Chapter 2.3, the Friedel-Crafts alkylation using tert-butyl chloride and aluminum chloride can afford 2,7-*tert*-butyl-pyrene **I-11** in high yield and good regioselectivity as a thermodynamic product.[32] A series of isomers will be obtained in the same reaction if isopropyl chloride is used as the electrophile.

Multi-step synthesis used to be the predominant strategy to obtain the 2,7-substituted pyrene for a long time. According to Boldt and Bruhke's method (Figure 1.9), the synthesis of 2,7-substituted pyrene starts with the construction of thiocyclophane (**I-17**).[33] Via a subsequent sulfur extrusion, $3a^1$-$5a^1$ bond formation, and a final oxidation, the 2,7-dihydroxylpyrene was obtained (**I-21**). The attempt to form diketone (**I-22**) was failed.

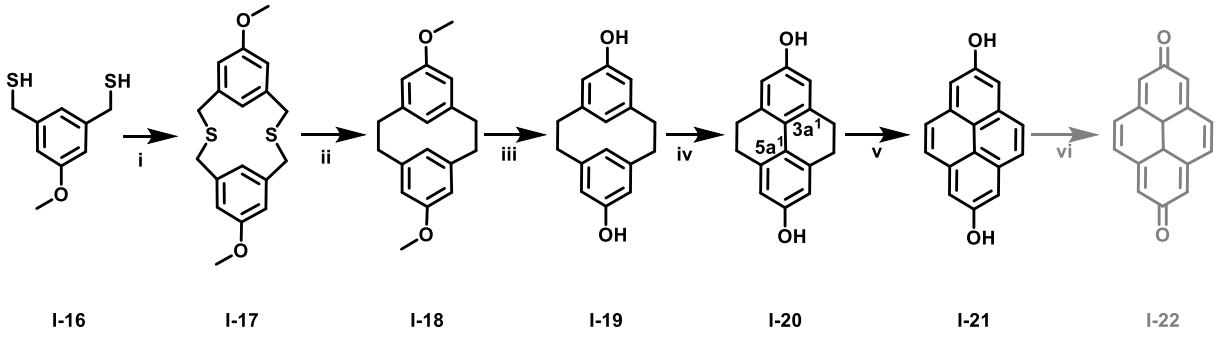

Figure 1.9. *Attempted pyrene-2,7-dione total synthesis. i: m-MeOPh(CH_2Br), KOH. ii: hν, $(CH_3O)_3P$. iii: BBr_3. iv: $AgCO_3$/celite. v: Pd/C. vi: $Pb(OAc)_4$.*

The concept of eliminating the nodal plane can be achieved by partial hydrogenation of pyrene (Figure 1.10).[34] The reduction product **I-23** behaves like a 2,2',6,6'-substituted 1,1'-biphenyl. The former 2,7 positions have a high orbital density after the hydrogenation, enabling further bromination. The rearomatization is carried out by bromine in carbon disulfide. The final 2,7-dibromo pyrene has been proven an important precursor for synthesis and polymer chemistry.

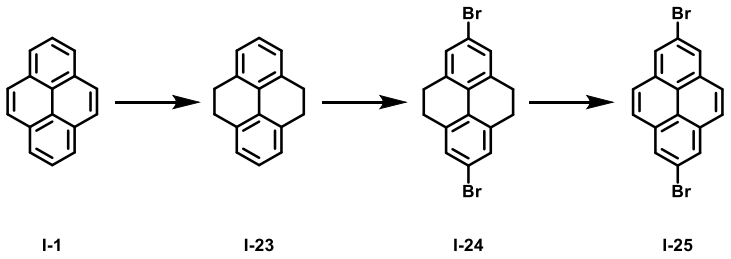

Figure 1.10. *2,7-dibromopyrene (**I-25**) synthesis. i: H_2, Pd/C. ii: $Br_2/CHCl_3$. iii: Br_2, CS_2*

Owing to the development of transition metal C-H activation, it is possible to introduce functional groups at the 2,7 positions directly with an iridium/bipyridyl catalyst system.[35] The 2,7-borylation product **I-26** enables the preparation of various small molecules and polymers via Suzuki-Miyaura coupling reactions.

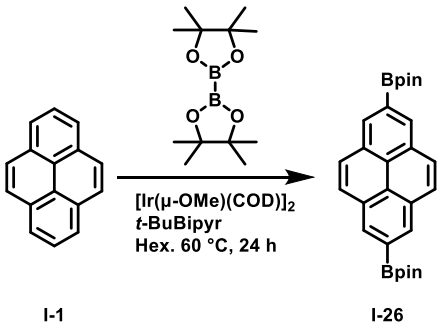

Figure 1.11. *Iridium catalyzed borylation of pyrene.*

1.2.5 π-extension of diketones and tetraketones

As an important species of pyrene derivatives, pyrene-4,5,9.10-tetraone **I-10** plays an important role in the field of energy storage[36-38] and catalysis[39] due to the abundant redox-active groups. Besides, the ketone groups endow the possibility to construct polycyclic aromatic hydrocarbon (PAH) especially acenes and hetero acenes via various paths based on ketone reactions.

The synthesis of acenes lacks the examples starting with pyrene-4,5,9,10-tetraone. However, via classic reactions such as aldol condensation and Diels-Alder reactions, acene **I-28** can be obtained with a moderate yield (Figure 1.12).[40]

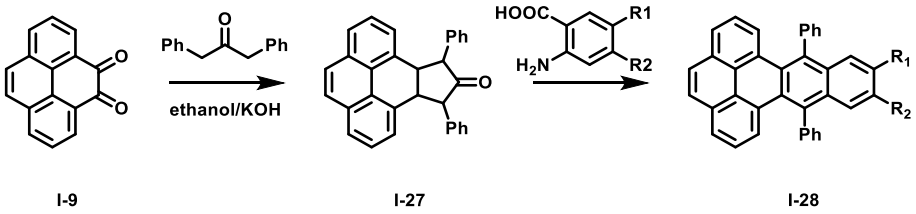

Figure 1.12. *Synthesis of acenes starting with diketone.*

Compared to the synthesis of acenes, the synthesis of pyrazaacenes from pyrene tetraone is much straight forward. Various *o*-diamines are used for condensation reactions in the ethanol/acetic acid system to obtain different substituted pyrazaacenes.[41]

1.3 Aims

The aims of this thesis in the field of redox- or photo-active functional molecules were to:

I. Design and synthesize pyrene-4,5,9,10-tetraone-based redox- or photo-active functional organic molecules.

II. Explore the structure-property relationship of graphene-based hybrid materials that are functionalized with these novel organic species for applications in energy storage and optoelectronics.

2. Characterization and analytical methods

The structures of organic molecules are identified by proton/carbon nuclear magnetic resonance, mass spectrometry, and infrared spectroscopy. The properties of functionalized graphene can be determined with X-ray photoelectron spectroscopy, UV-Vis absorption spectroscopy, and fluorescence spectroscopy. The electrochemical performance and the charge storage mechanism of electrode materials can be measured with cyclic voltammetry (CV), EIS and Galvanostatic charge-discharge (GCD) tests.

2.1 Nuclear magnetic resonance sspectroscopy

Nuclear magnetic resonance (NMR) spectroscopy is a technique to determine the structure of an organic molecule and quantify the components in a mixture. The principle of NMR spectroscopy involves the absorption of electromagnetic radiation by atomic nuclei with non-zero spin when exposed to an external magnetic field, resulting in higher energy-level transitions. Since each specific nucleus only absorbs a specific frequency, NMR can generally detect one isotope at a time. The most used NMR types are ^{1}H NMR and ^{13}C NMR. For each type of nuclei, the absorbed frequency is not always constant. The frequency is usually lowered because of the nuclear shielding generated by the surrounding electron(s). The difference in the electronic environment allows NMR to be used to identify the structure of a chemical. The difference observed in the surrounding magnetic field is defined as the chemical shift.

The compound to be measured is usually dissolved in a deuterated solvent and filled into an NMR tube. The deuterated solvent is selected to prevent interference from solvent signals since the chemical shift of deuterium nuclei is very different from that of protons in a ^{1}H NMR experiment. The Nobel Prize has been awarded five times in recognition of the development of technologies related to NMR, honoring one of the most significant discoveries in the history of science.[42]

2.2 Mass spectrometry

Mass spectrometry is a technique to measure the mass-to-charge ratio (m/z) of ions. The fundamental principle involves ionizing the components of a sample in an ion source to generate charged ions with distinct mass-to-charge ratios. It is commonly used to accurately determine the molecular weight of sample components.

2.3 X-ray photoelectron spectroscopy

X-ray photoelectron spectroscopy is a powerful tool to analyze the material surface both quantitatively and qualitatively.[43] The inner shell electrons of different elements have different binding energies. The value of the binding energy is also affected by the chemical surroundings of the elements. With the irradiation of the X-ray beam, the inner shell electrons are released with specific kinetic energies (E_k). The binding energy of the inner shell electrons (E_B) can be determined by the following equation:

$$E_B = hv - E_k \tag{2.1}$$

Here, *hv* is the energy of the photon from the X-ray source. For a given monochromatic excitation source and a specific atomic orbital, the energy of the emitted photoelectron is unique to that orbital. Additionally, the binding energy of inner-shell electrons in atoms varies depending on their chemical environment. This variation is observed in the spectrum as a shift in peak positions. Due to the limited escape depth of photoelectrons, only photoelectrons emitted from a thin layer (≤ 10 nm) near the surface of the sample are able to escape.[44]

2.4 Electrochemical methods

The electrochemical performance of electrode materials is evaluated in three-electrode and two-electrode systems with CV, GCD, and electrochemical impedance spectroscopy (EIS). Using these testing methods, parameters such as capacity, operating voltage window, equivalent series resistance, energy, and power density can be calculated. Each measurement targets specific parameters.

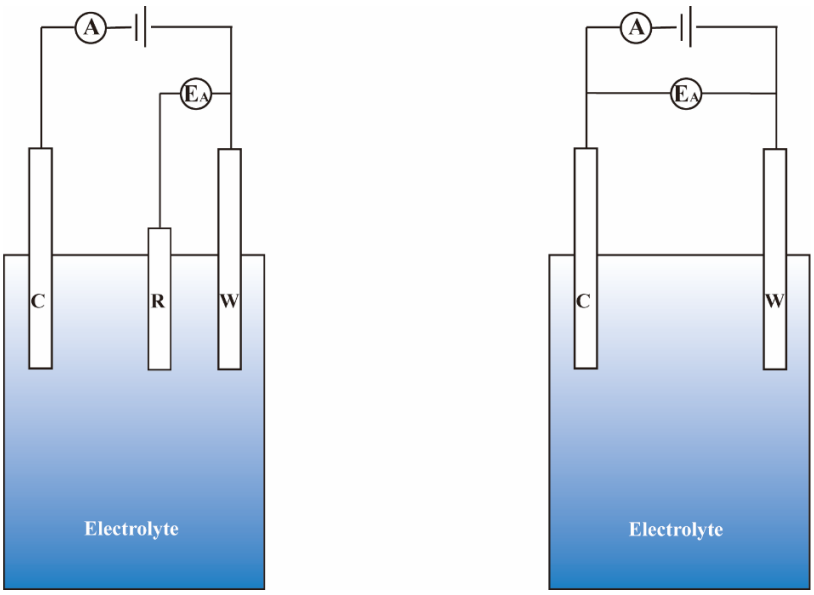

Figure 2.1. *Schematic diagram of a 3-electrode setup (left) and a 2-electrode setup (right). E_A is the potential applied between reference and working electrodes. W, C, and R are the working, counter, and reference electrodes.*

Figure 2.1 exhibits the structure of a three-electrode setup and a two-electrode setup for electrochemical tests. The three-electrode setup consists of a working electrode, a counter electrode, and a reference electrode. The working electrode is the testing electrode where the electrochemical process happens during the test. The reference electrode is an electrode with a precisely known electrode potential, which measures and controls the potential of the working electrode. To balance the current passing through the working electrode, a counter electrode is employed to facilitate the corresponding opposite electrochemical reaction. The three-electrode system focuses on investigating the electrochemical characterization of the working electrode, which is why it is also referred to as a half-cell device. In contrast, the two-electrode system only has the working electrode and the counter electrode. The voltage applied between the working electrode and the counter electrode defines the operating voltage window of the full-cell device.

2.4.1 Cyclic voltammetry

During a CV measurement, the potential applied to the device changes at a fixed rate, which is named as the scan rate. The potential applied between the cathode and anode or between the working electrode and counter electrode is named as the potential window or operating window. The current in the circuit is recorded as a response to the changing potential to analyze the electrochemical process. The acquired data are plotted as current (A) *v.s.* potential (V).[45]

2.4.2 Galvanostatic charge/discharge (GCD)

GCD is a technique used to charge and discharge a device at a constant current, also known as chronopotentiometry or constant current charge/discharge. It records the potential (V) as a function of time (s). The GCD test provides valuable information, including specific capacity (Cs), rate performance, operating voltage window, and equivalent series resistance (ESR). Therefore, it is considered one of the most straightforward and accurate methods for evaluating the electrochemical performance of supercapacitors.

The capacity is defined as the amount of charge (Q) stored per unit of applied voltage (V):

$$C_T = \frac{Q}{V} \tag{2.2}$$

The specific capacity refers to the charge stored per unit:

$$C_S = \frac{Q}{V \cdot \Pi} \tag{2.3}$$

Here, Π is the parameter that can convert an electrode material into the corresponding unit, such as mass, volume, or area.

Furthermore, the total charge can be defined as the product of current and time. In a GCD measurement, the total capacity can be determined by modifying Equation (2.4), given that the current remains constant during the test:

$$C_s = \frac{I\Delta t}{V\Pi} \tag{2.4}$$

2.4.3 Electrochemical impedance spectroscopy (EIS)

The resistance to alternating current is referred to as impedance (Z). ESI, within the same testing system, measures the impedance of the energy storage device using a low-amplitude alternating voltage. The data is typically presented in a Nyquist plot, which represents impedance over a range of frequencies.[46-48] EIS can be used to characterize both charge and mass transport, providing insights into the energy storage mechanism and electrochemical properties of the system.[49]

The Nyquist plot for a supercapacitor consists of spots on the curve corresponding to the decreasing alternating current frequency from the left to the right (Figure 2.2). The electrode resistance (R_s) can be read straightforwardly at point A, which includes the resistance of the electrode material and the contact resistance between the electrode material and the current collector.[50-51] The diameter of the semicircle between points A and B corresponds to the charge transfer resistance (R_{CT}), representing the resistance encountered by charge carriers as they move across the electrode-electrolyte interface.[52-53] Additionally, line BC can be approximated by a dashed straight line at intermediate frequencies. The slope of line BC represents the ion diffusion resistance at the electrode-electrolyte interface.[54-55]

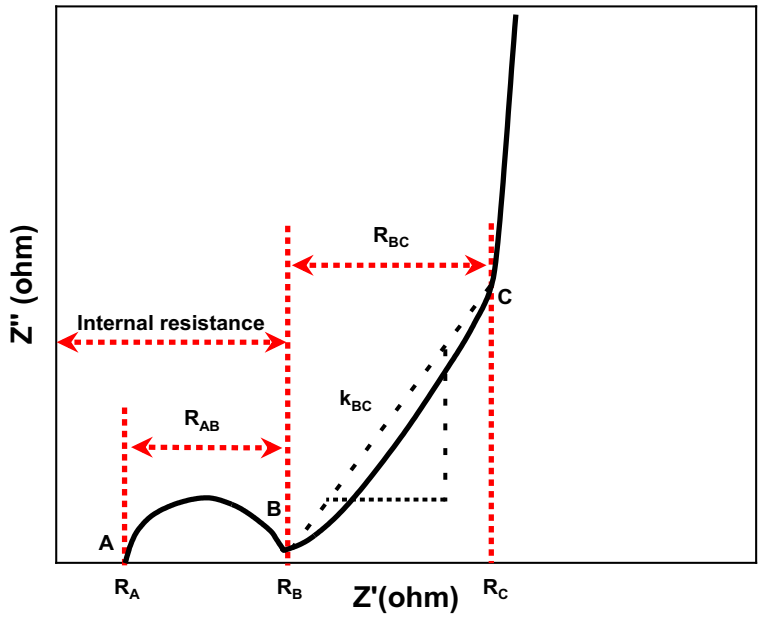

Figure 2.2. *Nyquist plot of a supercapactor.*

2.4.4 Steady-state spectroscopy

When a molecule absorbs light, it can be excited from the ground state S_0 to a higher-lying excited state S_1 and S_2 (Figure 2.3). Typically, this is followed by rapid relaxation (within 10^{-12} s) to the lowest vibrational level of S_1, a process known as internal conversion. In fluorophores, the return from S_1 to the ground state (S_0) is accompanied by photon emission, a phenomenon known as fluorescence. Additionally, molecules can transition from S_1 to an excited triplet state (T_1). The emission that occurs when the molecule returns from T_1 to S_0 is referred to as phosphorescence.

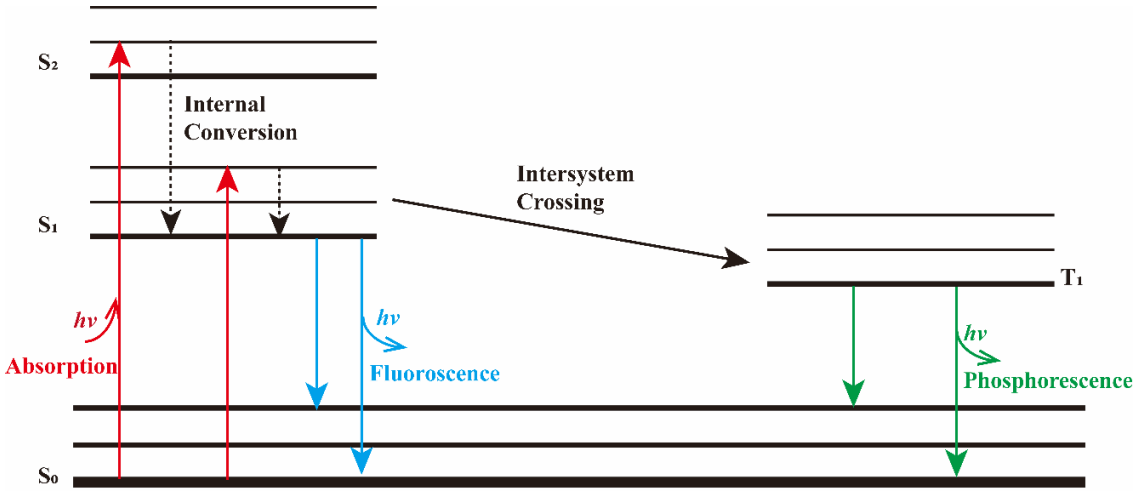

Figure 2.3. *Jablonski diagram showing the mechanism of fluorescence and phosphorescence.*

UV-Vis steady-state absorption spectroscopy is a technique that utilizes the continuous spectrum of electromagnetic radiation in the ultraviolet and visible regions to irradiate a sample, allowing for the analysis of the relative light absorption by the molecules within the substance. Additionally, based on the Lambert-Beer law, the relationship between the concentration of a solution and the absorbance can be elucidated, which allows quantitative analysis to be performed.[56]

$$log_{10}\left(\frac{I_0(\lambda)}{I(\lambda)}\right) = A(\lambda) = \varepsilon(\lambda)cl \tag{2.5}$$

The emission properties of a molecule can be analyzed using emission spectroscopy, with a proper excitation wavelength selected from its UV/Vis absorption spectrum. The fluorescence quantum yield can be determined from the absorption and emission spectra of the molecule, using an appropriate reference compound. Additionally, interactions between 2D materials and organic molecules or polymers can be evaluated by spectrophotometric titration.

3. Aqueous supercapacitors based on organic molecule-functionalized graphene

3.1 Background

During the past two hundred years, the development of human beings has been driven by energy transitions. The utilization of energy has undergone three major changes: "fire and firewood", "coal and steam engine", and "oil and internal combustion engine". With the energy transition, industry replaced agriculture as the dominant sector of the global economy. As a non-renewable energy, the supply of fossil fuels will decrease over time. Besides, the emission of carbon dioxide from the combustion of fossil fuel caused a series of environmental problems, which threatened human survival and development.[57-58] To address this issue, renewable energy sources such as solar, tidal, hydrogen, and wind are being explored as viable alternatives to fossil fuels. Electric energy plays a vital role in converting the stored energy from renewable sources, making it available for production and daily life activities. Additionally, most of the renewable energies are affected by seasons, weather, and temperature. Using electrical energy storage (EES) devices can convert renewable energy into a steady, reliable, and effective power supply.[59] Thus, the effective use of renewable energy can be achieved by developing EES devices such as metal ion batteries, and supercapacitors.[60-61]

To evaluate the electrochemical performance of EES devices, the concepts of energy density and power density are among the most commonly referenced metrics. The concept of energy density describes the quantity of energy stored per unit. On the other hand, power density refers to how fast an energy storage device can deliver energy. Figure 3.1 represents the relationship between energy density and power density, known as the Ragone plot. During the past decades, LIBs have been the major contributor to EES devices due to their high energy density, long cycle life, and stable power output. However, due to the shortage of lithium resources, risk of explosion resulting from a short circuit, and the hazardousness of the electrolyte, it is risky to use LIBs in large-scale energy storage applications. Furthermore, limited by the radius, lithium ions shows a relatively low diffusion rate inside electrode materials, limiting the power density of LIBs.[62] In contrast, electric double-layer capacitors (EDLCs) can store charges by adsorbing charge carriers at the surface of electrode materials, enabling rapid charge/discharge process. Thus, EDLCs can achieve

outstanding power density and ultra-long cycle life compared to other energy storage devices. Due to the limited specific surface area, EDLCs cannot reach a high energy density, which constrains their application scenarios. Developing safe energy storage devices with high energy and power densities is essential to meet the demands of a rapidly developing society. Compared to LIBs and EDLCs, supercapacitors exhibit considerable energy density, high power density, ultra-long cycle life, and boarder working temperature.

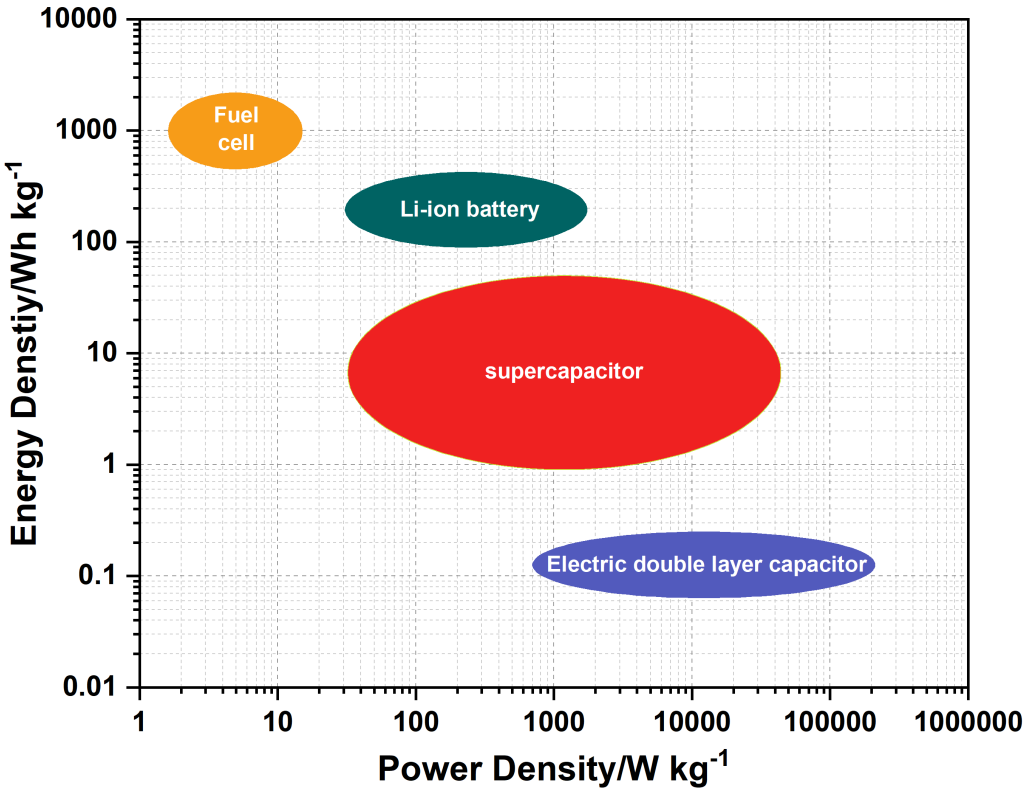

Figure 3.1. *Ragone plot of electrochemical energy storage devices.*

Electrolyte plays a major role in conveying charge carriers between the cathode and anode inside EES devices.[63] The electrolytes for supercapacitors can be classified into liquid electrolytes, solid-state, and quasi-solid-state electrolytes.[64-65] Liquid electrolytes including organic electrolytes, ion liquid electrolytes, and aqueous electrolytes are the most common electrolytes. Among these, organic electrolytes can offer a wide operating window of up to 2.5-2.8 V, enabling them to dominate the market share. However, organic electrolytes often use acetonitrile or propylene carbonate as the solvent, which is less conductive and highly flammable. Considering

the safety issue and the power density, aqueous electrolytes might be a more promising candidate for large-scale energy storage.

3.2 Aqueous electrical energy storage

To date, aqueous EES devices are developing rapidly, owing to the high ionic conductivity, enhanced safety, and easy preparation of aqueous electrolytes.[66] The most common aqueous electrolytes are H_2SO_4, KOH, NaOH, Na_2SO_4, K_2SO_4, and NaCl, etc.[67] However, limited by the thermodynamic decomposition voltage of water (1.23 V), expanding the potential operating window of aqueous supercapacitors is an important topic in device design. This part will be explained in chapter 3.2.3.

3.2.1 Introduction of aqueous supercapacitors

The history of supercapacitors can be traced back to the 1700s. Ewald Georg von Kleist and Pieter van Musschenbroek invented the first capacitor named the 'Leyden jar' (Figure 3.2). After 300 years of development, capacitors have evolved into various energy storage mechanisms. The Leyden jar consists of two pieces of metal foil, water in a glass jar, and a metal chain. Based on this fundamental structure of capacitors, static electricity can be stored at the interface between the electrode material and the electrolyte. In 1853, von Helmholtz first developed the electric double-layer model during the study of a colloidal suspension, marking the beginning of supercapacitor research.[68] Then the model of EDLCs was further developed by Gouy,[69] Stern,[70] and Grahame,[71] which constitutes the modern theory of EDLCs. In 1954, Howard Becker, an engineer from General Electric, submitted the first patent for electrochemical capacitors.[72] Later, Robert Rightmire from Standard Oil of Ohio, Inc. (SOHIO) developed a capacitor with a non-aqueous electrolyte.[73] With authorization from SOHIO, NEC Inc. commercialized electrochemical capacitors in 1971, using them as the backup power supplier for computer memories with a new name called 'supercapacitors'. To date, supercapacitors with various novel electrode materials have been developed and commercialized, making great contributions to the development of human society, especially the electronics industry.

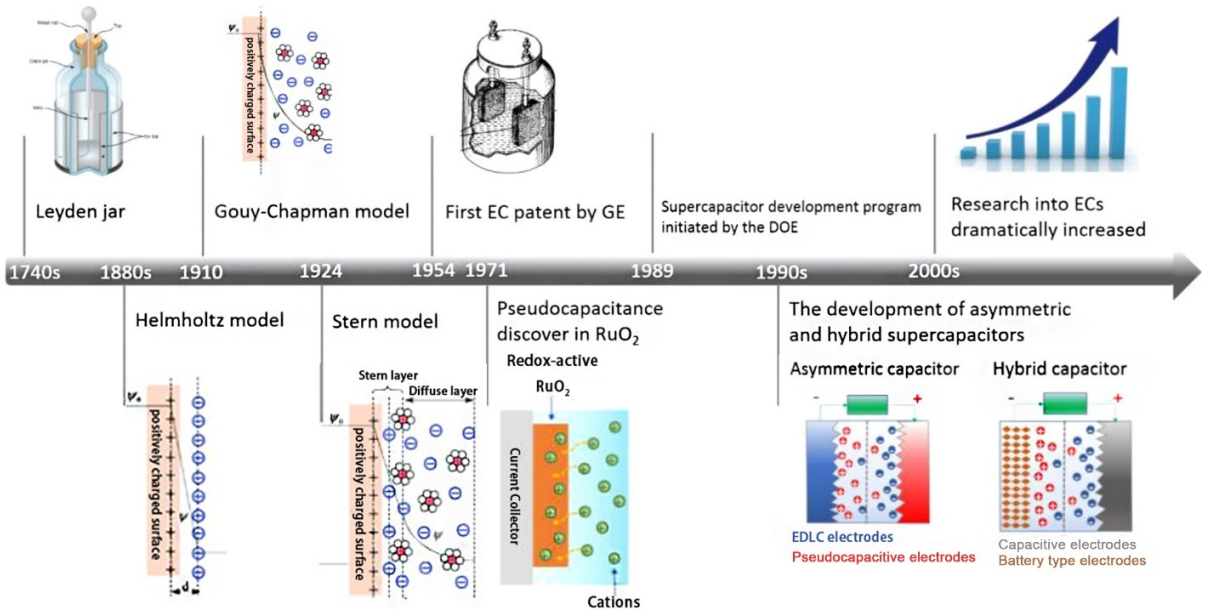

Figure 3.2. *Timeline for the development of supercapacitors. Adapted with permission from ref.* [57] *Copyright 2018, American Chemical Society.*

3.2.2 Charge storage mechanism of supercapacitors and testing methods

According to the charge storage mechanisms, electrode materials can be classified into three categories: EDLCs, pseudocapacitive, and Faradaic materials (Figure 3.3).[74]

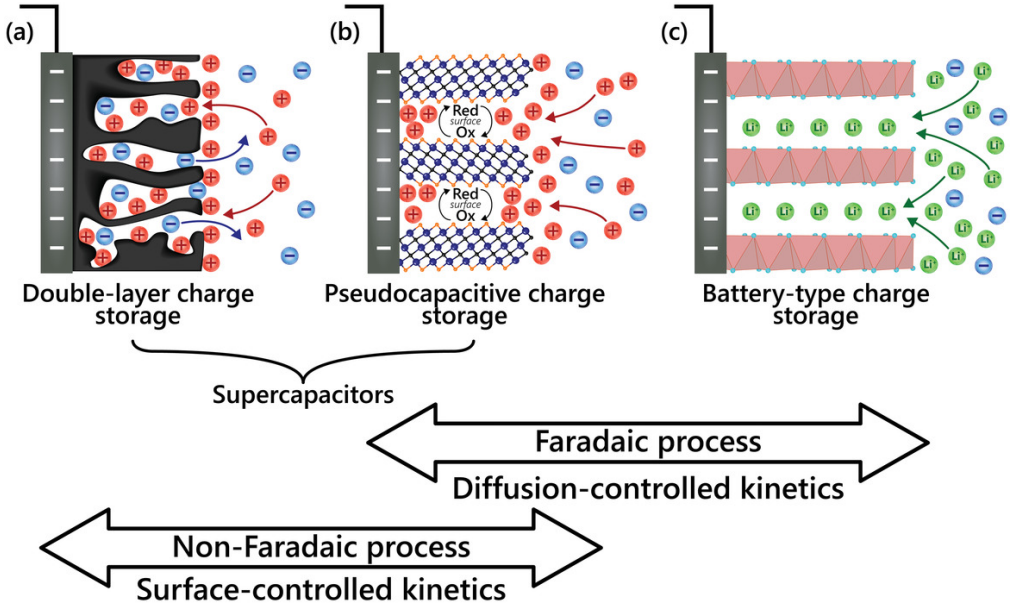

Figure 3.3. *Charge storage mechanism of electrode materials: (a) EDLCs, (b) pseudocapacitive, (c) Faradaic mechanism. Adapted with permission from ref.* [49] *Copyright 2019, John Wiley and Son.*

a) EDLCs

EDLCs are the most studied and simplest capacitors that hold the highest market share. During the charging process, the cations/anions will move to the surface of the cathode/anode. The charge stored can be calculated according to the following formula:

$$C = \frac{\varepsilon s}{4\pi k d} \tag{3.1}$$

Here, s is the contact surface area between the electrode and the electrolyte, ε is the dielectric constant of the electrolyte, and d is the distance between the parallel electrodes. The charge accumulated at the surface of the EDLC material will go back to the electrolyte during the discharge process. The charge-discharge process is purely physical, as it does not involve electron transfer between the electrode and the electrolyte. This is the reason that EDLC type materials possess high power density, long cycle life, and rapid charge-discharge rate. Carbon-based materials such as activated charcoal, carbon nanotube, and graphene are usually considered EDLC type materials. Since the charge adsorption only happens at the interface between the electrode and electrolyte, the specific capacity of EDLC type materials highly relies on their surface area. In aqueous electrolytes, the energy density of EDLCs is usually below 10 Wh kg^{-1}.

b) Pseudocapacitive mechanism

The energy storage of a pseudocapacitor is achieved by reversible redox reactions that happen at the surface or near-surface area of electrode materials.[75] Consequently, the response time of pseudocapacitors (approximately 10^{-2}-10^{-4} s) is significantly longer compared to that of EDLCs (approximately 10^{-8} s).[76]

c) Faradaic mechanism (battery type)

Differs from the EDLC and pseudocapacitive materials, battery-type materials such as transition metal oxides, sulfides, and phosphides depend on the reversible Faradaic redox reactions in the bulk phase of the materials. Thus, they can reach a relatively higher theoretical specific capacity. However, since the charge-discharge process will change the crystal structure of the electrode material, battery-type electrode materials have poor electrochemical reversibility.

Comprehensively using CV, GCD and quantitative kinetic analysis of electrode materials can be a powerful tool to precisely distinguish the charge storage mechanism of electrode materials.[77-79]

As shown in Figure 3.4, the CV curve of EDLC materials displays a constant current with an approximately rectangular shape, indicating capacitance characteristics. Similarly, the potential in the GCD curve changes linearly with time, reflecting typical capacitive behavior (Figure 3.4 a, c). For pseudocapacitive materials, the CV curve typically shows a near-rectangular shape, while the GCD curve is nearly linear profile. Unlike EDLC materials, pseudocapacitive materials display inflection points rather than significant plateaus (Figure 3.4 b, d-f). In contrast, the CV curves of battery-type materials shows significant redox peaks, while charge-discharge plateaus can be found in the GCD curves (Figure 3.4 g-i).

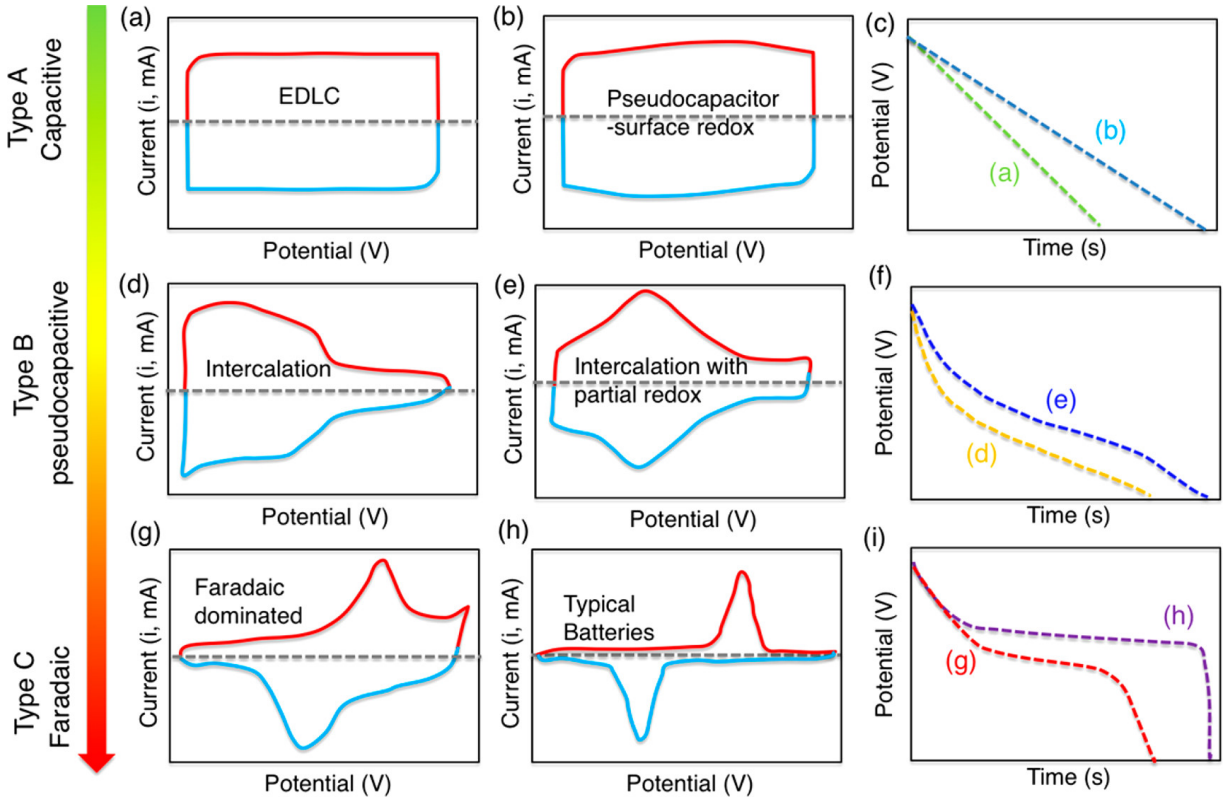

Figure 3.4. *CV curves and corresponding GCD curves of (a-c) EDLC and surface pseudocapacitor-type materials, (d-f) intercalation pseudocapacitor materials, and (g-i) battery-type materials. Adapted with permission from ref.* [79] *Copyright 2018, American Chemical Society.*

Additionally, based on the CV result, the contribution of charge storage (diffusion or surface control kinetics) can be determined by the relationship between the current (i_p) and the corresponding scan rate (v) according to the following equation:[80]

$$i_p = av^b \tag{3.2}$$

Here, the b value can be determined by calculating the slop of the curve plotted as a function of $\log(i_p)$ and $\log(v)$.

$$logi_p = blogv + loga \tag{3.3}$$

If b = 1, the current i_p changes linearly with the scan rate, which means the electrochemical process is surface-controlled, suggesting a capacitive behaviour; if the b = 0.5, the redox reaction is controlled by semi-infinite linear diffusion, suggesting a battery behavior.[81] The contribution of surface- and diffusion-controlled reactions can be further quantified according to the equation:[82]

$$i_{(v)} = k_1 v + k_2 v^{1/2} \tag{3.4}$$

Where $i_{(v)}$ is the total current density at a specific voltage, k_1v and $k_2v^{1/2}$ are the current contributed by capacitance control and the current controlled by diffusion, respectively. and the values of k_1 and k_2 can be obtained from the slope of the $(i_{(v)}/v^{1/2})$ and $v^{1/2}$ curves.

3.2.3 Aqueous asymmetric supercapacitors

The definition of "asymmetric" and "hybrid" should be introduced when two pieces of electrodes are assembled. A "hybrid capacitor" refers to a device with two electrodes that have different charge storage mechanisms. The concept of an asymmetric supercapacitor (ASC) covers a wider range. It refers to any capacitor consisting of two different electrodes. No doubt that hybrid devices are a special category of ASCs.[57]

As mentioned in Chapter 1, energy density is a vital parameter for energy storage devices. For supercapacitors, the energy density (E) is determined by the specific capacity and the voltage operating window of the full cell, according to the following equation:[83]

$$E = \frac{1}{2} CV^2 \tag{3.5}$$

The power density (P) of a device can be further calculated by:

$$P = E \times \frac{3600}{\Delta t} \tag{3.6}$$

The energy density of the device is positively correlated with the square of the voltage operating window of the full-cell device. Thus, broadening the voltage window of the full cell is one of the straightforward ways to improve the energy density of the device. However, limited by the thermodynamic breakdown voltage of water, the potential window of a single electrode is limited to 1.23 V. Using two pieces of electrodes with different potential windows can expand the voltage window of the full-cell devices beyond 1.23 V. Thus, developing new electrode materials to widen the operating window presents a promising strategy for achieving higher energy in aqueous supercapacitors.

3.2.4 Electrode materials in supercapacitors

Currently, the developed electrode materials include transition metal oxides, oxides/hydroxides, sulfides, selenides, phosphides, carbon-based materials (activated charcoal, carbon nanotube, and graphene), and redox-active organic systems (small molecules and conductive polymers).[84-85] Among these, organic compounds offer advantages such as low cost and design flexibility, rendering them promising candidates for electrode materials. Besides, organic compounds have abundant proton storage sites, which is suitable in acidic electrolytes.[86] According to the charge storage mechanism, organic electrode materials can be classified into n-type, p-type, and bipolar-type (Figure 3.5).[87] During the electrochemical reactions, n-type materials such as ketones, pyrazines, accept electrons resulting in a negatively charged species. In contrast, p-type materials usually donate electrons and become positively charged. Bipolar-type materials can donate and accept electrons and can be both oxidized and reduced. Currently, redox-active organic molecules with carbonyl groups, such as quinones, ketones, and carboxylates (n-type), exhibit numerous oxidation/reduction active sites and rapid reaction kinetics, making them highly attractive for aqueous energy storage devices.[88]

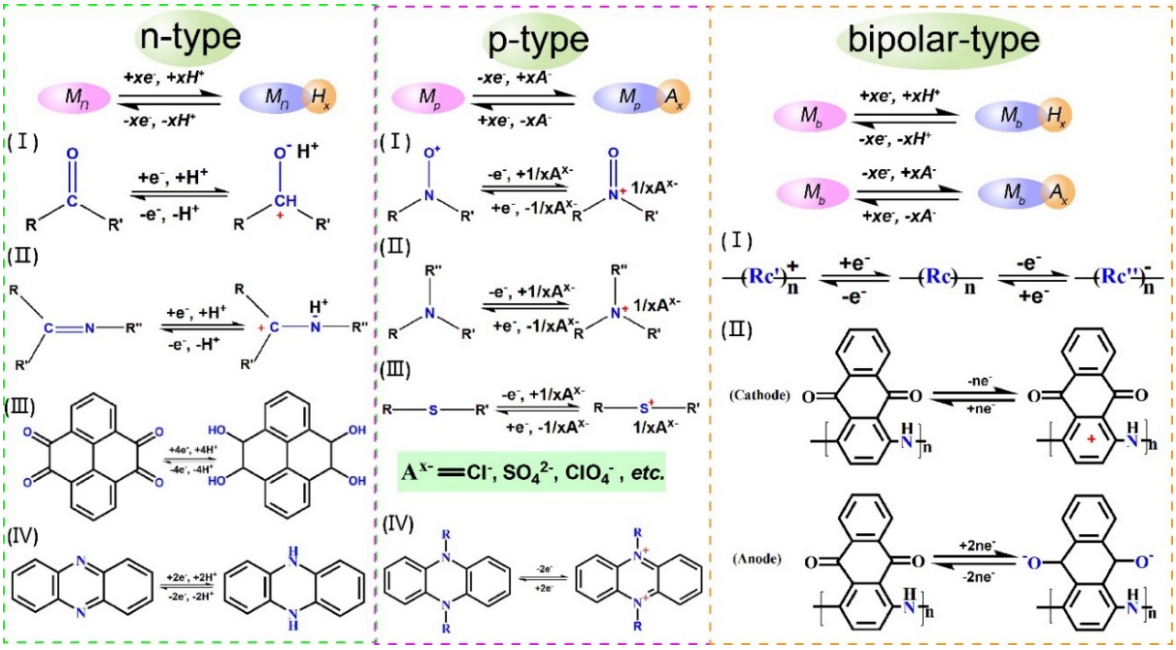

Figure 3.5. *Energy storage mechanism of organic electrode materials. Adapted with permission from ref.[87] Copyright 2019, John Wiley and Son.*

Organic compounds usually possess intrinsic low conductivity and inevitably dissolve into the electrolyte. Attaching organic materials to the surface of carbon-based materials has been proven an effective strategy to solve these issues.[89] Graphene has an infinite sp^2 carbon structure, which endows it with high electrical conductivity. Meanwhile, graphene has a large specific surface area and shows modest capacity performance. It is a commonly used conductive substrate for organic functional molecules in energy and electronics applications.[90] In contrast to covalent functionalization of graphene, noncovalent approaches via van der Waals, hydrophobic, electrostatic interactions, or π-π stacking can retain the sp^2 carbon network, which guarantees a high electrical conductivity of the hybrid electrode materials.[91] Gogotsi and co-workers[92] used a composite material of phenothiazine molecules and rGO (phen@rGO) as the positive electrode, $Ti_3C_2T_x$ MXene as the negative electrode, and 3 M H_2SO_4 (aq.) as the electrolyte to assemble a fully pseudocapacitive ASC. The composite electrode exhibits a specific capacity of 300 F g^{-1} at a scan rate of 5 mV s^{-1}. The full-cell device retains 80% capacity after 30000 charge-discharge cycles, demonstrating excellent cycle performance.

3.3 Aim

The aims of this thesis in the field of ASCs were to:

a) Design and synthesize pyrene-4,5,9,10-tetraone-based (PYT-based) derivatives as the redox-active molecule for graphene-based hybrid cathodes in aqueous ASCs.
b) Investigate the structure-property relationship of the designed materials as the cathode materials for supercapacitors.
c) Study and understand the charge storage mechanism of organic materials, and further explore more novel organic materials with high capacity.

3.4 Result and discussion

3.4.1 Oxidation of pyrene

As mentioned in Chapter 1, the 4,5,9,10 positions of pyrene possess double bond characters according to Clar's rule. Thus, each double bond can be oxidized into diketone by a catalytic amount of RuO_4, which is in-situ generated in the reaction.

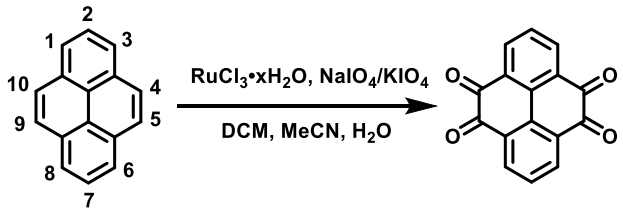

Figure 3.6. *The oxidation of pyrene.*

The optimized reaction conditions are shown in the following table:

Table 3.1. *Optimized reaction conditions for the oxidation of pyrene.*

Entry	Oxidant	T/°C	Time/h	Yield
1	$NaIO_4$	25/35	16/3	----------
2	$NaIO_4$	25/35	24/3	11%
3	$NaIO_4$	25/35/40	8/2/1	13%
4	KIO_4	25/30/35/40/50	5.5/1/2/3/4	9%
5	KIO_4	50	8h	21.3%

6	$NaIO_4$	0/35/40	6/2/1	----------
7	$KIO_4/NaIO_4$	50	8h/3h	**30%**
8	KIO_4	70	5h	15%

The oxidation mechanism is illustrated in Figure 3.7.[93] In the first step, a ruthenium (III) salt is converted into ruthenium tetraoxide (RuO_4), which subsequently turns into a Ru(VI) salt. This intermediate brings out a *syn* dihydroxylation reaction to produce the dihydroxylated product. The Ru(VI) species is then regenerated to Ru(VIII) through simple oxidation by a periodate salt, enabling the reaction to proceed with only a catalytic amount of ruthenium salt. Subsequently, the diol product reacts with the periodate salt to form a periodate ester. This ester can undergo two distinct pathways. In one pathway, cleavage of the C-C sigma bond occurs, resulting in the formation of a dialdehyde as a byproduct. In the other pathway, the reaction proceeds to form a diketone as the final product.

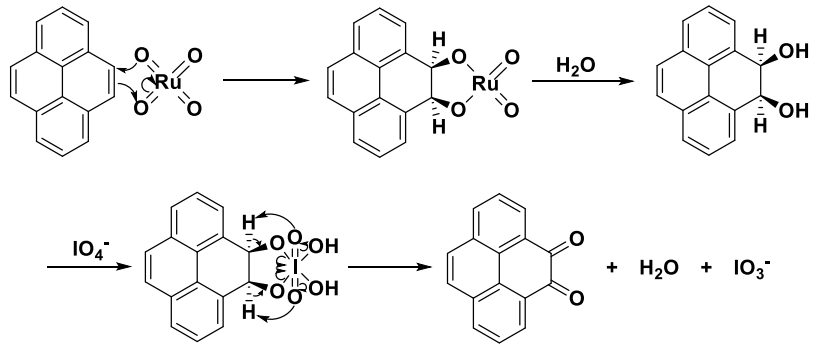

Figure 3.7. *Possible oxidation mechanism of pyrene towards pyrene dione (and tetraone)*

The latter pathway can be favored by using potassium periodate as the other oxidant, which has significantly lower solubility compared to the corresponding sodium salt.

3.4.2 Characterization of pyrene-4,5,9,10-tetraone and the corresponding nanocomposites

In this study, various types of commercially available rGO were selected as the conductive matrix for electrode materials. Compared to the rGO from LayerOne (LO), the rGO from Graphenea (GN) exhibited a higher oxygen content, as shown in Table. 3.2.

To study the interaction between the organic species and rGO, the individual component and nanocomposites are investigated by Fourier-transform infrared spectroscopy (Figure 3.8). Commercial graphene (GN and LO) exhibits no distinct absorption peaks, indicating the removal of most oxygen-containing groups from the graphene surface. The peaks of the PYT molecule at 1674cm^{-1} and 1273 cm^{-1} can be assigned to the C=O stretching and C-H bending absorption. Compared to pristine PYT, both of the strong absorption bands shifted to lower wavenumbers after combining with rGO, indicating the possible interaction between PYT and rGO.[94] In addition, the absorption peak of PYT/LO 4-5 is weaker compared to that of PYT/GN 4-5. Notably, no absorption peak is observed for the PYT/LO 2-7 composite, likely due to the confinement effect of the PYT molecules within the LO matrix.

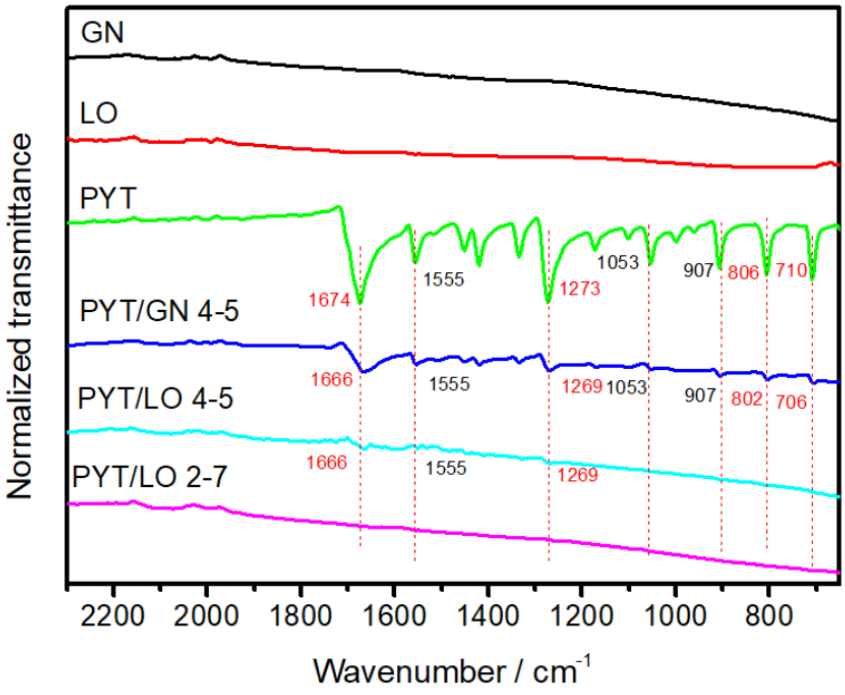

Figure 3.8. *FT-IR spectra of PYT, GN, LO, and the corresponding nanocomposites.*[95]

Using X-ray photoelectron spectroscopy, the elemental content of the nanocomposites are investigated. Figure 3.9 shows the survey scan of the pristine PYT, rGO, and the corresponding nanocomposites. The survey scan spectra of all samples display a prominent C1s peak and a distinct O1s peak. From Table 3.2, the PYT molecule contains 18.1% oxygen, attributed to its four carbonyl groups. Upon incorporation with graphene, the oxygen content in the PYT/graphene (PYT/GN) 4-5 sample reaches 15.2%. The PYT/LO 4-5 (6.4%) and PYT/LO 2-7 (5.5%) composites exhibite increased oxygen content compared to LO (3.2 %), attributed to the incorporation of carbonyl groups.

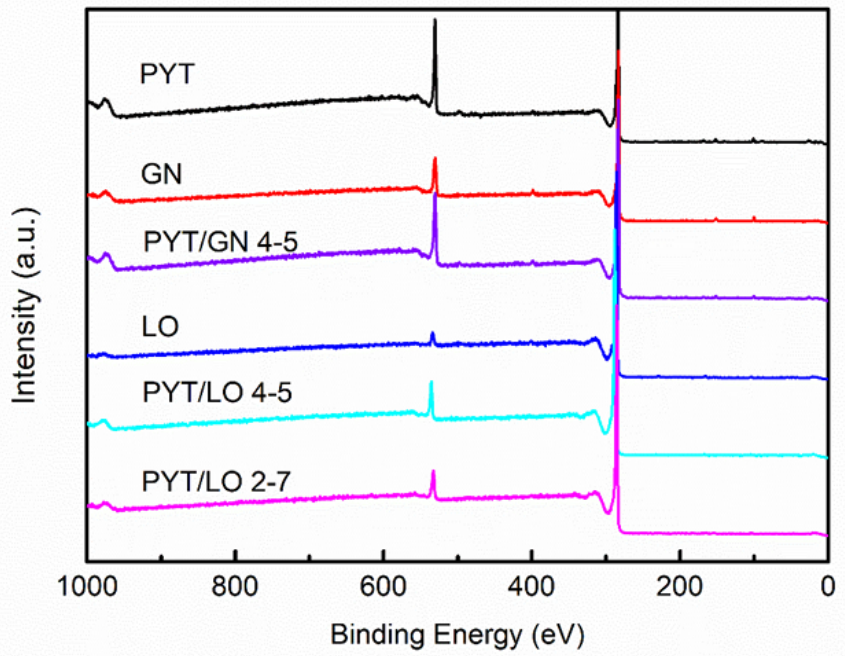

Figure 3.9. *Survey scan curves of PYT, GN, LO graphene, and the corresponding nanocomposites.*[95]

Table 3.2. *Elemental contents of PYT and the as-obtained nanocomposites.*

Sample	C (%)	O (%)
PYT	81.9	18.1
GN	88.2	11.8
PYT/GN 4-5	84.8	15.2
LO	96.8	3.2
PYT/LO 4-5	93.6	6.4
PYT/LO 2-7	94.5	5.5

3.4.3 Electrochemical performance of the pyrene-4,5,9,10-tetraone/graphene cathode

The electrochemical test of the PYT/rGO composite electrode was performed in a 1 M H_2SO_4 (aq.) electrolyte with Ag/AgCl as the reference electrode. The ratio between PYT and rGO is denoted as PYT-rGO. For example, a ratio of 8:1 between PYT and graphene (GN) is represented as PYT-GN 8-1. Figure 3.10 (a) shows the comparison of all CV curves at 10 mV s^{-1}. GN presents a typical nearly rectangular shape, indicating that the EDLC behavior dominates the charge storage process. After adding the PYT molecules, all the CV curves of the PYT/GN electrodes show two pairs of obvious reversible redox peaks at ~0.23/0.17 and ~0.37/0.30 V (vs. Ag/AgCl), which can be attributed to the redox reaction of PYT.[96] Due to the limited conductivity of PYT, the CV curve of PYT/GN 8-1 circles a tiny area suggesting a relatively low specific capacity. When the ratio is adjusted to 4:5, the CV of the PYT/GN 4-5 electrode circles the biggest area, indicating the highest capacity. The same trend can be observed in the GCD curves (Figure 3.10 b). All the GCD curves of the PYT/GN composite electrodes show a symmetric bent triangle shape, indicating the pseudocapacitive mechanism. The PYT/GN 4-5 electrode exhibits the longest discharge time and the highest specific capacity among all the electrodes. This outstanding electrochemical performance is attributed to its well-designed composite structure, which effectively leverages the individual advantages and synergistic interactions between the PYT molecules and graphene nanosheets.

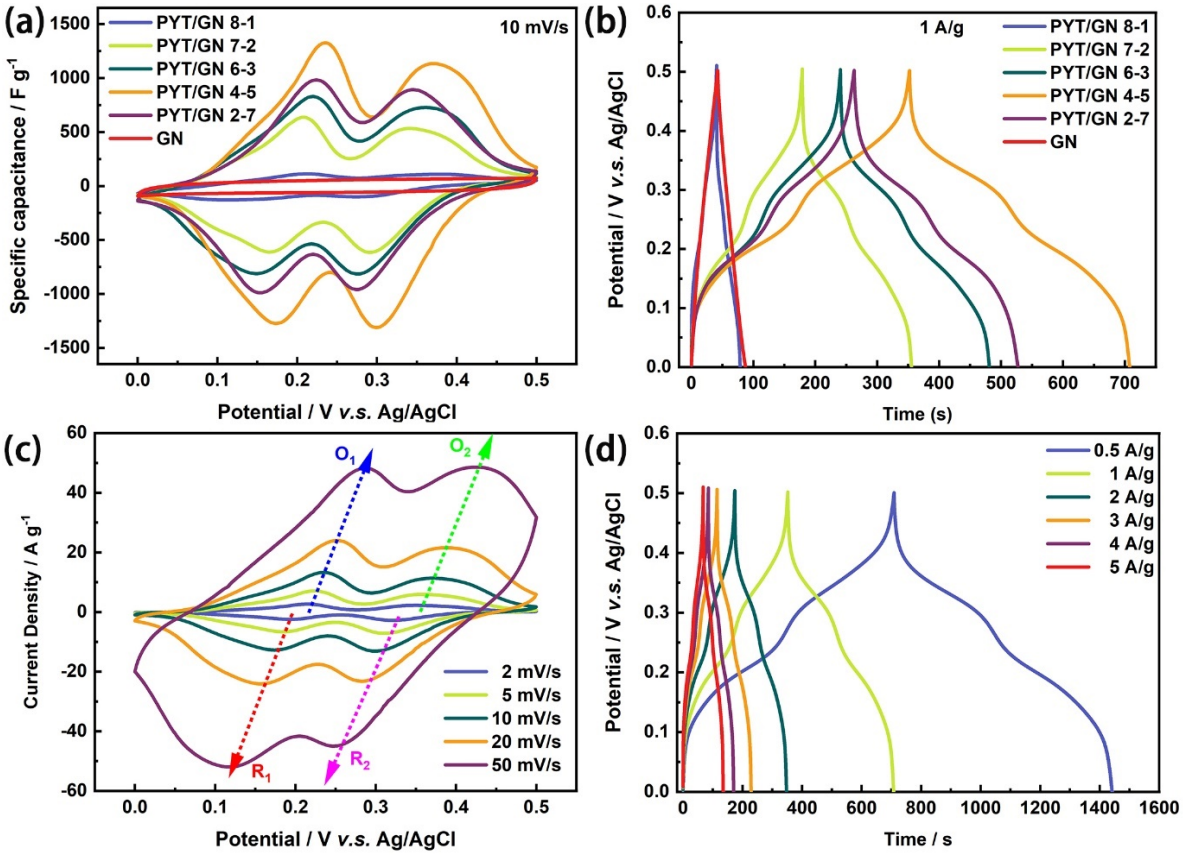

Figure 3.10. *Electrochemical characterization of PYT with GN in a three-electrode system. (a) CV curves of the PYT/GN nanocomposites with different ratios at a scan rate of 10 mV s^{-1}. (b) GCD curves of the PYT/GN nanocomposites with different ratios at a current density of 1 A g^{-1}. (c) CV curves of the PYT/GN 4-5 nanocomposite at different scan rates. (d) GCD curves of the PYT/GN 4-5 nanocomposite at different current densities.*

Figure 3.10 c and Figure 3.10 d exhibit the electrochemical performance of the PYT/GN 4-5 electrode at different scan rates and current densities. With the increase of the scan rates, the oxidation and reduction peak positions shifted towards more positive and negative potentials, respectively, due to internal resistance.[97] Notably, at a scan rate of 50 mV s^{-1}, the CV curve of the PYT/GN 4-5 electrode maintained its shape, indicating the high redox activity and excellent electrochemical reversibility of the PYT molecules within the composite electrode. At current densities ranging from 0.5 to 5 A g^{-1}, the specific capacities of the PYT/GN 4-5 electrode are 733, 711, 695, 686, 679, and 673 F g^{-1}, respectively, surpassing those of other electrode materials.[98-102] Furthermore, even at a high current density of 5 A g^{-1}, the electrode maintains specific capacity retention of 91.5%, demonstrating its excellent rate performance.

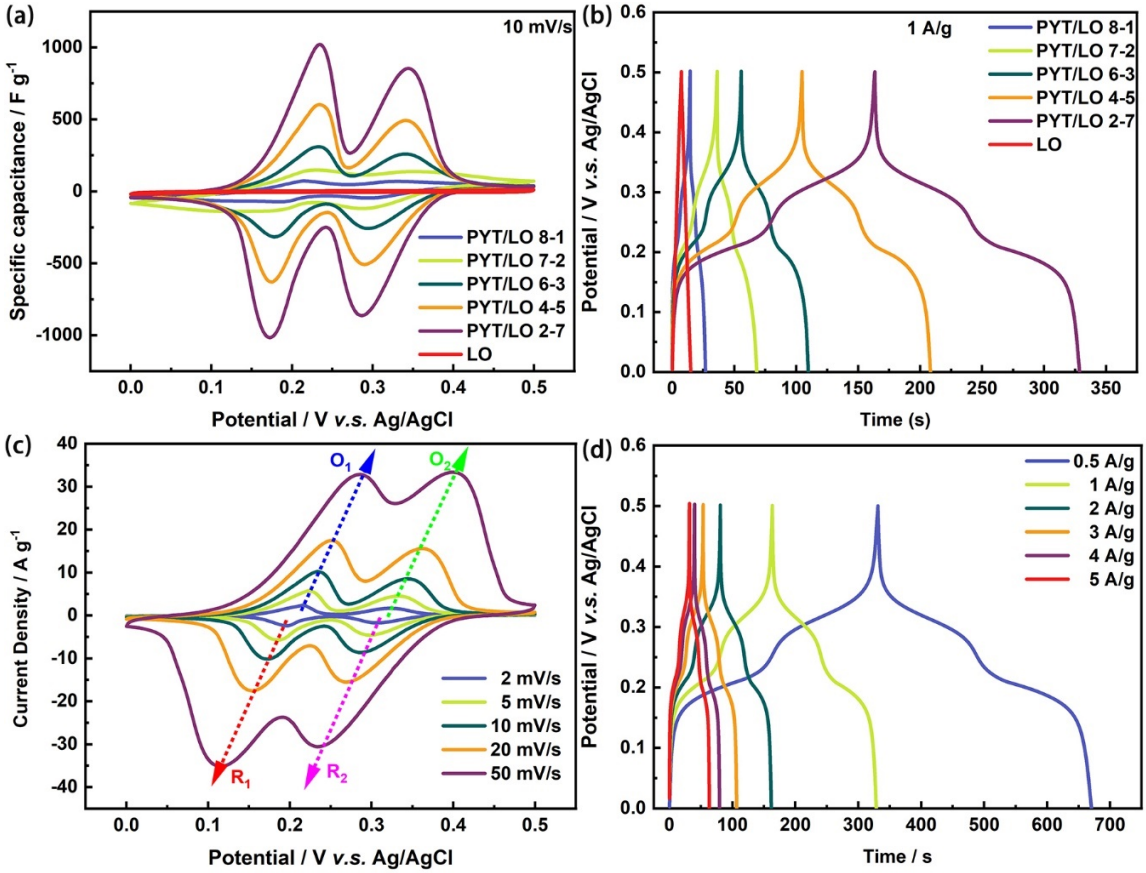

Figure 3.11. *Electrochemical characterization of PYT with LO in a three-electrode system. (a) CV curves of the PYT/LO nanocomposites with different ratios at a scan rate of 10 mV s^{-1}. (b) GCD curves of the PYT/LO nanocomposites at different ratios at 1 A g^{-1}. (c) CV curves of the PYT/LO 2-7 nanocomposite at different scan rates. (d) GCD curves of the PYT/LO 2-7 nanocomposite at different current densities.*

When the rGO with a higher reduction degree (LO) is used as the conductive substrate, the electrochemical performance of the composite electrodes was evaluated using the same tests (Figure 3.11). The integrated area of the CV curves and the discharge time of the GCD curves both indicate the specific capacity of the electrode material (Figure 3.11a and b). The pure LO shows a relatively low capacity, indicating its contribution to the composite electrode materials is neglectable. As the mass ratio of PYT to LO decreases from 8:1 to 2:7, both the CV area and discharge time of the composite electrode materials increase monotonically. This suggests an improvement in the redox activity of the composite materials, leading to an improved energy storage capacity. Figure 3.11 c and d present the CV curves of the optimized electrode material (PYT/LO 2-7) at various scan rates (2–50 mV s^{-1}) and the GCD curves at different current densities

(0.5–5 A g^{-1}), respectively. Similar to the PYT/GN 4-5, the PYT/LO 2-7 composite electrode can retain good shapes at various scan rates, indicating good reversibility and chemical stability. The specific capacities of the PYT/LO 2-7 electrode at current densities ranging from 0.5 to 5 A g^{-1} are 339, 331, 324, 320, 318, and 316 F g^{-1}, respectively.

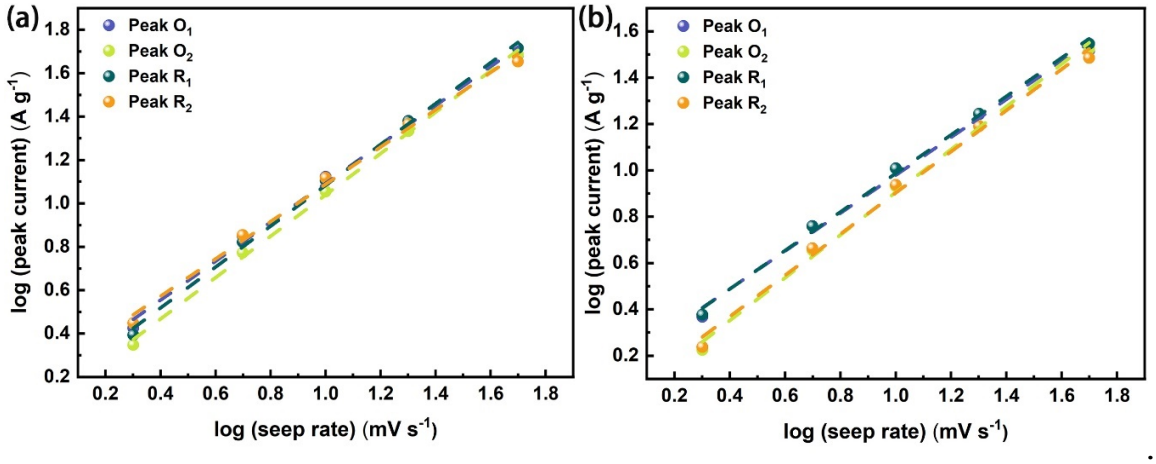

Figure 3.12. *(a) log(i) vs log(v) plots based on the CV curves of the PYT/GN 4-5 nanocomposite. (b) log(i) vs log(v) plots based on the CV curves of the PYT/LO 2-7 nanocomposite.*

The energy storage mechanism of the PYT/GN and PYT/LO composites are further evaluated according to equation 3.2. The b values of the PYT/GN 4-5 electrode are 0.90, 0.95, 0.95, and 0.86, respectively, which are close to 1 (Figure 3.12a). This indicates that surface-controlled pseudocapacitive behavior predominantly governs the charge storage process in the PYT/GN 4-5 electrode. Additionally, as shown in Figure 3.12 b, the b-values of the redox peaks in the CV curves for the PYT/LO 2-7 electrode material are 0.82, 0.92, 0.82, and 0.89, all of which are close to 1.

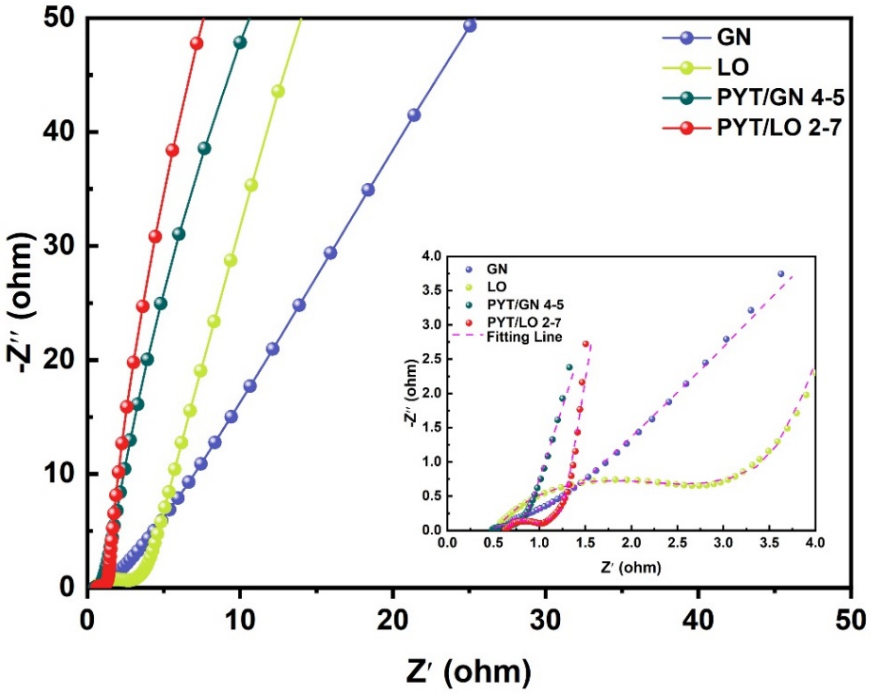

Figure 3.13. *Nyquist plots of EIS for the GN, LO, PYT/GN 4-5 and PYT/LO 2-7.*

Table 3.3 *Impedance parameters simulated from the equivalent circuits.*

Sample	Rs	R_{CT}
GN	0.51	0.96
LO	0.53	1.99
PYT/GN 4-5	0.49	0.15
PYT/LO 2-7	0.66	0.28

To further elucidate the energy storage mechanism, the EIS of GN, LO, PYT/GN 4-5, PYT/GN 2-7, PYT/LO 4-5, and PYT/LO 2-7 are presented in Nyquist plots in Figures 3.13. In the low-frequency region, all electrodes display nearly vertical lines, indicating low ion (H^+) diffusion impedance and excellent capacitive behavior. Additionally, the intercept on the X-axis in the high-frequency region represents the ohmic resistance (R_s), which encompasses the contact resistance between the active material and the current collector, the intrinsic resistance of the active material, and the ionic resistance of the electrolyte. [97] As shown in the fitting results (Figure 3.13), due to the poor conductivity of the PYT molecules, the Rs values of the PYT-based composite materials are larger than those of pure graphene (LO and GN). In addition, the diameter of the semicircle in

the mid-frequency region corresponds to the charge transfer resistance (R_{CT}), which reflects the charge transfer kinetics at the interface between the electrolyte and the electrode. Compared to pure GN (0.96 Ω) and pure LO (1.99 Ω) electrodes, the composite electrode materials exhibit a lower charge transfer resistance (R_{CT}), indicating a faster ion transfer process. This improvement may be attributed to the enhanced wettability at the interface between the electrolyte and the electrode. The EIS results demonstrate that the PYT-functionalized graphene electrode materials (PYT/GN and PYT/LO composites) exhibit excellent electron and ion transfer kinetics, which significantly enhances the electrochemical performance of the composite electrodes.

3.4.4 Characterization of A-$Ti_3C_2T_x$ as the anode material

To obtain the anode material with a lower operating potential window, $Ti_3C_2T_x$ was calcinated under an inert gas atmosphere. After calcination, the A-$Ti_3C_2T_x$ retained the layer-like structure (Figure 3.14), facilitating efficient charge transfer kinetics.

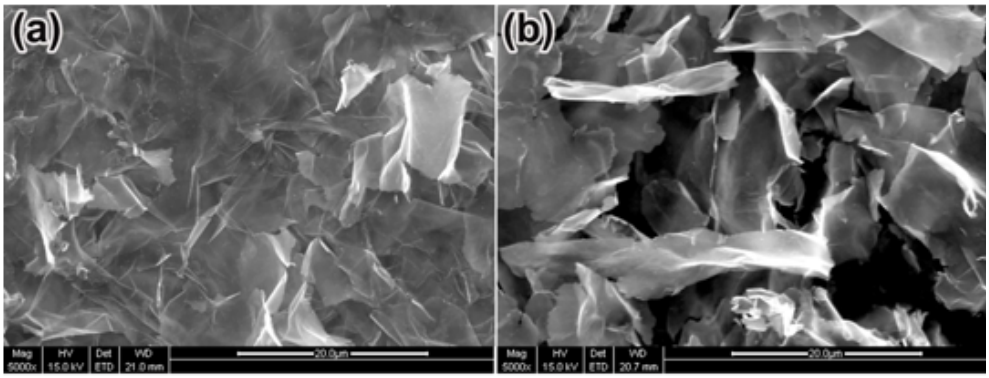

Figure 3.14. *SEM images of (a) $Ti_3C_2T_x$ and (b) A-$Ti_3C_2T_x$.*

XPS measurement was deployed to further disclose the changes in the element content of the $Ti_3C_2T_x$ anode after calcination (Figure 3.15). The broad survey reveals a decrease in fluorine (F) content from 11.0% to 7.4%, with fluorine acting as an electrochemically inert group on the surface. The removal of Ti–F bonds is expected to enhance the specific capacity of the MXene anode.

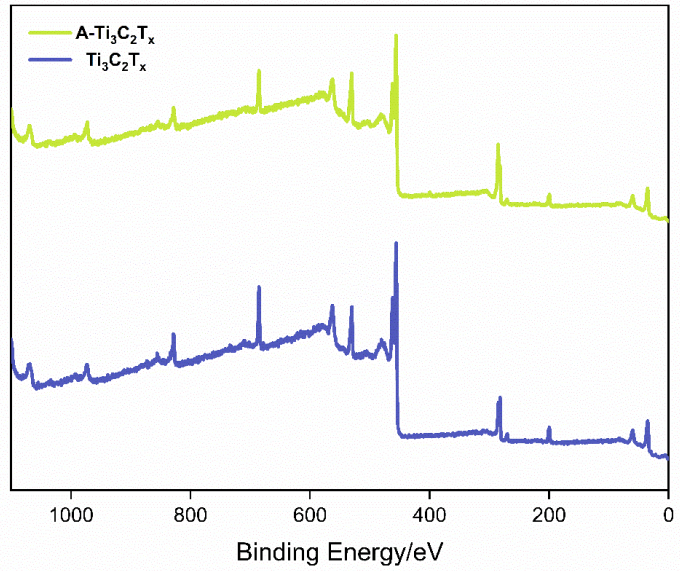

Figure 3.15. *Broad-survey XPS spectra of the $Ti_3C_2T_x$ and the A-$Ti_3C_2T_x$.*

Table 3.4 *Elemental contents of the $Ti_3C_2T_x$ and the A- $Ti_3C_2T_x$.*

Sample	C (%)	O (%)	F (%)	Ti (%)
$Ti_3C_2T_x$	47.3	17.0	11.0	24.7
A-$Ti_3C_2T_x$	51.1	21.0	7.4	20.5

3.4.5 Electrochemical performance of the A-$Ti_3C_2T_x$ anode

With a three-electrode system, the electrochemical performance of the $Ti_3C_2T_x$ and A-$Ti_3C_2T_x$ anodes was evaluated in 1 M H_2SO_4 (aq.). At a scan rate of 50 mV^{-1}, the annealed A-$Ti_3C_2T_x$ MXene electrode exhibits a larger CV integrated area compared to the pure $Ti_3C_2T_x$ MXene electrode (Figure 3.16a), indicating a significant improvement in specific capacity following the annealing process. The CV curves retain the same shape at different scan rates, suggesting a good redox reversibility (Figure 3.16b). Additionally, Figure 3.16c and d shows the capacity, which is calculated based on the GCD curves at various current densities. At current densities of 2, 4, 6, 8, and 10 A g^{-1}, A-$Ti_3C_2T_x$ exhibits specific capacities of 502, 445, 420, 411, and 384 F g^{-1}, respectively.

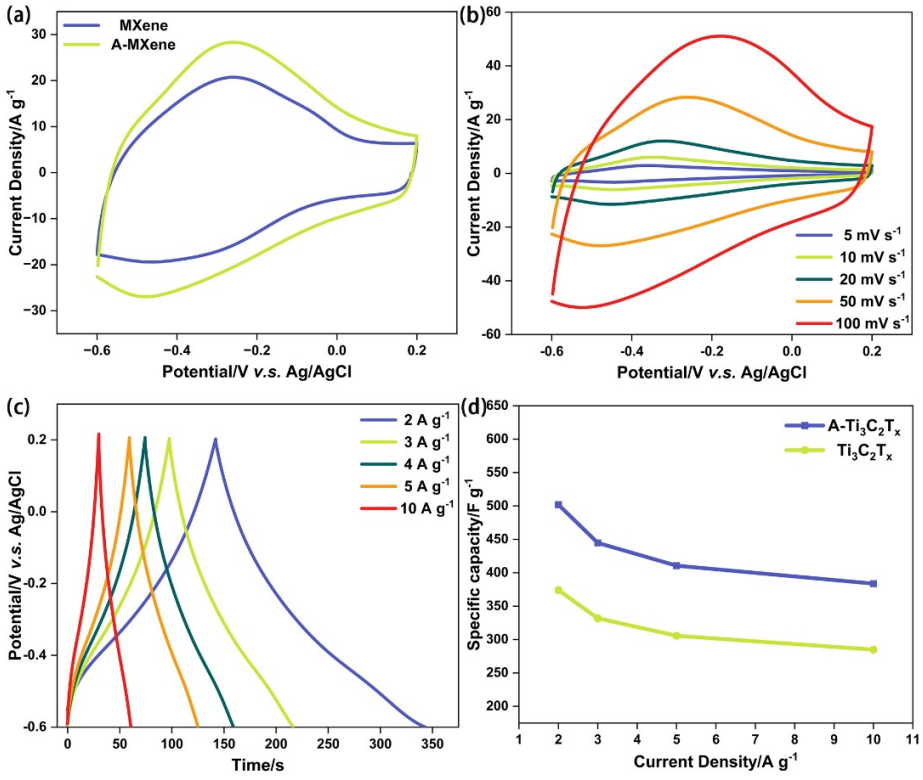

Figure 3.16. *(a) CV curves of the $Ti_3C_2T_x$ and the A-$Ti_3C_2T_x$ at 50 mV s^{-1}. (b) CV curves of the A- $Ti_3C_2T_x$ at different scan rates. (c) GCD curves of the A-$Ti_3C_2T_x$ at the current density of 2–10 A g^{-1}. (d) The specific capacity at various current densities.*

3.4.6 Electrochemical performance of the PYT/GN 4-5//A-$Ti_3C_2T_x$ asymmetric supercapacitor

The aqueous PYT/GN 4-5//A-$Ti_3C_2T_x$ ACS was assembled by using PYT/GN 4-5 as the cathode, and A-$Ti_3C_2T_x$ as the anode. The mass loading of the electrodes is determined by the equation below:

$$\frac{m^+}{m^-} = \frac{C^-V^-}{C^+V^+} \tag{3.7}$$

Here, m^+ and m^- represent the mass loadings of the cathode and anode, respectively. C^+ and V^+ denote the specific capacity and voltage operating window of the cathode, with analogous parameters for the anode.

The electrochemical performance of the assembled ASC was investigated in 1 M H_2SO_4 (aq.). To guarantee the safety of the full-cell device, the potential operating window is determined by

checking the gas evolution potential on the CV curves at 50 mV s^{-1}. When the operating voltage exceeds 1.4 V, the CV curves display a sharp peak, attributed to oxygen evolution (Figure 3.17a).[103] The CV curves of the PYT/GN 4-5//A-$Ti_3C_2T_x$ ASC display distinct oxidation and reduction peaks, attributed to proton and electron exchange occurring at the cathode and anode (Figure 3.17b). In addition, the GCD curves at different current densities show almost symmetric shapes, indicating good electrochemical stability (Figure 3.17c). The specific capacities of the PYT/GN 4-5//A-$Ti_3C_2T_x$ ASC at current densities of 1, 2, 3, 4, 5, and 10 A g^{-1} are 67.4, 63.6, 60.9, 58.6, 56.8, and 48.6 F g^{-1}, respectively. The assembled ASC demonstrated excellent cycling stability, with capacity retention of 91.4% and a high Coulombic efficiency of over 99% after 5,000 cycles (Figure 3.17d). This indicates the device's robust long-term performance. As shown in Figure 3.17, the PYT/GN 4-5//A-$Ti_3C_2T_x$ ASC achieved an energy density of 18.4 Wh kg^{-1} at a power density of 700 W kg^{-1}. Even at a maximum power density of 7,000 W kg^{-1}, the energy density remains notably high at 13.2 Wh kg^{-1}.

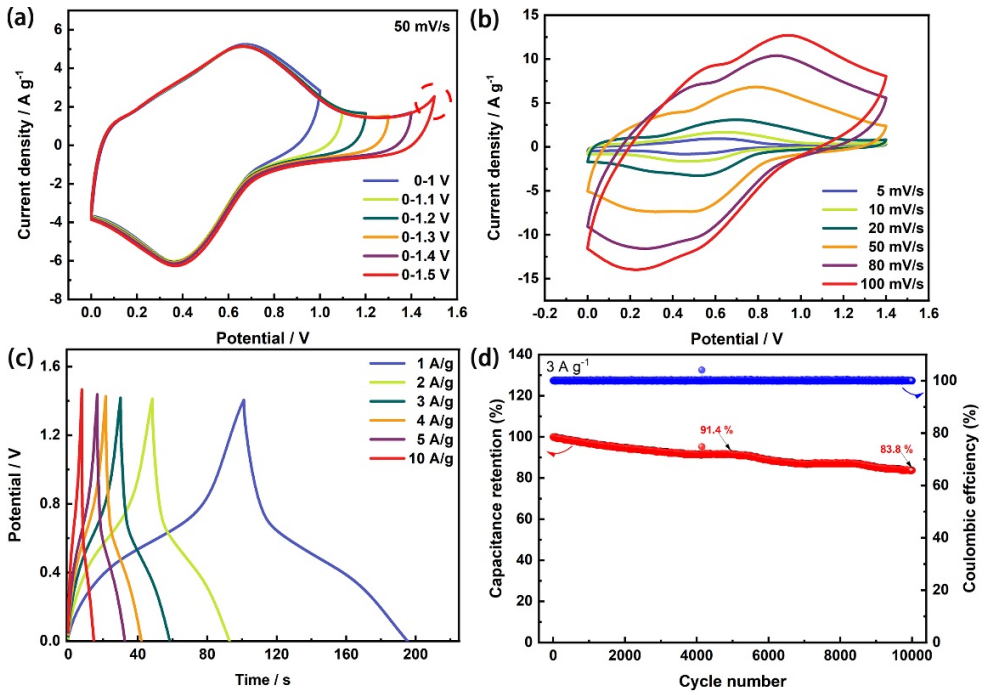

Figure 3.17. *Electrochemical performance of the as-assembled PYT/GN 4–5//A-$Ti_3C_2T_x$ ASC. (a) CV curves recorded at different potential windows. (b) CV curves at 5-100 mV s^{-1} scan rates. (c) GCD curves at 1-10 A g^{-1}current densities. (d) Cycling life at 3 A g^{-1}.*

3.4.7 Synthesis of conductive polymers with pyrazine units

The practical application of small organic molecules in aqueous energy storage devices is still limited by their low electrical conductivity and the inevitable dissolution into electrolytes during charge and discharge processes.[87, 104] Constructing polymers is one of the feasible and common strategies to address this issue. For example, polyanthraquinone can be obtained via Yamamoto coupling of 1,4-dichloro-9,10-anthraquinone. Compared to the monomer, the cycle life and rate performance are significantly enhanced.[105] In comparison, linear polymers such as polypyrrole,[106] polyanaline,[107-109] and polyindole[110] are suffering from irreversible redox reactions and the swelling of the electrodes during the charge/discharge process, which restrict the cycle life of this electrode materials.[111-112] Fusing the redox sites into aromatic systems can improve the chemical reversibility of the electrode materials.[113]

The pyrazine units are constructed by a simple condensation reaction between the PYT and tetraamine species. By changing the structure of tetraamines, three types of the polymers are designed and synthesized under the same reaction condition. The polymer named with PPYT is set as the reference structure among the three (Figure 3.18), while the polymer with two additional ketone groups is named as PPYTQ. To explore how the interaction between the polymer and graphene is affected, a sigma bond is introduced as a rotational axis. Compared to the two planar polymers, the twisted polymer, tPPYT, is expected to have weaker interactions with graphene.

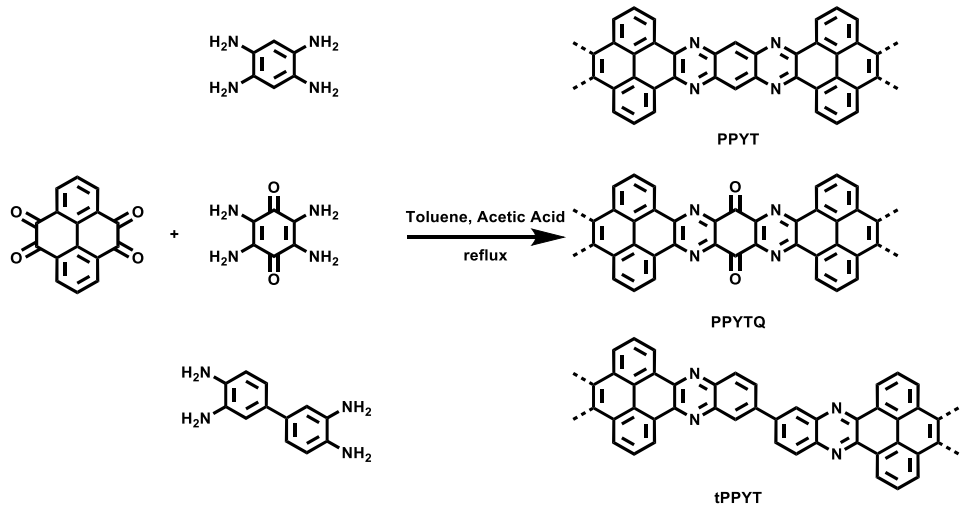

Figure 3.18. *Synthetic routes of the polymers PPYT, PPYTQ, and tPPYT.*

3.4.8 Characterization of PYT-based polymers and the corresponding composites

The size of the polymers is investigated by gel permeation chromatography (GPC). The average molecular weight (Mw) of PPYT is 39227 Daltons, while the Mw of PPYTQ is 43906 Daltons. The GPC test of tPPYT is not able to be performed due to the poor solubility in common solvents.

The polymer/graphene composite is named after the ratio of the polymers/graphene. For example, 2/1 PPYT/GN is the composite of PPYT and GN in a 2/1 ratio.

FT-IR and UV-Vis absorption spectroscopy are deployed to investigate the interaction between the redox active polymers and graphene. Figure 3.19 shows the FT-IR spectra of the polymers and the corresponding nanocomposites. The absorption bands for the C=N stretching vibration of PPYT, PPYTQ, and tPPYT can be found at 1678 cm^{-1}, 1670 cm^{-1}, and 1681 cm^{-1}, respectively. After combining with graphene, the C=N absorption band of 2/1 PPYT/GN shifts from 1678 cm^{-1} to 1662 cm^{-1}, which can be attributed to the potential π- π interaction between the two components. A similar trend can be observed in the 2/1 PPYTQ/GN composite, suggesting the interaction between the PPYTQ and GN. However, no significant absorption band in this region can be observed in 2/1 tPPYT/GN.

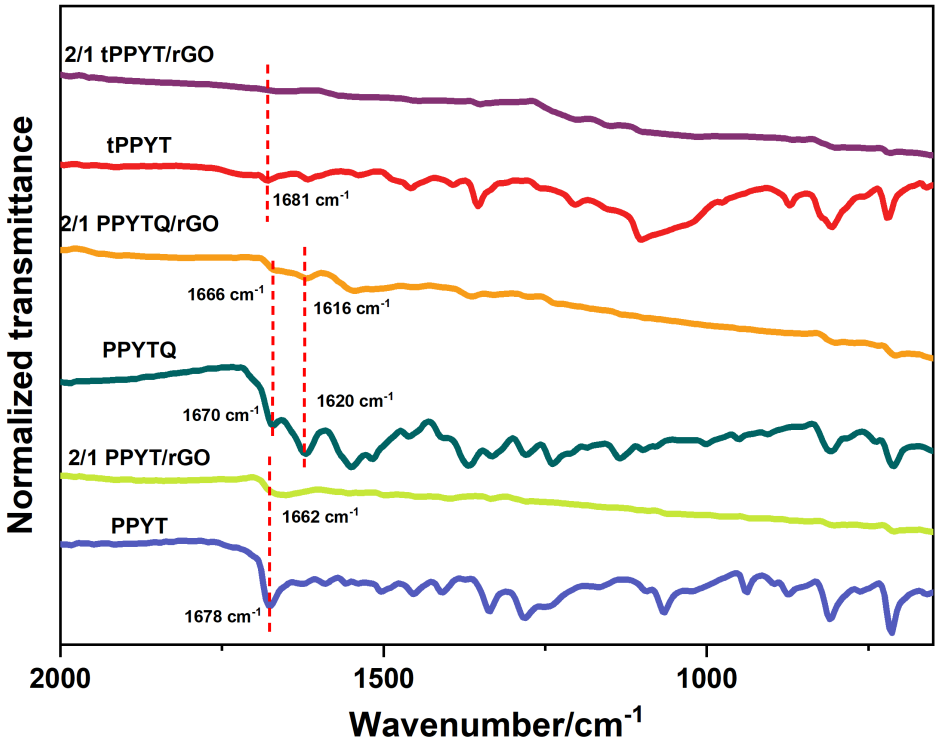

Figure 3.19. *FT-IR spectra of PPYT, PPYTQ, tPPYT, and the corresponding composites.*

The interaction between the three polymers and rGO is investigated by UV-Vis spectrophotometric titration (Figure 3.20). The UV-Vis spectrum of rGO in ethanol is set as a reference. It shows an absorption band at 271 nm which can be attributed to the π–π* transitions of rGO.[114] The PPYT polymer shows strong bands at 323 nm, 426 nm, and 490 nm. A 2 nm redshift from 323 nm to 324 nm can be observed after adding a rGO dispersion into a PPYT solution (Figure 3.20a). Besides, a 5 nm redshift from 539 nm to 544 nm is found when rGO is added to a PPYTQ solution. In contrast, the interaction between rGO and tPPYT is too weak to be detected, as no shift is observed during the titration. This result may stem from the conformational differences among the three polymers. tPPYT likely requires more energy for preorganization into a planar structure before attaching to rGO.

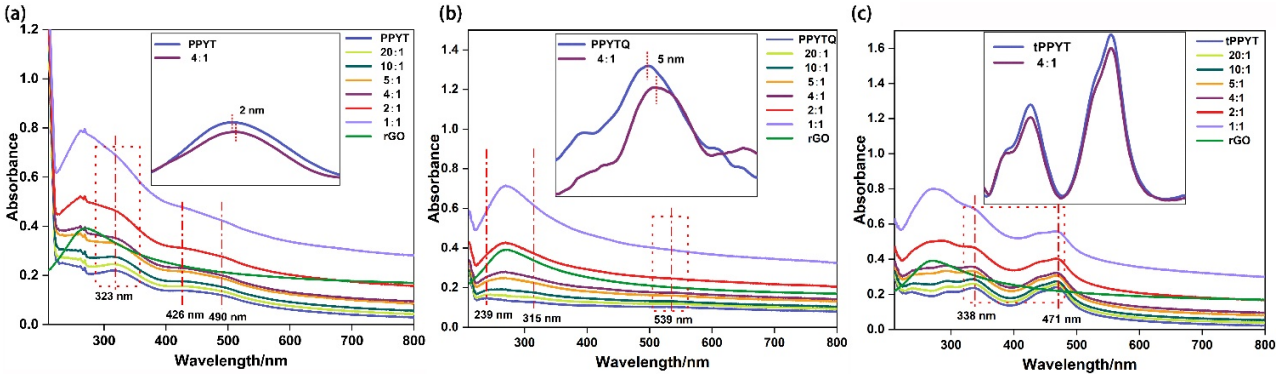

Figure 3.20. *UV-Vis absorption spectra of a titration between 0.1 mg/ml of rGO and 0.01 mg/ml of (a) PPYT, (b) PPYTQ, and (c) tPPYT in ethanol. The ratio shown in the legend is polymer/rGO.*

The elemental content of the nanocomposites is measured by XPS (Figure 3.21). As shown in Table 3.5, all the samples show C1s peaks and O1s peaks, while N1s peaks can only be observed in the materials with pyrazine groups. All the elemental content is in line with the theoretical values.

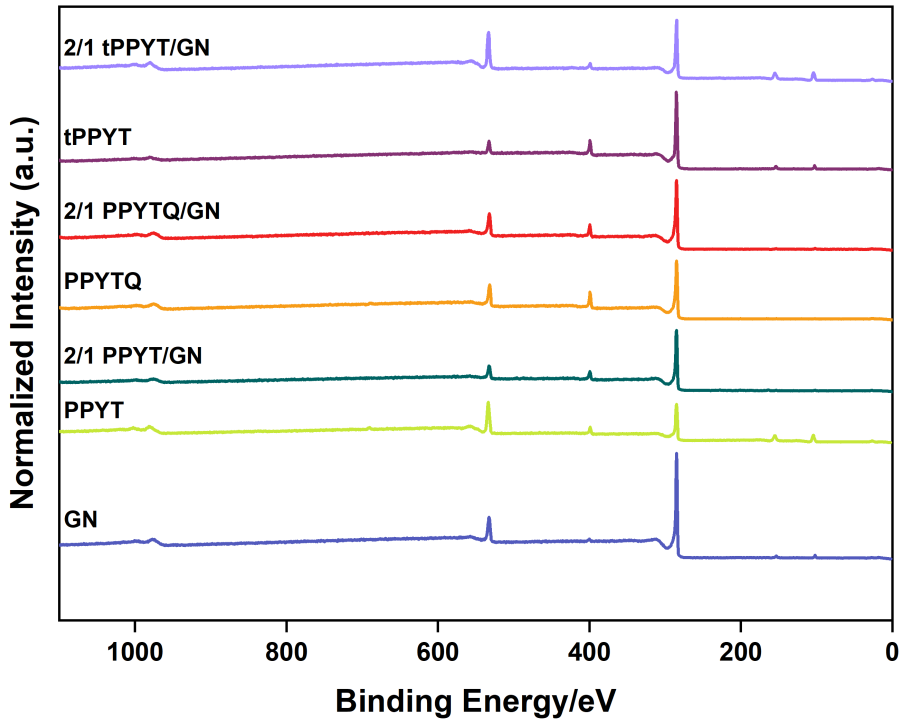

Figure 3.21. *Survey scans for all the three polymers and the corresponding nanocomposites.*

Table 3.5 *Elemental contents of all the polymers and nanocomposites.*

Materials	C (%)	O (%)	N (%)
rGO	88.2	11.8	0
PPYT	80.0	13.0	7.0
2/1 PPYT/rGO	84.3	8.9	6.8
PPYTQ	75.5	13.0	11.5
2/1 PPYTQ	78.0	13.6	8.4
tPPYT	80.5	11.7	7.8
2/1 tPPYT/rGO	77.8	15.7	6.5

Interestingly, the high-resolution N1s spectra can be fitted into two peaks at 399.6 eV and 400.7 eV after deconvolution, which can be attributed to the pyrazine nitrogen and protonated nitrogen (Figure 3.22). The protonation ratio (14.5%) of the PPYTQ polymer is the lowest among the three polymers. The possible explanation for this phenomenon is the adjacent carbonyl groups decrease the electron density of the pyrazine unit, which may lead to a lower proton affinity.

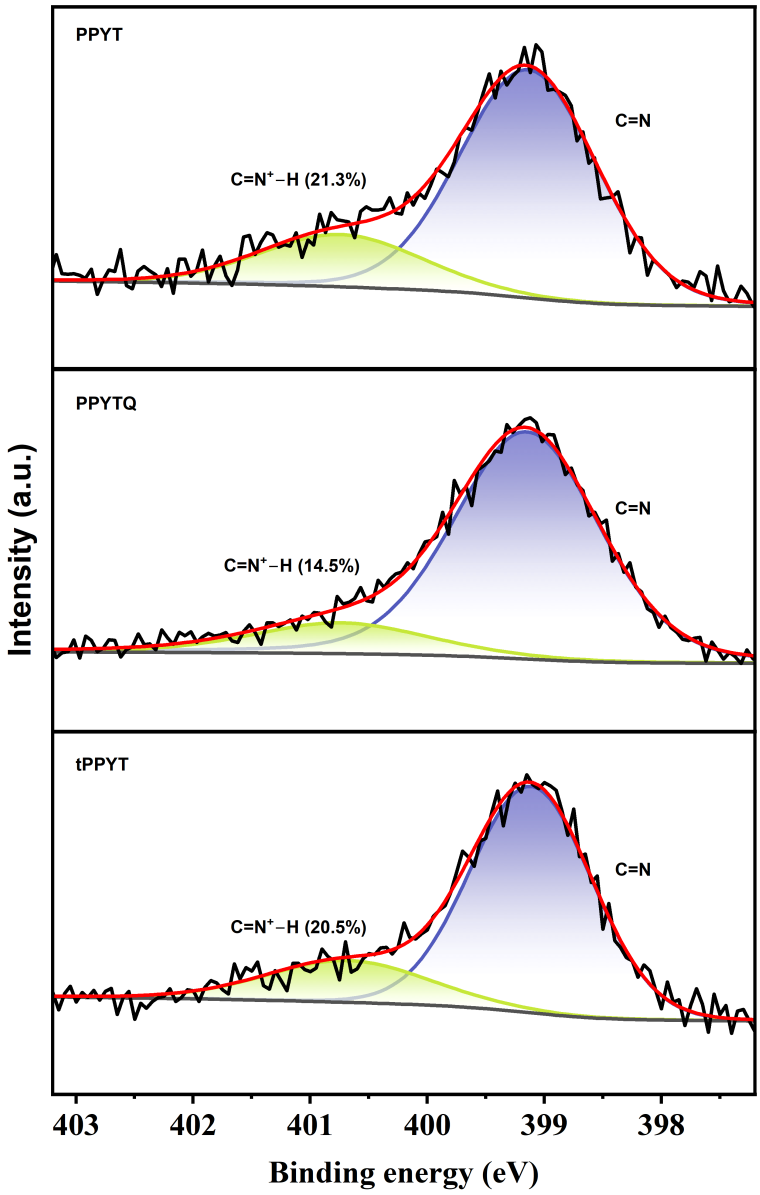

Figure 3.22. *High-resolution N1s spectra of the PPYT, PPYTQ, and tPPYT polymers.*

3.4.9 Electrochemical measurement of polymer/rGO cathodes

The electrochemical performance of the polymer/rGO nanocomposites is measured in a three-electrode system with 1 M H_2SO_4 (aq.) as the electrolyte. Compared to the PYT/rGO cathode, the PPYT/GN and PPYTQ/GN composite electrodes show a border potential operating window. In the operating window, the rGO electrode exhibits a rectangular-shaped CV curve, suggesting a EDLC mechanism (Figure 3.23a). The redox-active sites of PPYT endow the composite electrodes with a pair of redox peaks at ≈ 0.38 V/0.18 V (vs Ag/AgCl). Owing to the better conductivity,

when the redox polymer occupies a major part of the composite, the electrode can still convey a good electrochemical performance. Among all the ratios of the PPYT/rGO composites, the CV curve of 2/1 PPYT/rGO circles the largest area (Figure 3.23a). Meanwhile, the 2/1 PPYT/rGO composite exhibits the longest discharge time, indicating the highest specific capacity (Figure 3.23b). In contrast, the 3/1 PPYT/rGO electrode shows a lower specific capacity, potentially due to the limited conductivity. The CV curves of the 2/1 PPYT/rGO electrode maintain consistent shapes across various scan rates, indicating excellent redox reversibility and chemical stability (Figure 3.23c). In addition, based on the GCD curves (Figure 3.23d), the 2/1 PPYT/rGO electrode exhibits the highest specific capacities of 591, 550, 533, 520, and 508 F g^{-1} at 1–5 A g^{-1}, respectively. Interestingly, due to the limited conductivity, the 3/1 PPYT/rGO electrode shows poor capacity retention at higher current densities compared to the other ratios (Figure 3.23e). Moreover, according to equation 3.3, the b value of the 2/1 PPYT/rGO electrode are 0.68 and 0.64, suggesting the charge storage mechanism is predominantly diffusion-controlled (Figure 3.23f).

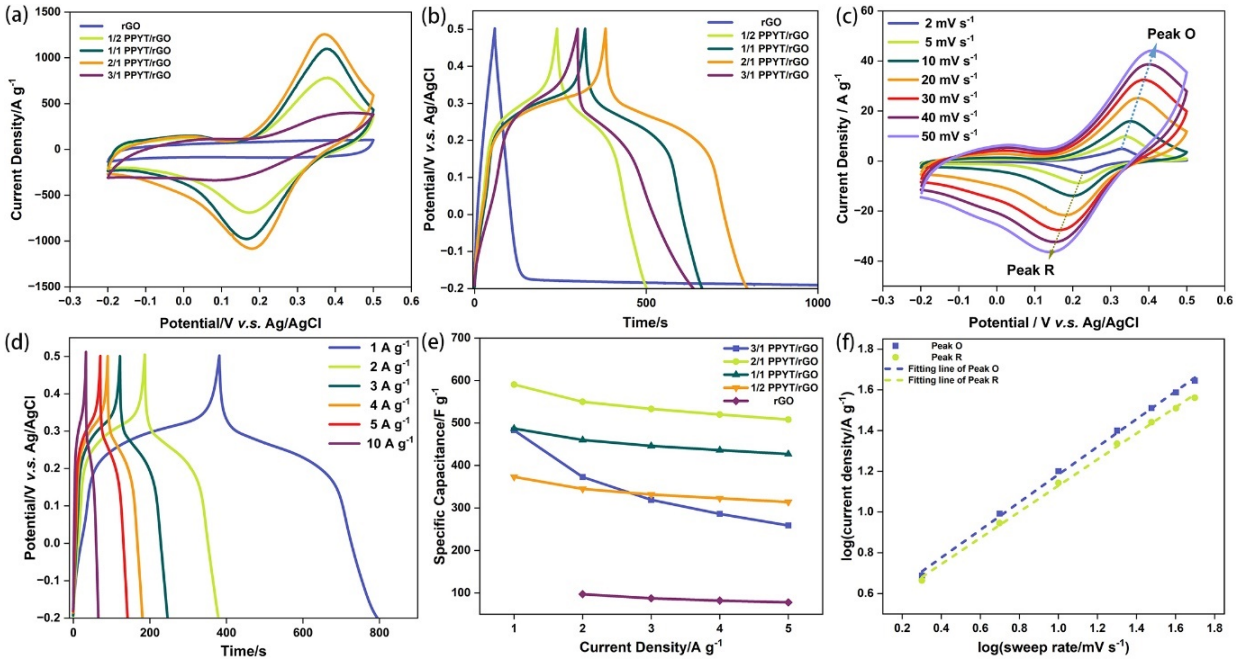

Figure 3.23. *Electrochemical performance of the PPYT/rGO electrodes at different ratios in a three-electrode system. (a) CV curves of the rGO and PPYT/rGO electrodes at 20 mV s^{-1}. (b) GCD curves of the rGO and PPYT/rGO electrodes at 1 A g^{-1}. (c) CV curves of the 2/1 PPYT/rGO electrode at different scan rates. (d) GCD curves at various current densities. (e) The specific capacity of the rGO and PPYT/rGO electrodes at different current densities. (f) log(i) vs log(v) plots according to the CV curves.*

The electrochemical performance of the PPYTQ composite electrode is evaluated in the same system. PPYTQ electrodes exhibit two distinct pairs of redox peaks at ≈ 0.26/0.13 and 0.34/0.22 V (vs Ag/AgCl), attributed to the presence of pyrazine and ketone groups, which serve as redox-active sites. Similar to the PPYT polymer, the 2/1 PPYTQ/rGO electrode shows the best electrochemical performance among all the electrode ratios based on the integration of the CV area and the discharge time in the GCD test (Figure 3.24a and b). At a scan rate from 2 – 50 mV s^{-1}, the 2/1 PPYTQ/rGO electrode maintains a consistent shape in its CV curves, indicating electrochemical reversibility (Figure 3.24c). At the current densities ranging from 1 to 5 A g^{-1}, the 2/1 PPYTQ/rGO electrode demonstrates specific capacities of 603, 511, 470, 447, and 418 F g^{-1} (Figure 3.24d). However, the rate performance of the 2/1 PPYTQ/rGO is relatively lower than the 2/1 PPYT/rGO electrode. The specific capacity at a current density of 5 A g^{-1} is only 69% of the value measured at 1 A g^{-1}, while the retention of 2/1 PPYT/rGO is 86%. As the PPYTQ polymer content decreases, the nanocomposite electrodes demonstrate improved rate performance, likely due to the increased electrical conductivity of the material (Figure 3.24e). The b-values of the four redox peaks are 0.79, 0.78, 0.78, and 0.84, indicating a mixed charge storage mechanism involving both diffusion-controlled and surface-controlled reactions (Figure 3.24f).

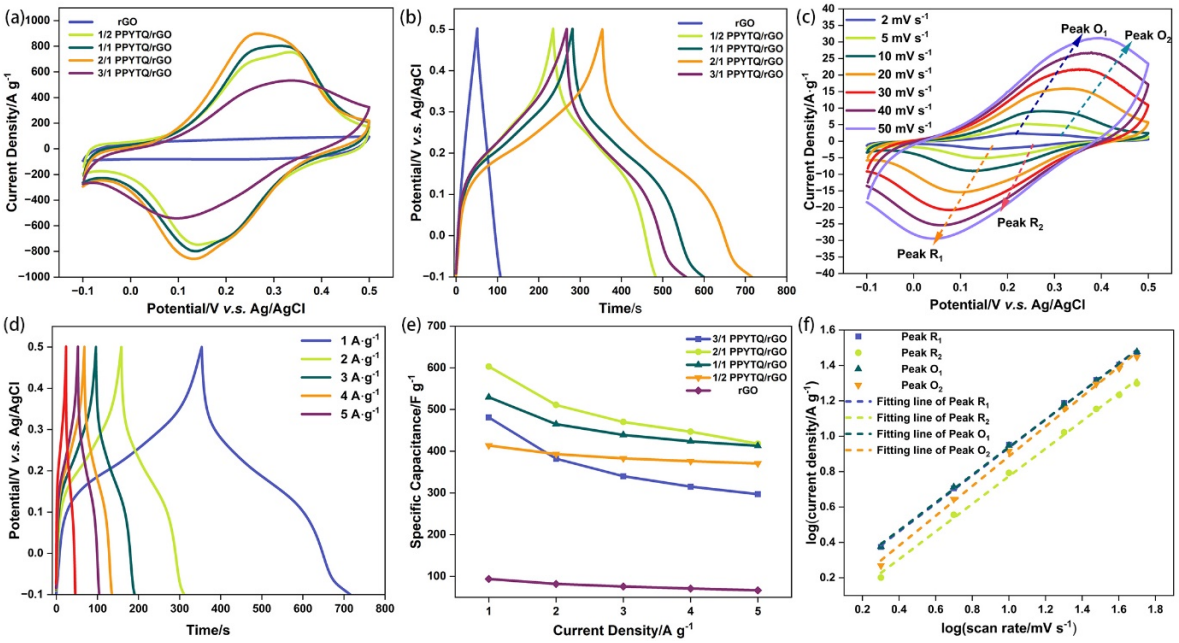

Figure 3.24. *Electrochemical performance of the PPYTQ/rGO electrodes at different ratios in a three-electrode system. (a) CV curves of the rGO and PPYTQ/rGO electrodes at 20 mV s^{-1}. (b) GCD curves of the rGO and PPYTQ/rGO electrodes at 1 A g^{-1}. (c) CV curves of the 2/1 PPYTQ/rGO electrode at different scan rates. (d) GCD curves at various current densities. (e) The specific capacity of the rGO and PPYTQ/rGO electrodes at different current densities. (f) log(i) vs log(v) plots according to the CV curves.*

Unlike composites with planar aromatic polymers, the composite material containing twisted polymer tPPYT exhibits a much narrower potential window, and a higher occurrence of electrode side reactions during charge and discharge processes (Figure 3.25).

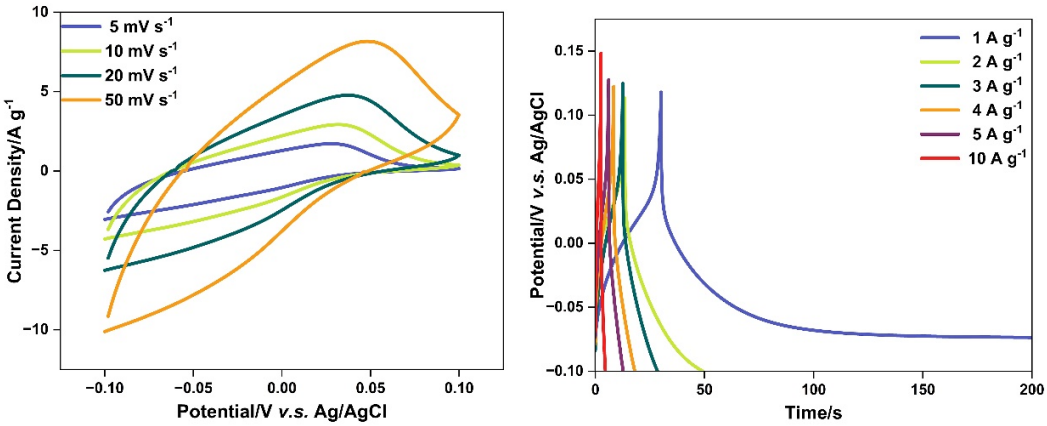

Figure 3.25. *Electrochemical characterization of the 2/1 tPPYT/rGO electrode in a three-electrode system. CV curves (left), GCD curves at 1-10 A g^{-1}(right).*

The energy storage mechanism of the three polymer/rGO composites is further investigated by EIS (Figure 3.26). The vertical line observed in the low-frequency region indicates low proton diffusion impedance and capacitive behavior. Similar to the PYT/graphene nanocomposite electrodes, the PPYT/rGO and PPYTQ/rGO nanocomposite electrodes exhibit a lower charge-transfer resistance compared to the rGO electrode. This improvement is attributed to the enhanced wettability provided by the heteroatoms present in the polymers.

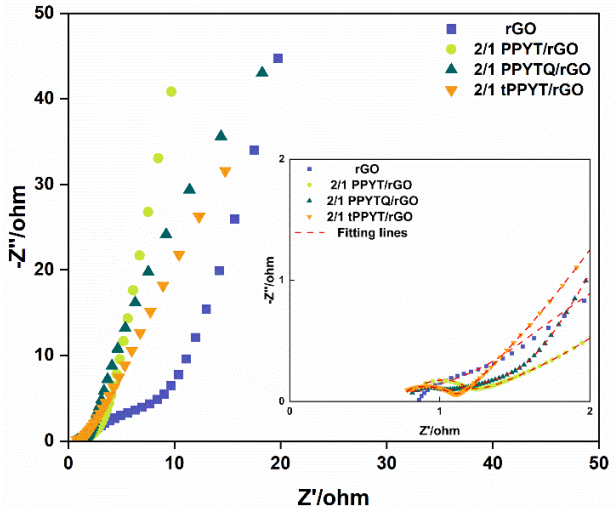

Figure 3.26. *Nyquist plots of EIS for the rGO, 2/1 PPYT/rGO, 2/1 PPYTQ/rGO, and 2/1 tPPYT/rGO.*

Table 3.6 *Impedance parameters simulated from the equivalent circuits.*

Sample	Rs (ohm)	Rct (ohm)
rGO	0.73	1.13
2/1 PPYT/rGO	0.82	0.32
2/1 PPYTQ/rGO	0.81	0.21
2/1 tPPYT/rGO	0.83	0.45

3.4.10 Electrochemical performance of the 2/1 PPYT(Q)/rGO//A-$Ti_3C_2T_x$ asymmetric supercapacitor

Using the same annealed $Ti_3C_2T_x$ electrode as the anode, the electrochemical performance of the assembled ASC is evaluated in 1 M sulfuric. Compared to the PYT/GN 4-5//A-$Ti_3C_2T_x$, the full-cell devices assembled with 2/1 PPYT/rGO and 2/1 PPYTQ/rGO exhibit wider voltage window and higher energy density. As shown in Figure 3.27a, the voltage operating window of the 2/1

PPYT/rGO//A-$Ti_3C_2T_x$ ASC can be expanded to 1.9 V in 1 M H_2SO_4 (aq.). With the increased scan rate of the CV test, the shape of the curves can still be retained even at a scan rate of 50 mV s^{-1}, indicating good stability of the device (Figure 3.27b). Based on the mass loading, the as-assembled device exhibits specific capacities of 75.9, 73.1, 70.2, 68.9, 67.5, 61.4 F g^{-1} at current densities from 1 to 10 A g^{-1}, respectively (Figure 3.27c). The device exhibits ultralong cycle life at a current density of 5 A g^{-1}. After 15000 cycles, the device can still deliver 91.3% retention with 100% coulombic efficiency (Figure 3.27d).

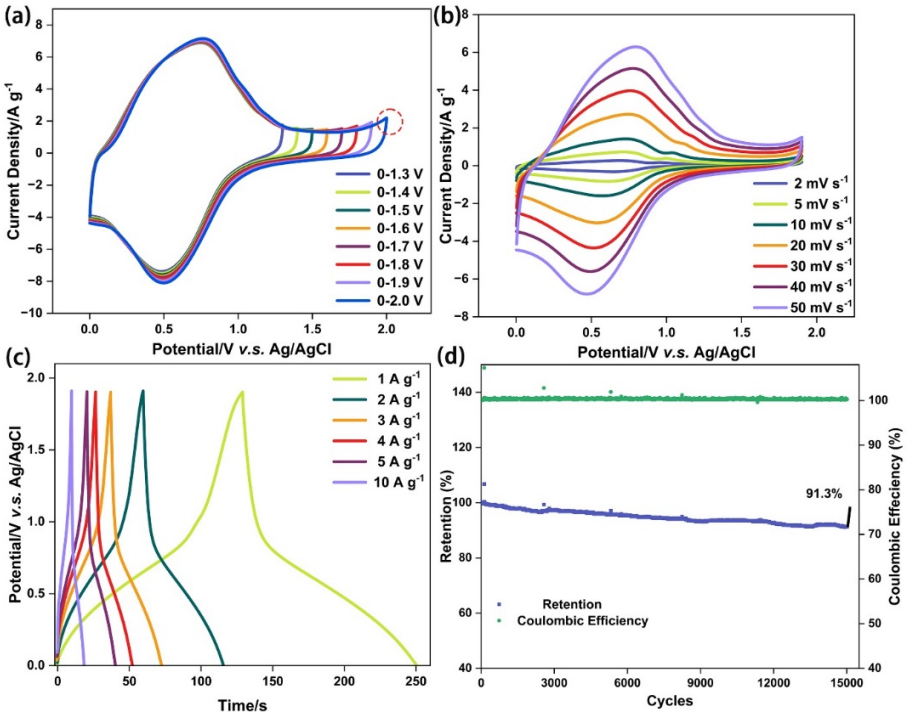

Figure 3.27. *Electrochemical performance of the 2/1 PPYT/rGO//A-$Ti_3C_2T_x$ ASC. (a) CV curves recorded at different potential windows. (b) CV curves at different scan rates. (c) GCD curves at various current densities. (d) Cycling life at 5 A g^{-1}.*

Similar to the 2/1 PPYT/rGO//A-$Ti_3C_2T_x$ device, the 2/1 PPYTQ/rGO//A-$Ti_3C_2T_x$ ASC also exhibits a 1.9 V voltage window (Figure 3.28). According to the mass loading of the cathode and anode, the full-cell device can deliver specific capacities of 64.1, 59.5, 56.1, 53.9, 52.2, and 46.3 F g^{-1} at current densities of 1–10 A g^{-1}. Moreover, after 15,000 charge/discharge cycles, the device retains 95.1% capacity, demonstrating an ultralong cycle life.

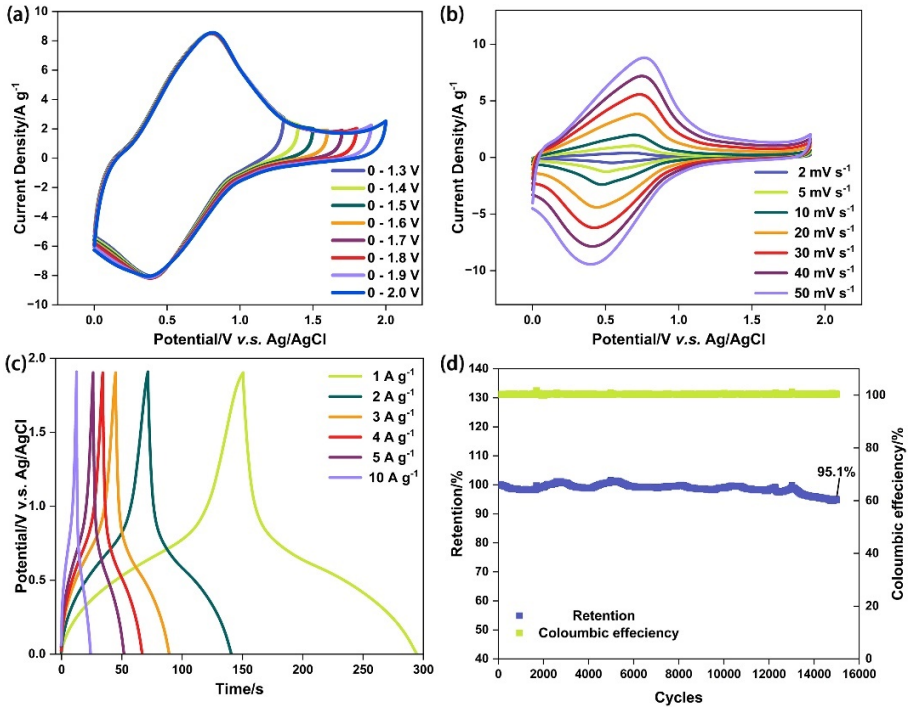

Figure 3.28. *Electrochemical performance of the as-assembled 2/1 PPYTQ/rGO//A-$Ti_3C_2T_x$ ASC. (a) CV curves recorded at different potential windows. (b) CV curves at different scan rates. (c) GCD curves at various current densities. (d) Cycling life at a current density of 5 A g^{-1}.*

3.5 Summary and future directions

In paper I, we have developed hybrid cathodic electrode materials via the noncovalent functionalization of two kinds of commercially available rGO. The interaction between PYT and rGO was confirmed by FT-IR. The optimized hybrid electrode PYT/GN 4-5 exhibits an excellent specific capacity of 711 F g^{-1} at a current density of 1 A g^{-1}. The reduced content of fluorine terminal groups in A-$Ti_3C_2T_x$ improve its electrochemical performance, achieving a specific capacity of 431 F g^{-1} at a current density of 3 A g^{-1}. The assembled PYT/GN 4-5//A-$Ti_3C_2T_x$ ASC exhibits an energy density of 18.4 Wh kg^{-1} at a power density of 700 W kg^{-1}, with a capacity retention of 91.4% after 5,000 cycles at a current density of 3 A g^{-1}, demonstrating excellent cycling stability.

In paper II, three polymers with pyrazine units based on the condensation reaction of pyrenetetraone have been developed. The spectrophotometric titration results illustrate the different assembly behaviors between graphene and the polymers, offering insights into the design of organic electrode materials. Additionally, the 2/1 PPYTQ/rGO electrode demonstrates the highest specific capacity of 603 F g^{-1} at a current density of 1 A g^{-1}. Moreover, the assembled ASC exhibits an excellent energy density of 38.1 Wh kg^{-1} at a power density of 950 W kg^{-1}, with an ultra-long cycle life.

Building on current research, we aim to design and synthesize organic materials with more refined structures to enhance charge carrier transfer. At the same time, we will focus on developing organic electrode materials for aqueous energy storage systems, broadening the range of charge carriers beyond protons.

4. Noncovalent functionalization of graphene with cutting-edge donor-acceptor organic molecules for nonlinear optical applications

4.1 Introduction and background

Nonlinear optics (NLO) is a branch of optics that studies the behavior of light in media that exhibit a nonlinear response to the electric field of the light.[115] Although the response generally necessitates high light intensity for observation (electric field > 10^8 V m^{-1}), NLO still holds significant potential for applications in photonic devices.[116-118] The usage scenarios of these devices include but are not limited to biomedical,[119-120] material processing such as ablation,[121] and large-scale fiber optic communication.[122-123] Currently, the method of information transmission that combines photons and electrons has become one of the most critical communication technologies. Achieving this requires the integration of photonic and electronic technologies to enable the mutual conversion of electrical and optical signals. Key devices facilitating this integration include optical switches and electro-optic modulators, with NLO and associated materials forming the foundation for these devices and technologies.[124-125]

4.1.1 Fundamentals of nonlinear optics

As a light goes through a transparent media, the electric field of the light will cause induced dipole moment (μ) in the molecules of the medium. The relationship between electric field amplitude of light (E) and the molecular dipole moment μ follows the equation:[126]

$$\mu(E) = \mu_0 + \alpha E + \beta E^2 + \gamma E^3 + \cdots \quad (4.1)$$

Here, μ_0 represents the intrinsic dipole moment of the molecule, while α, β, γ, etc., correspond to the molecule's first-order, second-order, and third-order polarizabilities, respectively. Additionally, all the terms in the formula are vectors, i.e., they have a specific direction in space.

It is worth mentioning that under low light intensity, the terms behind αE in equation 4.1 are neglectable, which means the dipole moment of the molecules μ has good linearity with the electric field of the light. In contrast, when the light intensity is high enough, the as-mentioned terms cannot be neglected, μ and E exhibit a nonlinear relationship. To quantify the dipole moment of the medium, the concept polarization of the medium (P) is defined as the dipole moment per unit

volume. In the normal medium, the polarization of the medium P shows good linearity with the intensity of the external photoelectric field E, which follows the equation:

$$P = \varepsilon_0 \chi^{(1)} E \tag{4.2}$$

The $\chi^{(1)}$ is the linear susceptibility, ε_0 is the permittivity of free space. With the higher intensity, the higher-order terms should be counted, the equation is modified to:[127]

$$P = \varepsilon_0 \left(\chi^{(1)} E + \chi^{(2)} E^2 + \chi^{(3)} E^3 + \cdots \right) \tag{4.3}$$

The value of linear susceptibility, $\chi^{(1)}$, is significantly larger than the nonlinear susceptibilities, $\chi^{(n)}$ ($n \geq 2$). Thus, the contribution of the nonlinear term in Equation (4.3) becomes non-negligible only in the presence of strong photoelectric fields. Since the invention of the laser, the field of NLO has advanced rapidly, with a particular focus on second-order and third-order NLO effects. Second-order NLO processes include second harmonic generation (SHG), sum-frequency generation (SFG), difference-frequency generation (DFG), and parametric oscillation.[128-129] Third-order NLO processes include third harmonic generation (THG), two-photon absorption (TPA), etc.[130]

a. Second-order NLO

The second-order NLO properties of a molecule are closely related to its symmetry. Such properties require the molecule to exhibit asymmetry or belong to a non-centrosymmetric space group.[131-132] The second harmonic generation is the NLO effect that is observed the earliest (Figure 4.1a). In 1961, Franken et al. observed that when a ruby laser with a wavelength of λ_1 = 694.3 nm passed through a quartz crystal and was subsequently split by a prism, a frequency-doubled light with a wavelength of λ_2 = 347.15 nm can be generated.[133] This phenomenon was named as SHG or optical frequency doubling, resulting from the interaction between the incident light and the NLO material (such as quartz crystal). In SHG, pairs of photons with the same frequency combine to produce photons with double the frequency and energy. This effect is one of the most widely used second-order NLO processes.[134] The SHG effect is a valuable spectroscopic technique for analyzing the surface chemical and physical properties of centrosymmetric materials.[135] Since its development in 1981, SHG spectroscopy has been effectively utilized to investigate surface and interface properties across a wide variety of materials.[136] In biological imaging, for instance, SHG can be applied to fluorescence microscopy, enabling detailed imaging of animal tissues and live organisms.[120]

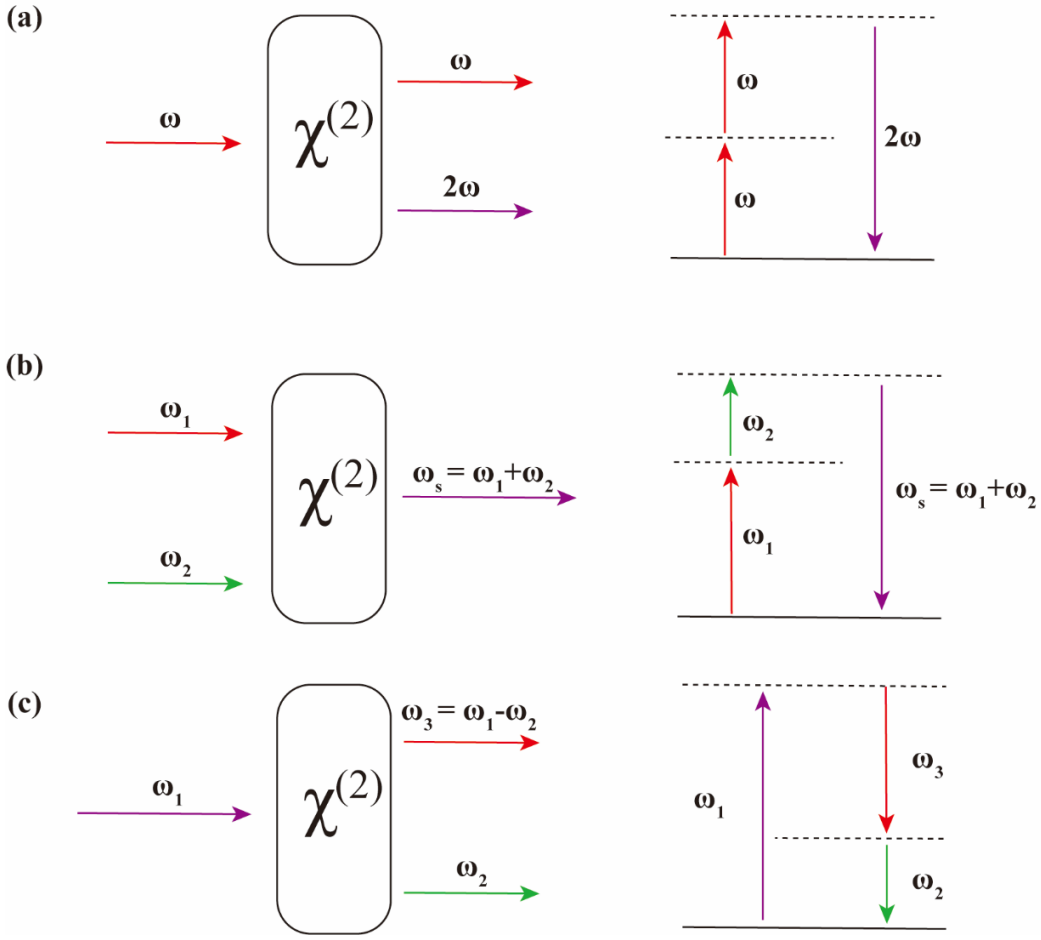

Figure 4.1. *Representation of the second order NLO process (a)SHG, (b)SFG, (c)DFG, and the corresponding energy level diagram.*

Figure 4.1b shows a process that is related to SHG called SFG, where two photons with different frequencies (ω_1 and ω_2) combine to give a single photon with frequency of ($\omega_1 + \omega_2$). It is an important phenomenon to obtain tunable lasers. As a reverse process of SFG, two protons with different frequencies (ω_1 and ω_2) went through the medium, resulting into an output photon with a frequency of $\omega_1 - \omega_2$ (Figure 4.1c). This process is called DFG.

b. Third-order NLO

Third-order and other odd-order NLO effects are not constrained by symmetry requirements.[137] Similar to the SHG, third harmonic generation is a process that three photons with frequency ω interact within a NLO material to generate a single photon with a frequency of 3ω. Another third-order nonlinear effect is called optical Kerr effect. It describes the change in a material's refractive

index in response to varying light intensity. The change in refractive index is according to the following equation:

$$\Delta n = \left(\frac{3\chi^{(3)}}{4c\varepsilon_0 n^2}\right) l \tag{4.4}$$

Here, Δn represents the change in refractive index, *n* denotes the linear refractive index, *I* is the light intensity.

When a molecule simultaneously absorbs two photons, it transitions from the ground state to an excited state—a process known as two-photon absorption (2PA). It is usually accompanied with a fluorescence emission which is known as two-photon excited fluorescence (TPF).[138] The process by which a molecule absorbs two photons to transition from the ground state to an excited state can be described as follow: the molecule initially absorbs one photon, moving from the ground state to a virtual energy state. Subsequently, it absorbs a second photon, enabling the transition from this virtual state to the excited state. Notebly, NLO processes such as SHG, SFG, DHG, THG, and optical Kerr effect are parametric processes, during which the quantum state of the materials remain unchanged. In contrast, TPA is a non-parametric process, which involves the transfer of energy between photons and the NLO material, exciting the material from the ground state to a real excited state.

4.1.2 Nonlinear optical materials

All materials exhibit NLO responses under sufficiently intense laser irradiation. However, the response of NLO materials is significantly stronger. NLO materials can be broadly categorized into inorganic and organic types based on their compositions.

Inorganic NLO materials plays a vital role in the early-stage study of this field. Typical inorganic NLO materials include perovskite crystals like lithium niobate ($LiNbO_3$),[139-140] phosphate crystals such as potassium dihydrogen phosphate (KH_2PO_4),[141] borate crystals like lithium triborate (LiB_3O_5),[142] and semiconductors such as cadmium sulfide (CdS).[143] The NLO response of inorganic materials arises from lattice vibrations or electron-hole recombination, resulting in a relatively slow response speed. Additionally, high-quality crystal growth for these materials is challenging and costly to achieve.[144] Furthermore, the low photoelectric coefficient of inorganic materials limits their applicability in various optical and electronic applications.[145] Beyond these

materials, 2D materials are promising candidates for NLO applications. Graphene has been shown to exhibit excellent saturable absorption characteristics and NLO properties since around 2009.[146-147] With the rapid advancement of 2D materials, the development of novel optical devices based on these materials has also accelerated.[148-149]

Organic NLO materials have gained significant research interest due to their high NLO coefficients, rapid response, and good structure tunability.[150] Additionally, their molecular structures and synthesis processes are relatively straightforward, making them well-suited for simple solution-based processing methods.[151] These characteristics position organic small molecules as highly promising candidates for NLO applications. Via studies of the SHG phenomenon in benzopyrene[152] and various coumarins[153] with electron-donating and electron-withdrawing groups, it has been proven that organic compounds containing π-electrons exhibit strong NLO responses. With the introduction of electron donor, electron acceptor, and conjugated π-bridge concepts, along with a series of exploratory experiments, the intramolecular charge transfer (ICT) characteristics[154-155] and transition dipole moment[156-157] in the D-A or donor-π-acceptor molecules have been proven to enhance NLO activity. The typical D-A molecules for NLO are *N,N*-dimethyl-4-[2-(4-nitrophenyl)vinyl]aniline (DANS)[158] and *p*-nitroaniline (PNA).[159] Later on, various structures including diphenylene and diphenylacetylene, Schiff base, azo compounds, and diphenylketene, have been employed in organic NLO materials.

4.1.3 Structural design of NLO materials

For a certain molecular skeleton, the stronger electron-donating and withdrawing groups enhance the second-order nonlinear optical response, which can be attributed to the prompt charge transfer within the molecule under an external field.[159-160] In addition, The molecular conjugated structure, including factors such as the area and planarity of the conjugation system, can significantly influence the molecular NLO response. The increased area and planarity of the conjugation system will enhance the delocalization of the π electrons, which will increase the dipole moment change, thereby increasing the nonlinear polarizability. Thus, structural design of organic NLO molecules should consider enhancing the electron donating or withdrawing groups, and proper design of the conjugation system. The theory model of the D-A molecules for the third-order NLO effect is more complicated.[161] While all the factors mentioned above that can affect the third-order NLO response, the structure-property relationship remains unclear.

2D materials such as graphene, MXene, and black phosphorus exhibit remarkable optical properties such as high electron mobility, board band optical response, and strong excitonic effects.[162-165] Functionalization of graphene with π-conjugated molecules that increase the electron/charge transfer capabilities can significantly enhance the NLO performance of the graphene-based NLO materials.[166-167] The charge separation/recombination occurs between graphene and D-A moieties can largely enhance the delocalization of electrons, which can further improve the NLO properties of graphene in the hybrid materials.

4.2 Aim

The aims of this thesis in the field of NLO materials were to:

- Design and synthesize a series of D-A molecules based on the functionalization of pyrene-4,5,9,10-tetraone.
- Investigate the interaction between the organic D-A species and graphene.
- Study the relationship between the symmetry of the D-A molecules and the NLO effect of the hybrid materials.

4.3 Result and discussion

4.3.1 Synthesis of donor-acceptor molecules

a. Construction of D-A skeleton

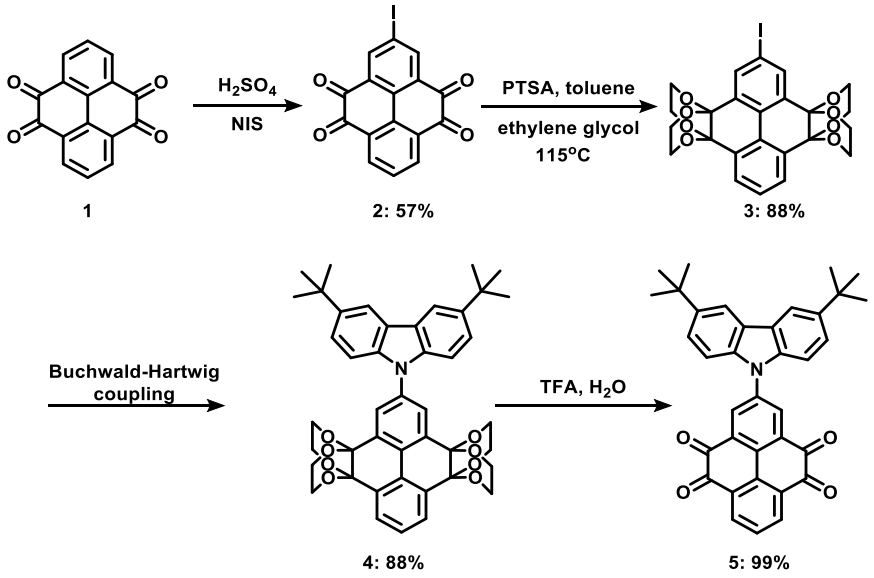

Figure 4.2. *The synthetic route of 2-carbazole-pyrene-4,5,9,10-tetraone.*

As mentioned in chapter 3.4.1, PYT was obtained via the K-region oxidation of pyrene, which can be prepared on a gram scale. The 2-functionalization of pyrene-4,5,9,10-tetraone is achieved by the direct iodination with *N*-iodosuccinimide (NIS) in sulfuric acid.[168-169] By adding insufficient equivalents of NIS, the 2,7-bifunctionalized PYT is inevitably obtained from the reaction. In the end, by adding 1.5 equivalents of NIS, product **2** can be obtained with a yield of 57%. Before the coupling reaction, **2** is protected by acetalization reaction to avoid the interfere to the palladium-catalyst in the coupling reaction. The acetalization is achieved by refluxing **2** with ethylene glycol in toluene in the presence of *p*-toluenesulfonic acid (PTSA). Using Buchwald-Hartwig coupling, 3,6-di-tert-butylcarbazole is introduced as the donor component of the system. Employing $Pd_2(dba)_3$ as the catalyst precursor and tri(*tert*-butyl)phosphine as the ligand, compound **4** is obtained with an 88% yield. Subsequent deprotection of compound **4** is carried out in a 9:1 mixture of trifluoroacetic acid and water, yielding compound **5** with a high efficiency of 99%.

b. The build of symmetirc acceptors

According to the work from Mateo-Alonso and his co-workers, the extension of the π system can be achieved by a condensation reaction with 2,3-diaminomaleonitrile and various substituted *o*-phenyldiamine in a mixture of acetic acid and other solvent.[41, 170-171]

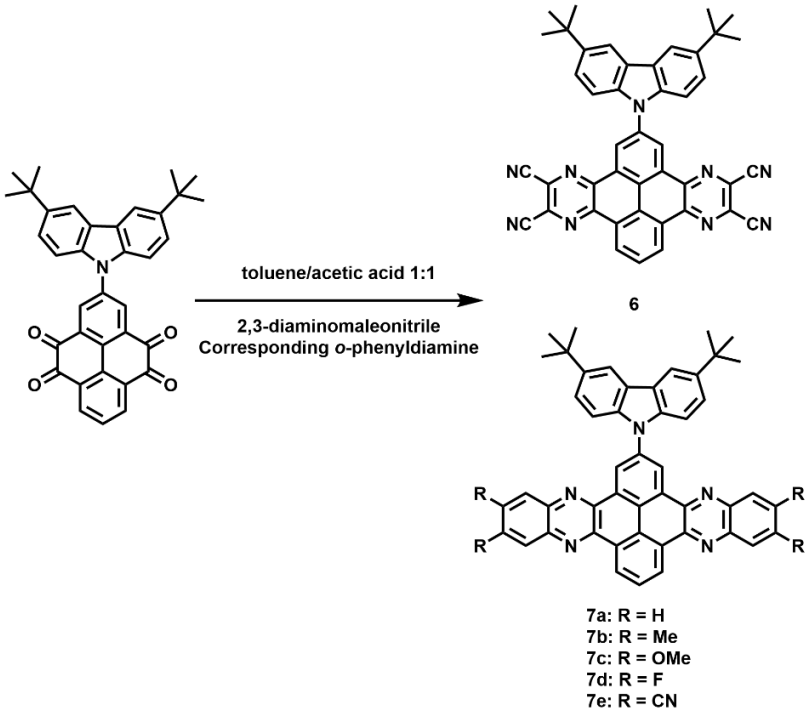

Figure 4.3. *The construction of symmetric D-A molecules.*

Notably, due to severe π-π stacking interactions, it is not possible to get **7a** – **7d** in solution, not even for thin-layer chromatography. However, with the existence of cyano-groups, the solubility of the compound is significantly increased.

c. The building of asymmetric acceptors

Since the cyano- group can significantly increase the solubility of the D-A molecule and impart π-accepting properties, 4,5-dicyano-1,2-phenyldiamine is an excellent choice for the synthesis of asymmetric acceptor (Figure 4.4).[171] With the same reaction condition for the symmetric acceptor, when the equivalent of the diamine decreases to one, the asymmetric acceptor can be obtained with an approximate 45% yield, remaining the bare diketone groups for further functionalization.[172] Based on the reported reaction condition, the final reaction mixture contains compounds **5**, **6 (7e)**, and **8 (9)**. Among these compounds, the mixture of **5**, **7e**, and **9** is challenging to isolate using

chromatography and recrystallization, owing to their similar polarity and solubility. Product **9** was initially isolated through 2D preparative thin-layer chromatography (2D PTLC).

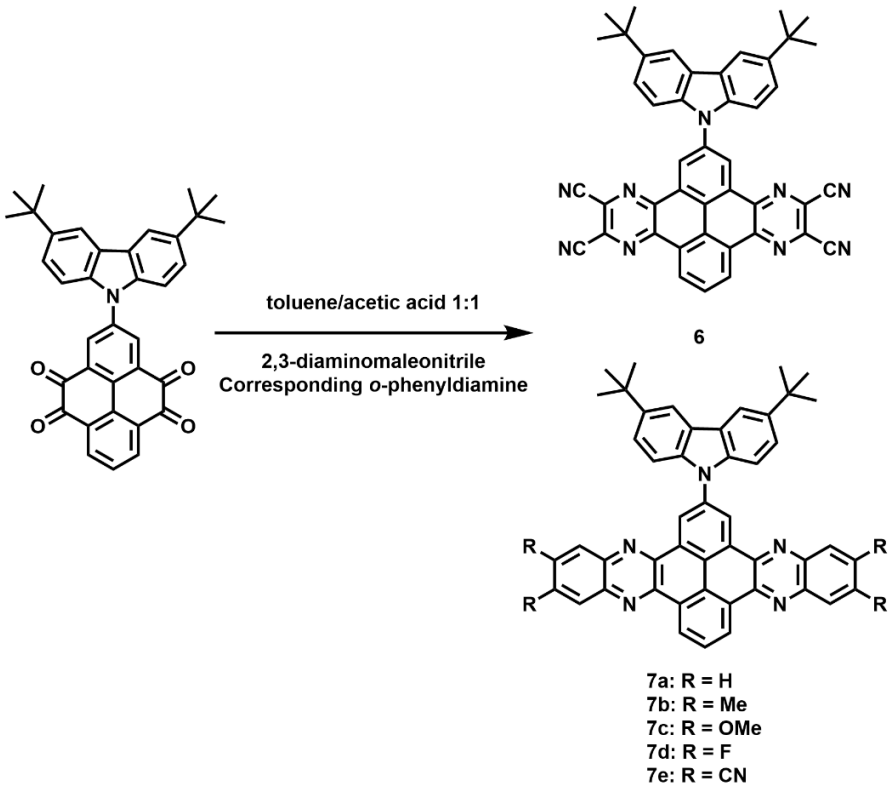

Figure 4.4 *The construction of asymmetric precursor.*

Later on, owing to the limited solubility of **9** in ethyl acetate, ethyl acetate was used to precipitate **9** from the reaction solution. When the acetic acid content is decreased to 10%, the formation of **7e** can be inhibited.

Following the established protocol, asymmetric structures shown in Figure 4.5 were synthesized for photophysical testing and subsequent assembly with graphene.

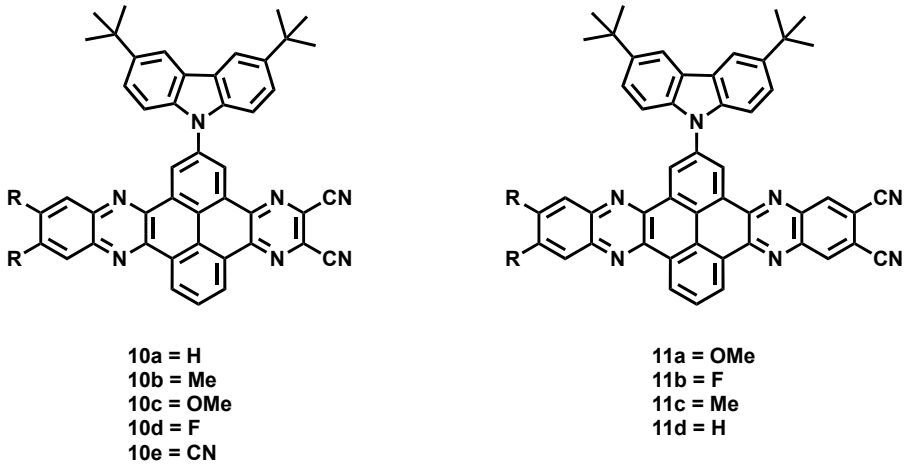

Figure 4.5. *The construction of asymmetric D-A molecules.*

4.3.2 Study on the interaction between donor-acceptor molecules and graphene

The interaction between the D-A moieties and graphene is investigated via UV-Vis absorption and IR spectroscopy. UV-Vis spectrophotometric titration is deployed to study the interaction between the obtained D-A species and graphene. The experiment was performed by adding a 2.5 μM D-A molecule solution into a 0.01 mg/ml rGO dispersion using UV-Vis absorption spectroscopy.

Figure 4.6 (a-d) exhibit the titration results of the symmetric compound **7e** and the asymmetric moieties **11a**, **11b**, and **11d**. Compound **7e** is used as a good example to explain the process and data analysis of spectrophotometric titration between the D-A molecules and graphene. The titration was performed by adding compound **7e** into a 0.01 mg/ml rGO dispersion as the experimental group and to an equal volume of blank solution with same gradient as the control group. For the experimental group, the absorption of rGO is subtracted as the background signal from the curves. Compared to the control group, a 2 nm redshift from 322 nm to 344nm is observed, corresponding to the π-π* transition of the acceptor, indicating a charge/electron/energy transfer process between the compound **7e** and rGO.[173] The assembly behaviour between compound **7e** and rGO is saturated when 1.0 μM **7e** is added into a 0.01 mg/ml rGO dispersion. Similar redshifts can also be observed between the asymmetric species **11a**, **11b**, **11d**, and rGO. Among all the asymmetric D-A compounds, compound **11a** shows the highest redshift value from 327 nm to 330 nm. The stronger intensity of the interaction can be attributed to the existence of the two methoxy groups. With the strong electron-donating groups, compound **11a** exhibits the largest dipole

moment among all the D-A moieties. The saturation concentration of **11a** is 2.5 µM against 0.01 mg/ml rGO, the highest among the tested D-A systems. As for other moieties, smaller shifts on the absorption are observed during the titrations, indicating a weaker interaction between those D-A moieties and rGO. At 1.0 µM, compound **11b** exhibits a redshift from 319 nm to 321 nm, while compound **11d** shows a similar redshift from 320 nm to 322 nm. The saturation concentration of **11d** is 1.5 µM against 0.01 mg/ml rGO in chloroform. In contrast, no shift in the absorption bands is observed during the titration of compound **11c**. One possible explanation is that steric hindrance from the methyl groups cannot be alleviated through sigma bond rotation.

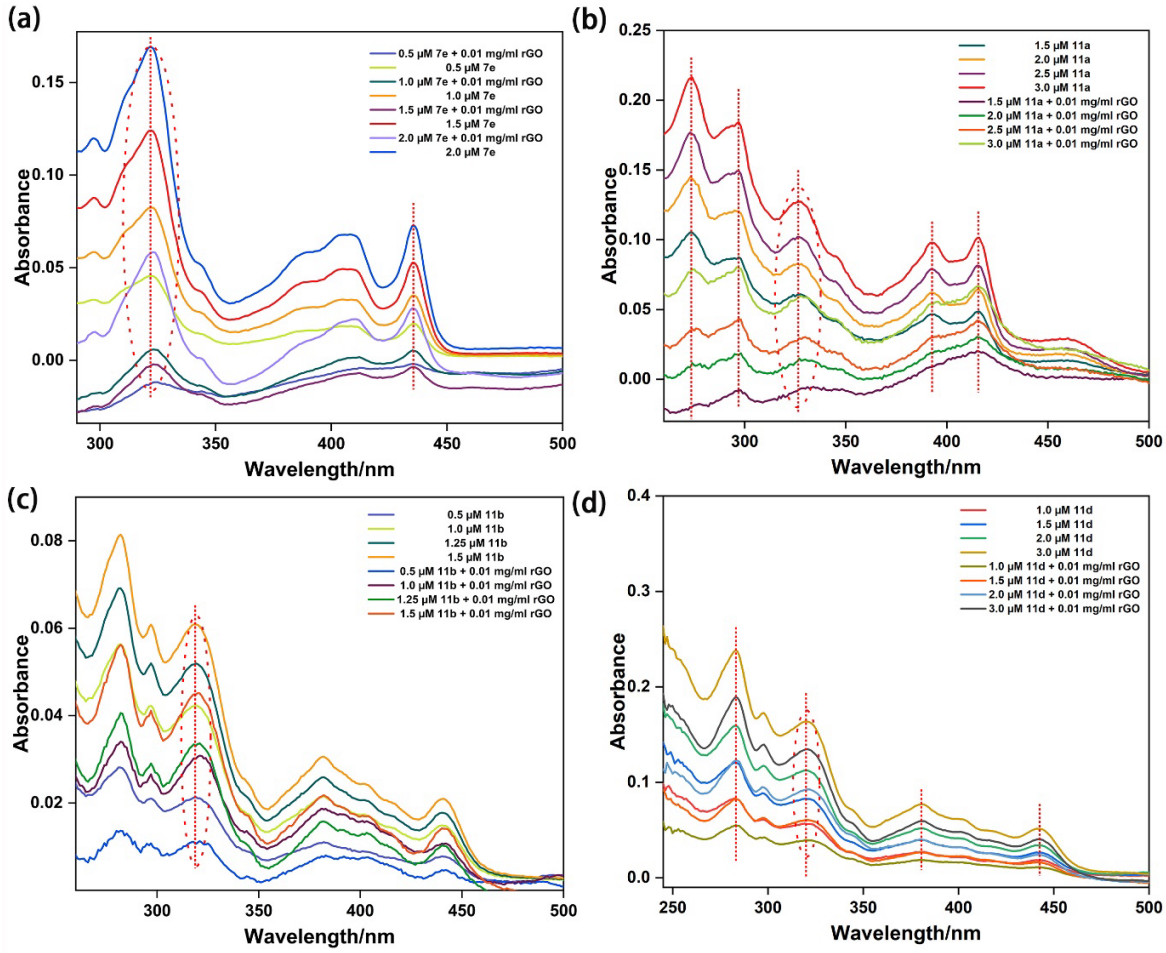

Figure 4.6. *UV-Vis spectrophotometric titration spectra of (a) compound **7e**, (b) **11a**, (c) **11b**, and (d)**11d**.*

Another interesting phenomenon is the difference in the saturation concentration. Compound **7e**, **11a**, **11b**, and **11d** has the same -CN groups at one side of the acceptors which are strong electron withdrawing groups. The low-lying LUMO of the acceptors may help the electron transfer from

graphene surface to the acceptors. Using compound **11d** (-H) as a reference, **11a** (-OMe) has a higher lying LUMO, resulting less electron transfer with the graphene surface. Consequently, the electron density of the hybrid formed with **11a** is higher than that of the corresponding hybrid with **11d**. Therefore, graphene can potentially accommodate more **11a** molecules than **11d** molecules, leading to a higher saturation concentration. The same principle applies to compound **7e** and compound **11b**.

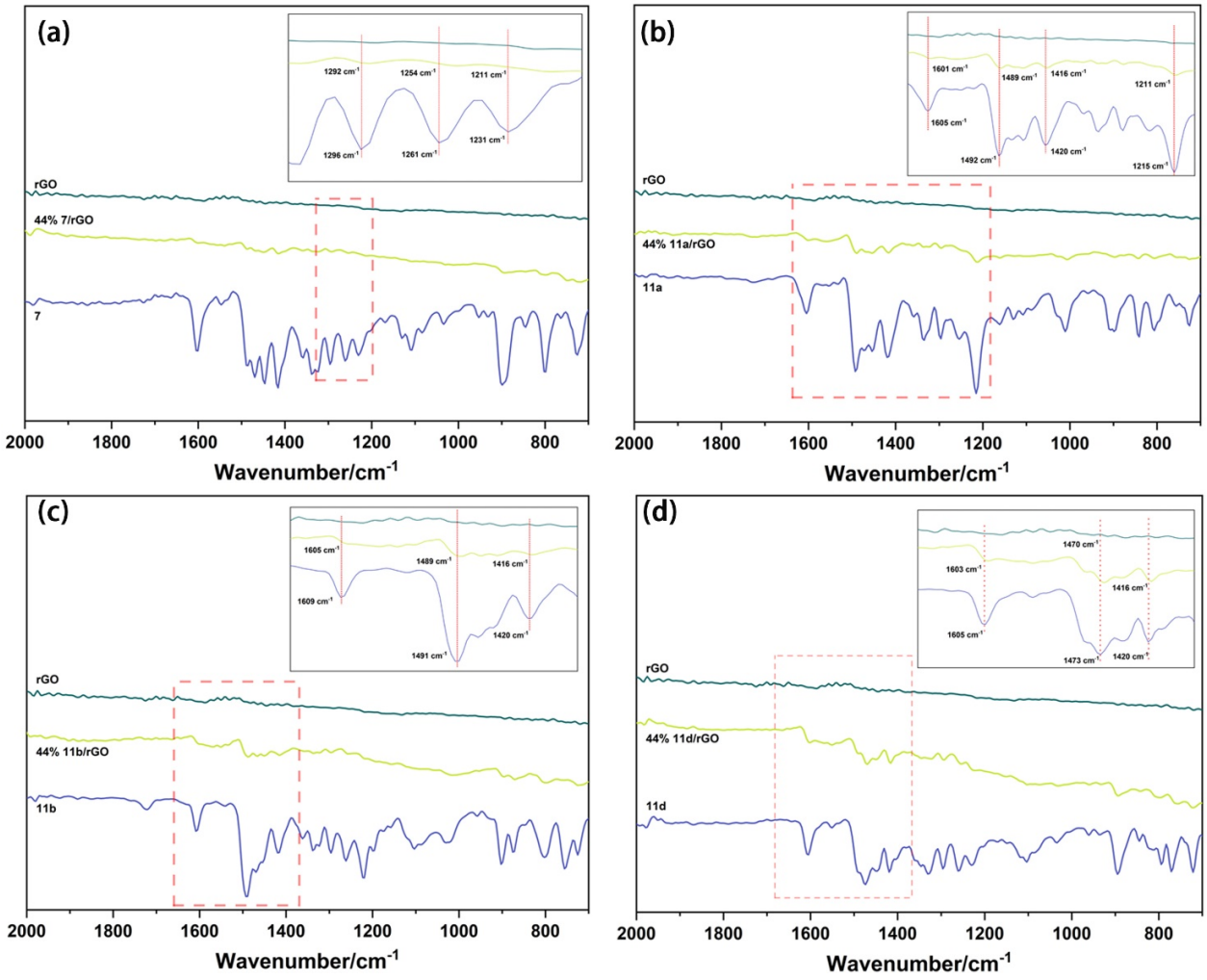

Figure 4.7. *IR spectra for compound (a)* ***7e****, (b)* ***11a****, (c)* ***11b****, (d)* ***11d****, and the corresponding composites.*

The interaction between the D-A molecules and rGO is further investigated through IR spectroscopy measurements. Figure 4.7 exhibits the IR spectra of the D-A molecules and the corresponding nanocomposites with rGO. To increase the signal of the molecule in the composite, the content of the D-A moieties is increased to 45 wt%. The shifts in the IR bands observed in the

1650–1100 cm^{-1} range across all composite samples correspond to the C=C double bond stretching and C-H bending regions. For example, compound **7e** exhibits absorption bands at 1296, 1261, and 1231 cm^{-1}, respectively. After mixed with rGO, the absorption bands shift to 1292, 1254, and 1211 cm^{-1}. Similar shifts can also be observed in the other hybrid samples. This indicates that graphene can potentially restrict the vibrational motions of the chemical bonds within the D-A molecules.

4.4 Summary and future directions

We have finished the synthesis and characterization of novel PYT-based D-A molecules with different symmetry. Their interactions were investigated by UV-Vis spectrophotometric titration and IR spectroscopy. Further work will involve the measurement of NLO effects of the hybrid materials.

5. Conclusion and outlook

In this thesis, A series of small organic molecules and polymers has been synthesized, using pyrene-4,5,9,10-tetraone (PYT) as the building block for electrode materials in aqueous energy storage devices. In addition, novel PAH donor-acceptor systems have been designed and synthesized. Furthermore, the resulting materials are evaluated from various perspectives to pursue valuable insights into the design of organic materials for applications in energy storage and optoelectronics.

In paper I, two types of PYT/rGO hybrid materials have been developed as cathode materials for aqueous ASC. The optimized electrode can reach a maximum capacity of 711 A g^{-1} at a current density of 1 A g^{-1}. The π-π interaction between the PYT molecules and rGO enhances the stability and rate performance of the composite electrode. With thermally treated $Ti_3C_2T_x$ as the anode, the assembled PYT/GN 4-5//A-$Ti_3C_2T_x$ ASC achieves an energy density of 18.4 Wh kg^{-1} at a power density of 700 W kg^{-1}, with capacity retention of 91.4% after 5,000 cycles at a current density of 3 A g^{-1}.

In paper II, three types of conductive polymers with different conformational flexibility were designed and synthesized via condensation reactions using PYT. UV-Vis spectrophotometric titration reveals variations in the assembly behaviors of polymers and graphene, influenced by the polymer conformational flexibility, and demonstrates how these differences impact the electrochemical performance of the hybrid electrode. The composite electrode exhibits a high specific capacity maximum to 603 F g^{-1} at a current density of 1 A g^{-1}. Moreover, the assembled ASC exhibits a wide potential operating window up to 1.9 V, with an energy density of 38.1 Wh kg^{-1} at a power density of 950 W kg^{-1}. Additionally, the ASC can deliver maximum 95.1% retention after 15,000 cycles.

In the part III, PAH D-A systems have been designed and synthesized, based on the functionalization of PYT. The symmetry of acceptors can be controlled via stoichiometric condensation reactions. UV-Vis spectrophotometric titration illustrates the potential interaction between the D-A systems and graphene. NLO properties will be further investigated at a later stage.

6. Acknowledgments

The completion of this dissertation represents not only the culmination of years of research, but also the support, guidance, and encouragement of many extraordinary individuals. This milestone is as much a testament to their contributions as it is to my perseverance, and I take this opportunity to express my heartfelt gratitude to all those who have been part of this journey.

First and foremost, I owe an immense debt of gratitude to my advisor, Xiaoyan Zhang, whose unwavering guidance, profound knowledge, and steadfast support have been the cornerstone of my academic journey. His ability to challenge my thinking while encouraging my independence has been pivotal in shaping me as a researcher. Your unwavering belief in me, has been a source of inspiration and motivation.

To the professors on the 9th floor—Jerker, Gunnar, Nina, Lars, Angela, and Ann-Sofie—thank you for fostering a supportive and stimulating environment that has greatly contributed to both my academic and personal growth. Your leadership and collegiality serve as exemplary models for younger researchers on the floor. Whether through engaging discussions, collaborative problem-solving, or the shared moments of a coffee break during long hours in the lab, your camaraderie has made this journey both enjoyable and deeply rewarding.

This journey would not have been possible without the unconditional love and support of my family. To my parents, thank you for your sacrifices, encouragement, and the values you instilled in me from an early age. You support my every dream from the young age to now, no matter how ridiculous the dream is. Your faith in my abilities has been a guiding light throughout my life.

I am also deeply thankful for the enduring friendships I have cultivated along the way. To my friends Ishan, Mangmang, and Zenghua, your encouragement, humor, and willingness to lend an ear during times of frustration have been invaluable. You have reminded me that no achievement is complete without meaningful connections and shared experiences. Floor 9 has been the home to me through out all the four and half years. It is hard to include every member here, but I am grateful to all of you for your encouragement, generous help and the nice working environment.

Additionally, I would like to acknowledge my master advisors Professor Junbiao Chang and Xiao-Na Wang. You played a pivotal role in fostering my critical thinking and experimental skills early in my career, providing a solid foundation for my doctoral research.

Acknowledgments

This dissertation is the result of collective efforts, and I am deeply grateful to everyone who contributed to making this achievement possible. To all of you, thank you for your faith in me and for helping me reach this important milestone.

7. Experimental section

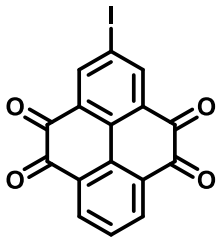

2-iodopyrene-4,5,9,10-tetraone (2)

15 mL of concentrated sulfuric acid (98%) was added to a 50 mL round bottom flask. Then, 262 mg (1.0 mmol) of pyrenetetrone and 270 mg of *N*-iodosuccinimide (1.5 mmol) were added to the reaction. The reaction mixture was stirred at room temperature for 1 h, after which the temperature was raised to 50 °C in an oil bath and allowed to react for an additional 2 hours. Subsequently, the mixture was poured into 40 mL of ice water and neutralized with sodium bicarbonate. The crude product was then dried under vacuum and purified using column chromatography, resulting in the isolation of 221 mg of the target molecule with a yield of 57% (eluent: pure DCM-5% EA in DCM). ^{1}H NMR (400 MHz, $CDCl_3$): δ 8.79 (s, 2H), 8.52 (d, 2H, J = 7.8 Hz), 7.75 (t, 1H, J = 7.8 Hz).

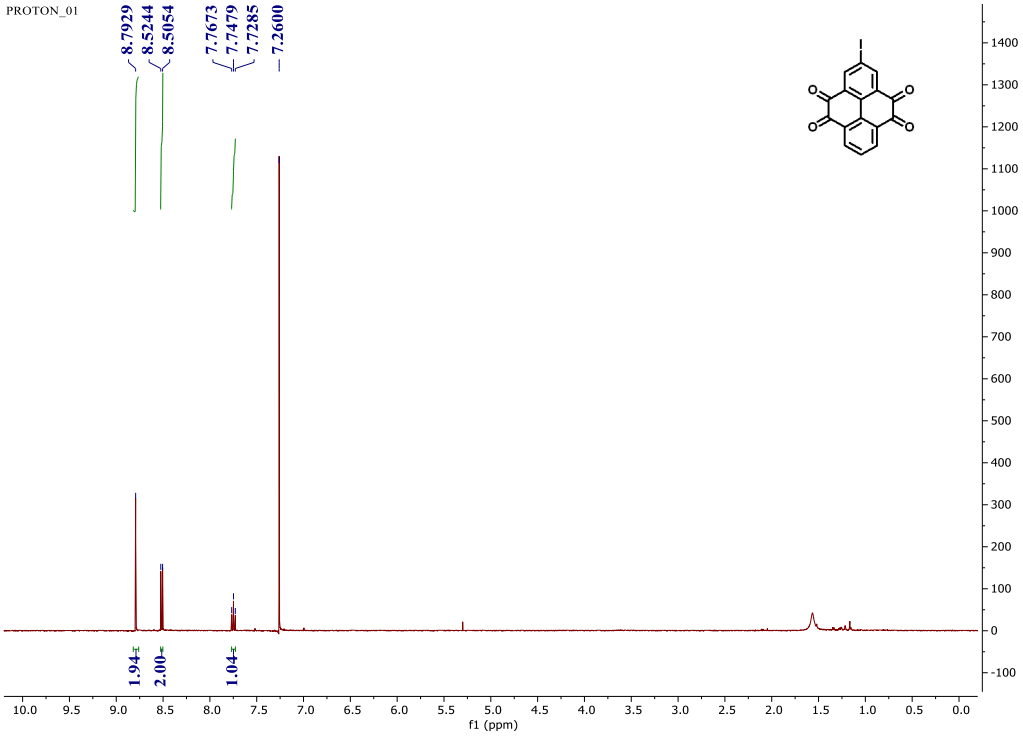

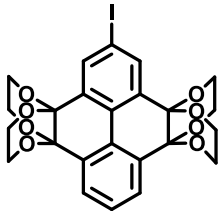

2-iodo-5,6,12,13-tetrahydro-3b,7a:10b,14a-bis(epoxyethanooxy)pyreno[4,5-b:9,10-b']bis([1,4]dioxine) (3)

To a 25 mL round bottom flask, 68.2 mg (0.2 mmol) of 2-iodopyrene-4,5,9,10-tetraone**,** 6.8 ml of toluene, 2.8 mL (0.05 mmol) of ethylene glycol and 34.2 mg (0.18 mmol) of *p*-toluenesulfonic acid were added. The resulting reaction mixture was refluxed at 125 ºC in a oil bath for 20 hours. The reaction was cooled down to room temperature. Subsequently, toluene was removed by a rotary evaporator. The crude was filtered and washed with water and methanol until the solid was white (99.3 mg, 88%). ^{1}H NMR (400 MHz, $CDCl_3$): δ 8.09 (s, 2H), 7.75 (d, 2H, J = 7.7 Hz), 7.52 (t, 1H, J = 7.7 Hz), 4.20 (br, 8H), 3.67 (br, 8H).

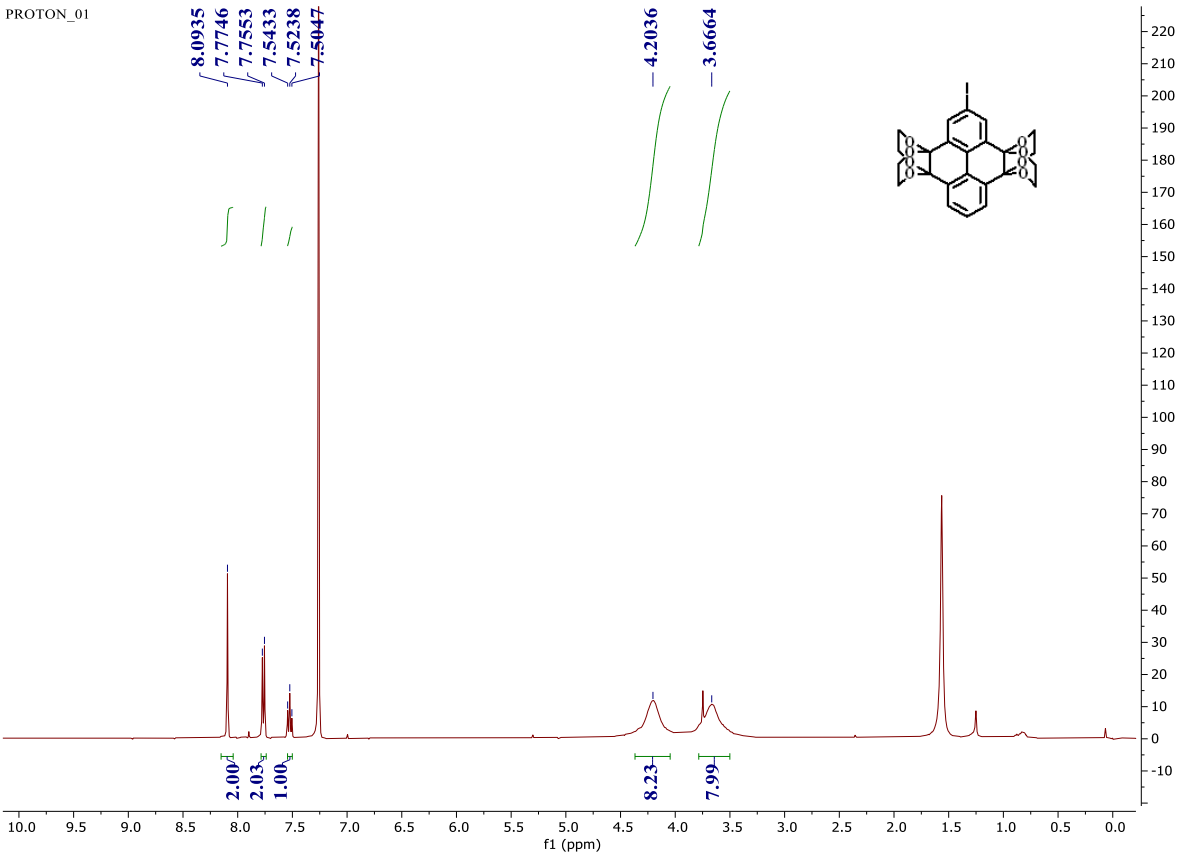

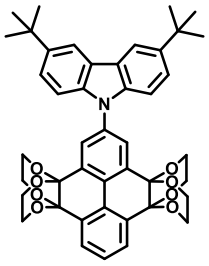

3,6-di-tert-butyl-9-(5,6,12,13-tetrahydro-3b,7a:10b,14a-bis(epoxyethanooxy)pyreno[4,5-b:9,10-b']bis([1,4]dioxine)-2-yl)-9H-carbazole (4)

To a 50 mL three-necked round bottom flask, 35 mg (0.067 mmol) of 2-bromo-4,5,9,10-di(ethylene glycol)ketal-pyrene, 1.4 mg (0.0134 mmol) of $Pd_2(dba)_3 \cdot CH_3Cl$, 5.4 mg (0.0268 mmol) of $(t\text{-}Bu)_3P$, 22.6 mg (0.201 mmol) of KO*t*Bu, and 21 mg (0.075 mmol) of 3,6-di-tert-butylcarbazole were added. Then, the three-necked round bottom flask and the condenser were purged with nitrogen. Subsequently, the reaction mixture was stirred at 115 °C for 18 hours. The solvent was removed under reduced pressure. 42.2 mg of the product was obtained by flash chromatography with a yield of 88%. ^{1}H NMR (400 MHz, $CDCl_3$): δ 8.14 (m, 2H), 8.00 (s, 2H), 7.82 (d, 2H, J = 7.8 Hz), 7.54 (t, 1H, J = 7.8 Hz), 7.50 (dd, J = 8.6, 1.9 Hz, 2H), 7.47 (d, J = 8.6 Hz, 2H), 4.21 (br, 8H), 3.72 (br, 8H), 1.47 (s, 18H). ^{13}C NMR (151 MHz, $CDCl_3$) δ 143.37, 139.25, 138.88, 135.12, 133.01, 129.66, 128.92, 127.61, 127.27, 124.93, 123.94, 123.78, 116.41, 109.63, 92.76, 92.60, 34.91, 32.15.

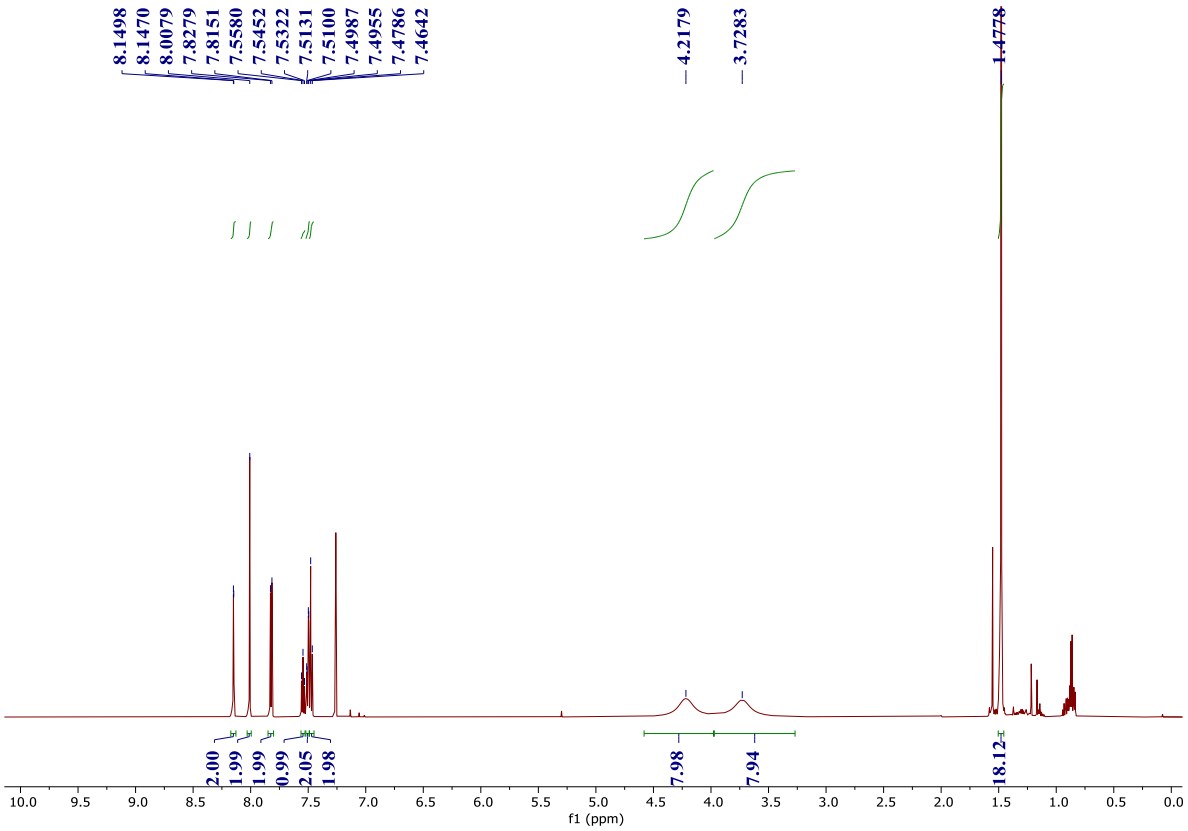
8.1498
8.1470
8.0079
7.8279
7.8151
7.5580
7.5452
7.5322
7.5131
7.5100
7.4987
7.4955
7.4786
7.4642
4.2179
3.7283
1.4778
2.00
1.99
1.99
0.99
2.05
1.98
7.98
7.94
18.12
f1 (ppm)

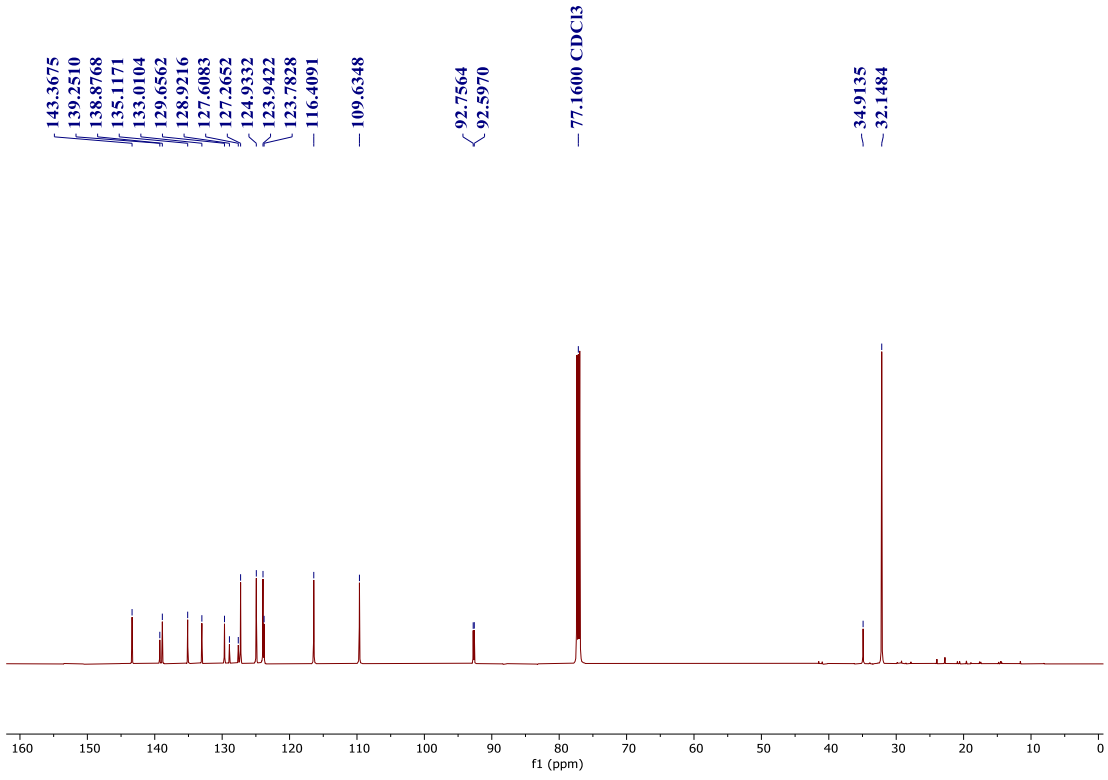
143.3675
139.2510
138.8768
135.1171
133.0104
129.6562
128.9216
127.6083
127.2652
124.9332
123.9422
123.7828
116.4091
109.6348
92.7564
92.5970
77.1600 CDCl3
34.9135
32.1484
f1 (ppm)

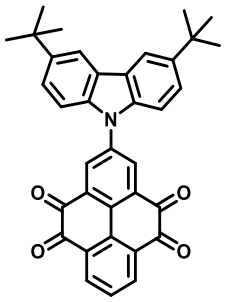

2-(3,6-di-tert-butyl-9H-carbazol-9-yl)pyrene-4,5,9,10-tetraone (5)

32 mg (0.045 mmol) of **4** was added into a 25 mL round bottom flask. Then, a 5 mL of TFA/H_2O = 9/1 solution was slowly added to the flask. The reaction mixture was stirred at room temperature. After 15 hours, the reaction solution was poured into crushed ice. Subsequently, the mixture was extracted with 3 × 10 mL of DCM and dried with sodium sulfate. The solution was evaporated by a rotavapor with a yield of 99%. ^{1}H NMR (400 MHz, $CDCl_3$): δ 8.74 (s, 2H), 8.55 (d, 2H, *J* = 7.8 Hz), 8.15 (d, 2H, *J* = 1.7 Hz), 7.74 (t, 1H, *J* = 7.8 Hz), 7.54 (dd, 2H, *J* = 4.3, 2.0 Hz), 7.44 (d, 2H, *J* = 8.7 Hz), 1.48 (s, 18H). ^{13}C NMR (151 MHz, $CDCl_3$) δ 177.71, 177.60, 145.02, 141.75, 137.83, 137.24, 134.63, 132.89, 132.71, 131.27, 131.06, 130.76, 124.68, 124.59, 116.94, 109.23, 35.00, 32.04.

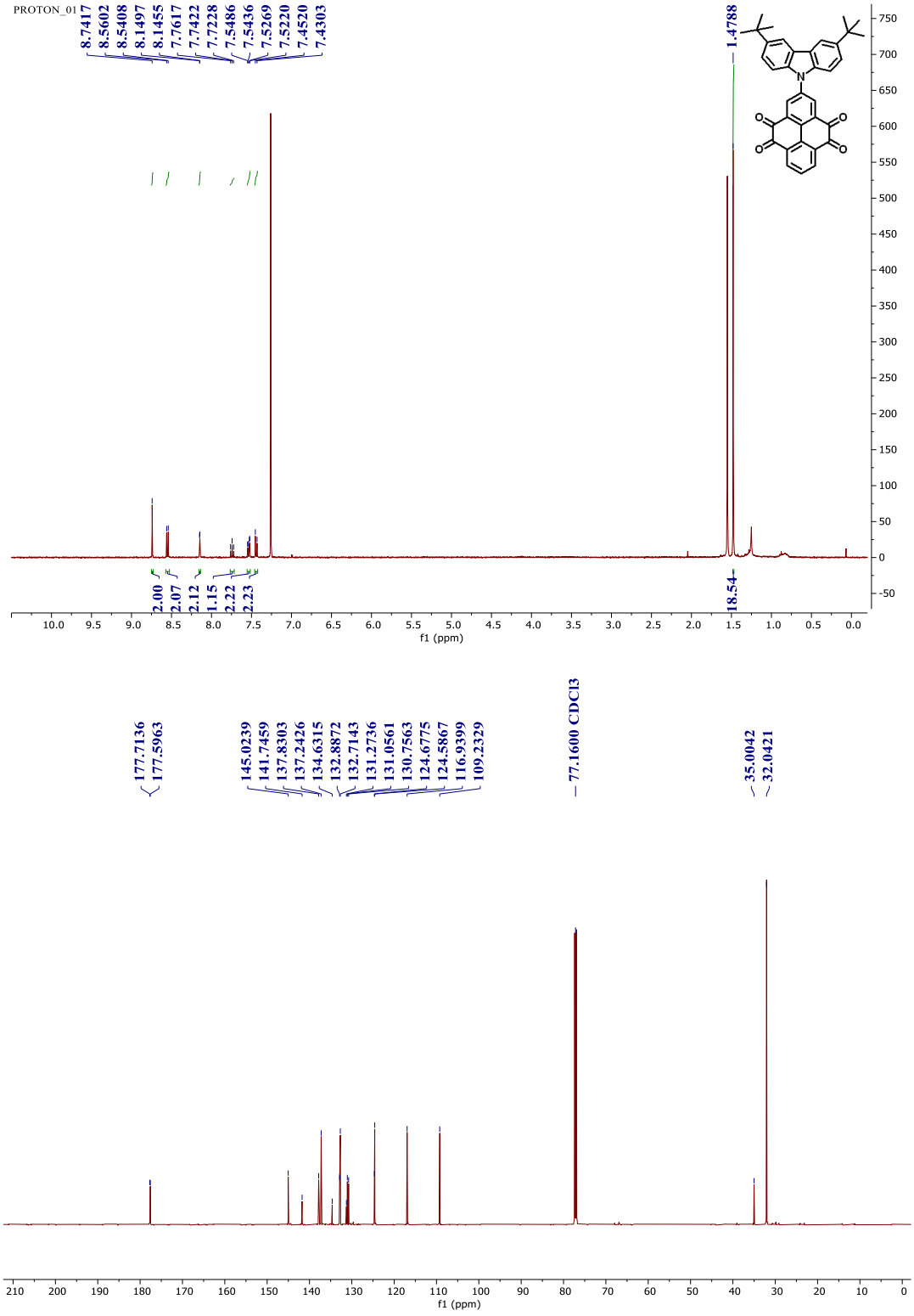
PROTON_01
8.7417
8.5602
8.5408
8.1497
8.1455
7.7617
7.7422
7.7228
7.5486
7.5436
7.5269
7.5220
7.4520
7.4303
1.4788
2.00
2.07
2.12
1.15
2.22
2.23
18.54
f1 (ppm)
177.7136
177.5963
145.0239
141.7459
137.8303
137.2426
134.6315
132.8872
132.7143
131.2736
131.0561
130.7563
124.6775
124.5867
116.9399
109.2329
77.1600 CDCl3
35.0042
32.0421
f1 (ppm)

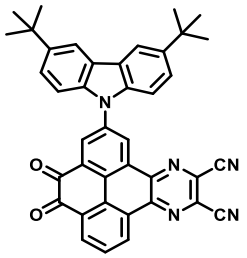

Compound **8**

23 mg (0.043 mmol) of **5** and 4.92 mg (0.0045 mmol) of diaminomaleonitrile were added to a mixture of 5 ml toluene and 5 ml acetic acid in a 50 ml sealed tube, then the flask was evacuated and refilled with N_2 three times, followed by refluxing at 120 °C for 24 h. The reaction was cooled down to room temperature. The solution was dried on a rotavapor. Subsequently, the resulting crude was purified by column chromatography with a yield of 65% (eluent: DCM). ^{1}H NMR (600 MHz, $CDCl_3$) δ 9.68 (d, J = 2.4 Hz, 1H), 9.52 (dd, J = 8.1, 1.4 Hz, 1H), 9.02 (d, J = 2.4 Hz, 1H), 8.82 (dd, J = 7.5, 1.4 Hz, 1H), 8.20 (d, J = 1.9 Hz, 2H), 8.08 (t, J = 7.8 Hz, 1H), 7.56 (dd, J = 8.6, 1.9 Hz, 2H), 7.52 (d, J = 8.7 Hz, 2H), 1.50 (s, 18H). ^{13}C NMR (151 MHz, $CDCl_3$) δ 178.50, 178.36, 145.02, 142.24, 141.51, 141.01, 138.18, 135.45, 134.15, 132.40, 131.94, 131.82, 131.51, 131.40, 130.39, 130.34, 129.78, 129.41, 128.77, 127.57, 124.63, 124.59, 117.02, 113.34, 113.30, 108.88, 35.05, 32.08.

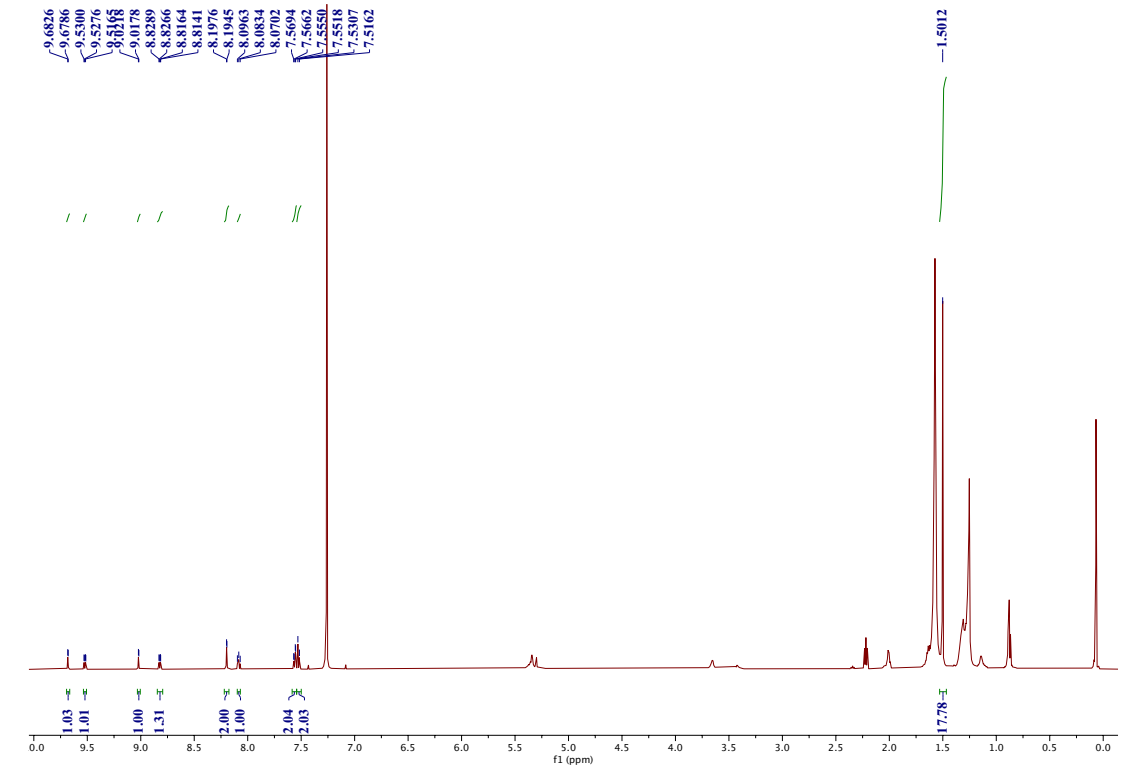
9.6826
9.6786
9.5300
9.5276
9.0218
9.0178
8.8289
8.8266
8.8164
8.8141
8.1976
8.1945
8.0963
8.0834
8.0702
7.5694
7.5662
7.5550
7.5518
7.5307
7.5162
1.5012
1.03
1.01
1.00
1.31
2.00
1.00
2.04
2.03
17.78
f1 (ppm)

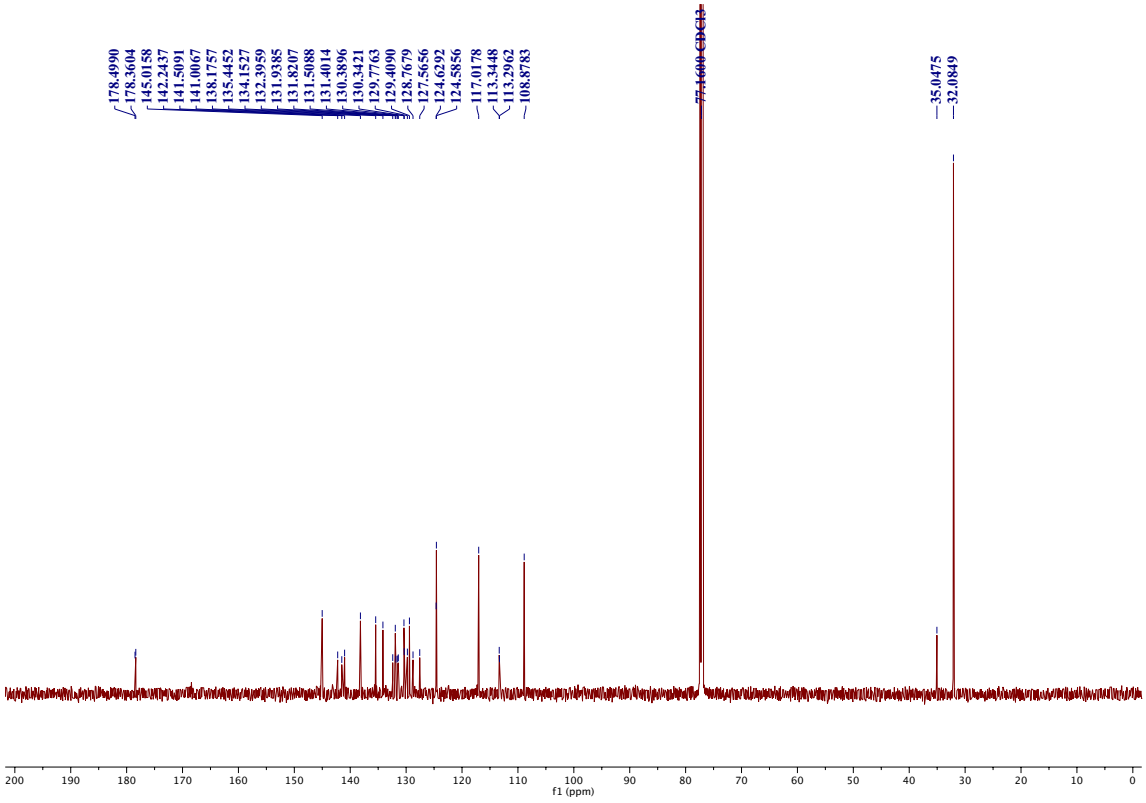
178.4990
178.3604
145.0158
142.2437
141.5091
141.0067
138.1757
135.4452
134.1527
132.3959
131.9385
131.8207
131.5088
131.4014
130.3896
130.3421
129.7763
129.4090
128.7679
127.5656
124.6292
124.5856
117.0178
113.3448
113.2962
108.8783
77.1600 CDCl3
35.0475
32.0849
f1 (ppm)

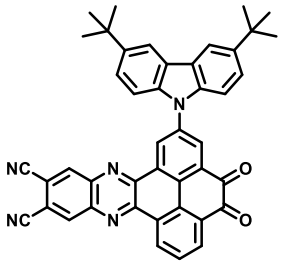

Compound **9**

216 mg (0.400 mmol) of **5**, 68 mg (0.430 mmol) of 4,5-dicyano-1,2-diaminobenzene were added into a 40 ml 10:1 EA/acetic acid mixture. The reaction mixture was stirred at room temperature for 2 days, after which the crude was dried in vacuum and was further isolated on a column with PE/EA 4/1 as the eluent. ^{1}H NMR (600 MHz, $CDCl_3$): 9.87 (d, *J* = 2.4 Hz, 1H), 9.68 (d, *J* = 8.0 Hz, 1H), 8.93 (d, *J* = 2.4 Hz, 1H), 8.9 (s, 1H), 8.87 (s. 1H), 8.75 (dd, *J* = 7.5, 1.4 Hz, 1H), 8.21 (s, 2H), 8.04 (t, *J* = 7.8 Hz, 1H), 7.55 (s, 4H), 1.51 (s, 18H). 13C NMR (151 MHz, CDCl3) δ 178.89, 178.74, 144.75, 144.20, 142.56, 142.33, 140.66, 138.38, 137.82, 137.69, 134.80, 134.35, 132.52, 131.55, 131.25, 130.53, 130.16, 129.35, 129.00, 124.54, 124.46, 116.99, 114.99, 114.93, 114.75, 109.06, 35.04, 32.11.

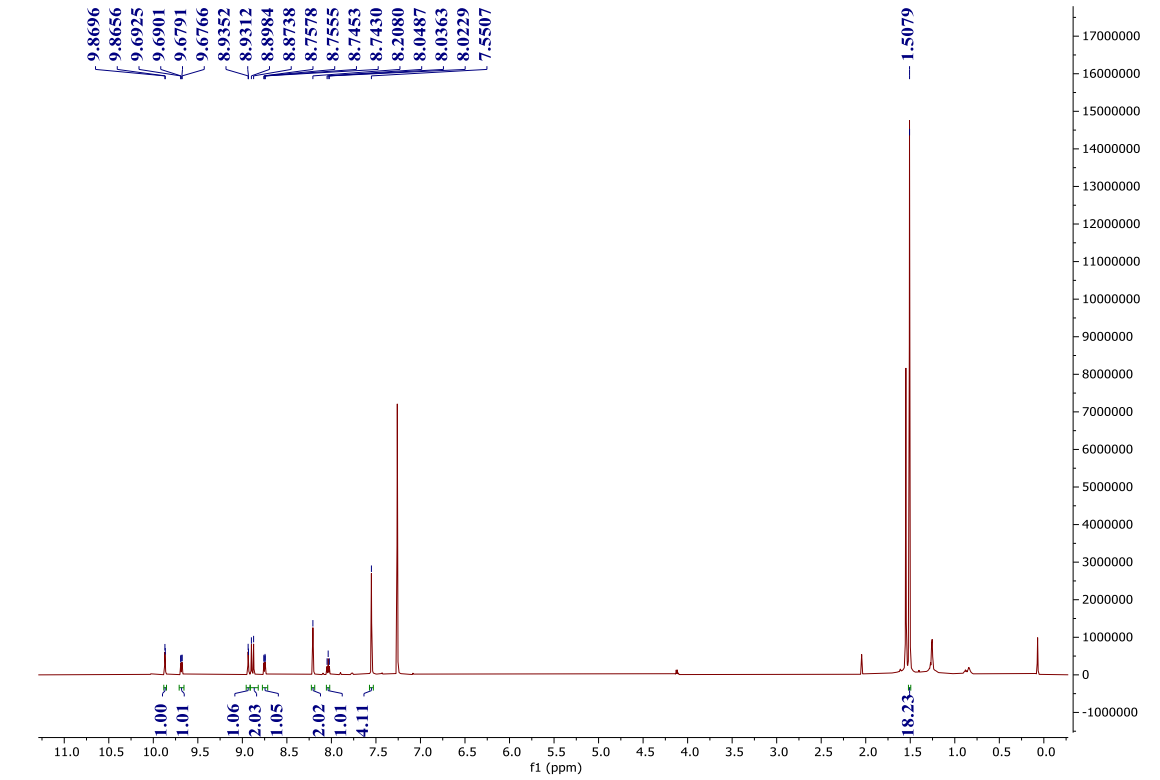
9.8696
9.8656
9.6925
9.6901
9.6791
9.6766
8.9352
8.9312
8.8984
8.8738
8.7578
8.7555
8.7453
8.7430
8.2080
8.0487
8.0363
8.0229
7.5507
1.5079
1.00
1.01
1.06
2.03
1.05
2.02
1.01
4.11
18.23
f1 (ppm)

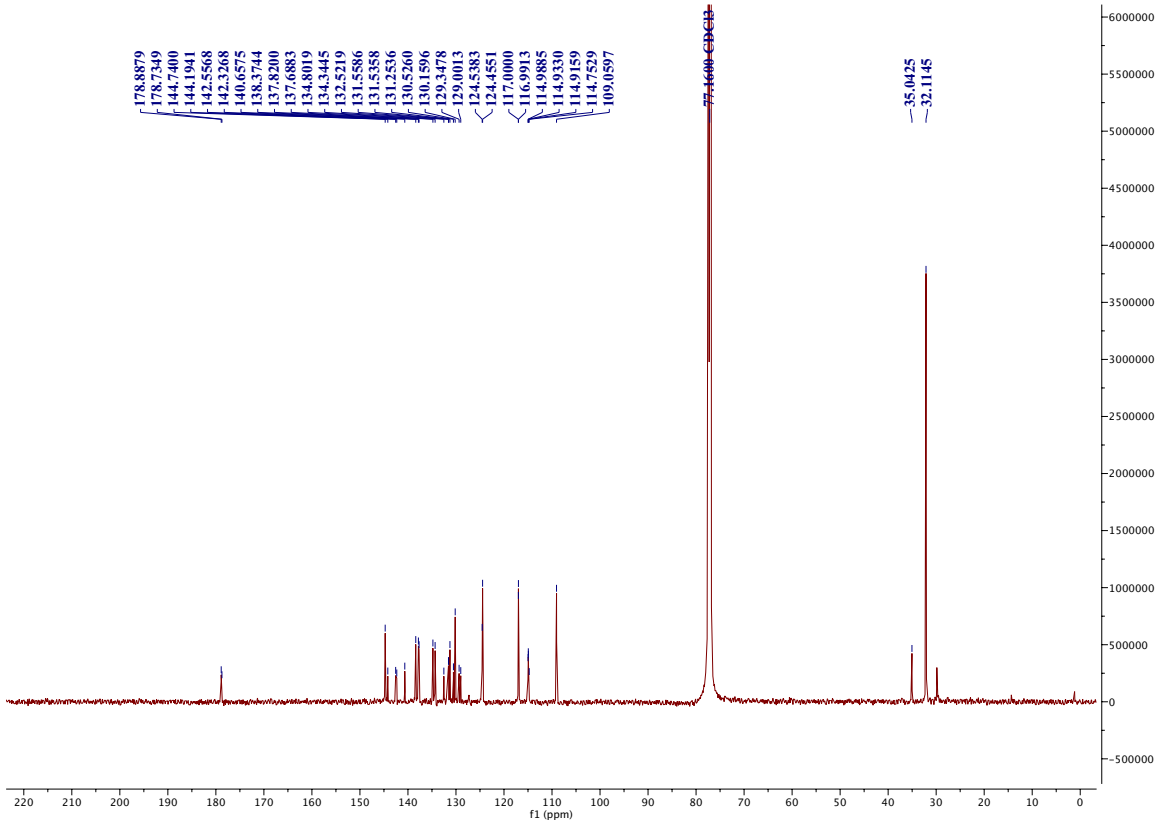
178.8879
178.7349
144.7400
144.1941
142.5568
142.3268
140.6575
138.3744
137.8200
137.6883
134.8019
134.3445
132.5219
131.5586
131.5358
131.2536
130.5260
130.1596
129.3478
129.0013
124.5383
124.4551
117.0000
116.9913
114.9885
114.9330
114.9159
114.7529
109.0597
77.1600 CDCl3
35.0425
32.1145
f1 (ppm)

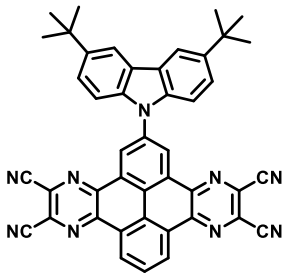

Compound **6**

23 mg (0.043 mmol) of **5** and 10 mg (0.093 mmol) of diaminomaleonitrile were added to a mixture of 5 ml toluene and 5 ml acetic acid in a 50 ml sealed tube, then the flask was evacuated and refilled with N_2 three times, followed by refluxing at 120 °C for 24 h. The reaction was cooled down to room temperature. The solution was dried on a rotavapor, and the resulting crude was purified by column chromatography with a 99% yield (eluent: DCM). ^{1}H NMR (600 MHz, CD_2Cl_2) δ 9.93 (s, 2H), 9.76 (d, J = 7.8 Hz, 2H), 8.47 (t, J = 7.9 Hz, 1H), 8.27 (d, J = 1.9 Hz, 2H), 7.66 (d, J = 8.6 Hz, 2H), 7.59 (dd, J = 8.6, 1.9 Hz, 2H), 1.51 (s, 18H). ^{13}C NMR (151 MHz, $CDCl_3$) δ 144.96, 143.26, 142.47, 140.46, 138.66, 131.94, 131.49, 131.34, 129.81, 129.23, 128.98, 127.64, 127.00, 126.80, 124.64, 124.58, 117.10, 113.47, 113.42, 108.55, 35.08, 32.13.

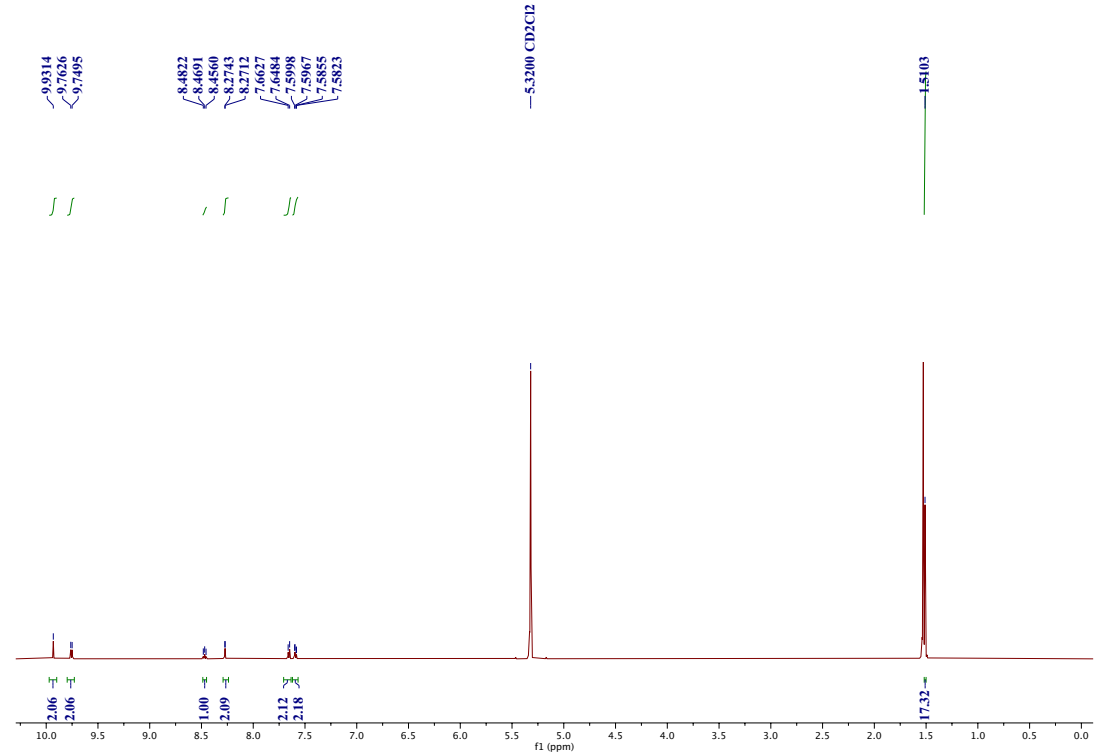
9.9314
9.7626
9.7495
8.4822
8.4691
8.4560
8.2743
8.2712
7.6627
7.6484
7.5998
7.5967
7.5855
7.5823
5.3200 CD2Cl2
1.5103
2.06
2.06
1.00
2.09
2.12
2.18
17.32
f1 (ppm)

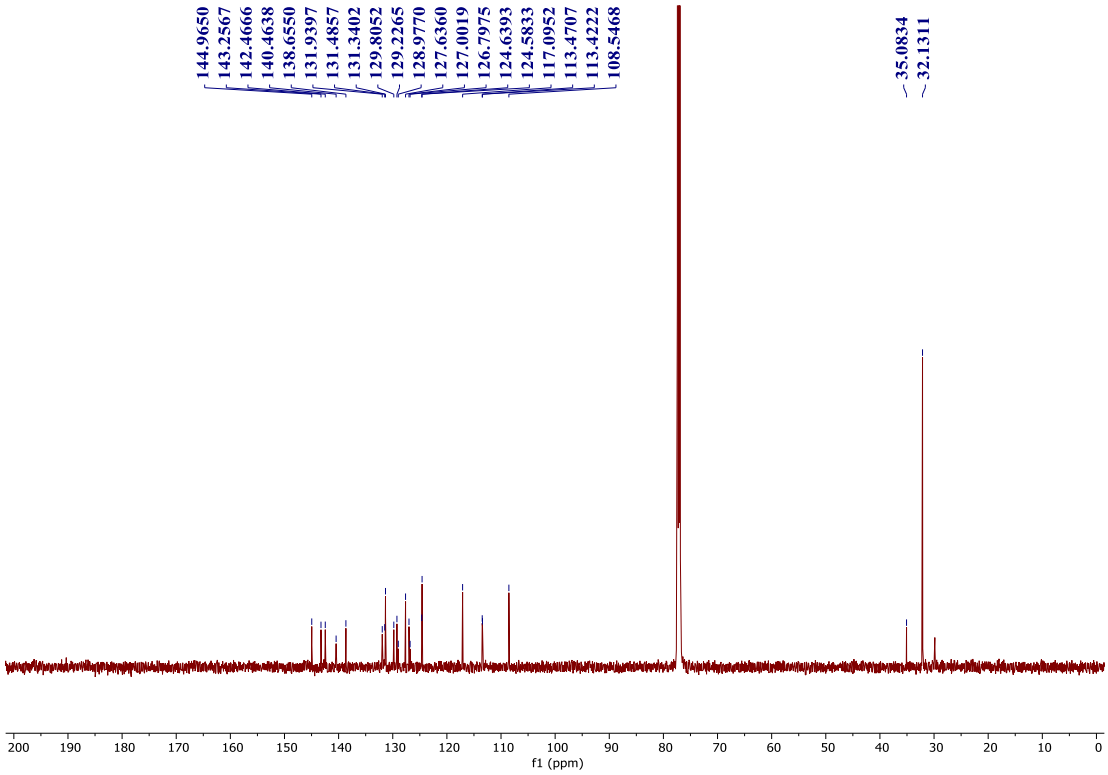
144.9650
143.2567
142.4666
140.4638
138.6550
131.9397
131.4857
131.3402
129.8052
129.2265
128.9770
127.6360
127.0019
126.7975
124.6393
124.5833
117.0952
113.4707
113.4222
108.5468
35.0834
32.1311
f1 (ppm)

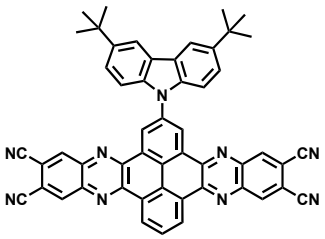

Compound **7e**

50 mg (0.093 mmol) of **5**, 34 mg (0.215 mmol) of 4,5-dicyano-1,2-diaminobenzene was added into a 10 ml 1:1 toluene/acetic acid mixture. The reaction mixture was stirred at room temperature for 2 days, after which the crude was dried in vacuum and isolated on a column using dichloromethane as the eluent, with a 99% yield. ^{1}H NMR (600 MHz, CD_2Cl_2) δ 10.06 (s, 2H), 9.86 (d, J = 7.8 Hz, 2H), 8.94 (s, 2H), 8.88 (s, 2H), 8.36 (t, J = 7.8 Hz, 1H), 8.31 (d, J = 1.4 Hz, 2H), 7.71 (d, J = 8.6 Hz, 2H), 7.60 (dd, J = 8.7, 2.0 Hz, 2H), 1.53 (s, 18H).

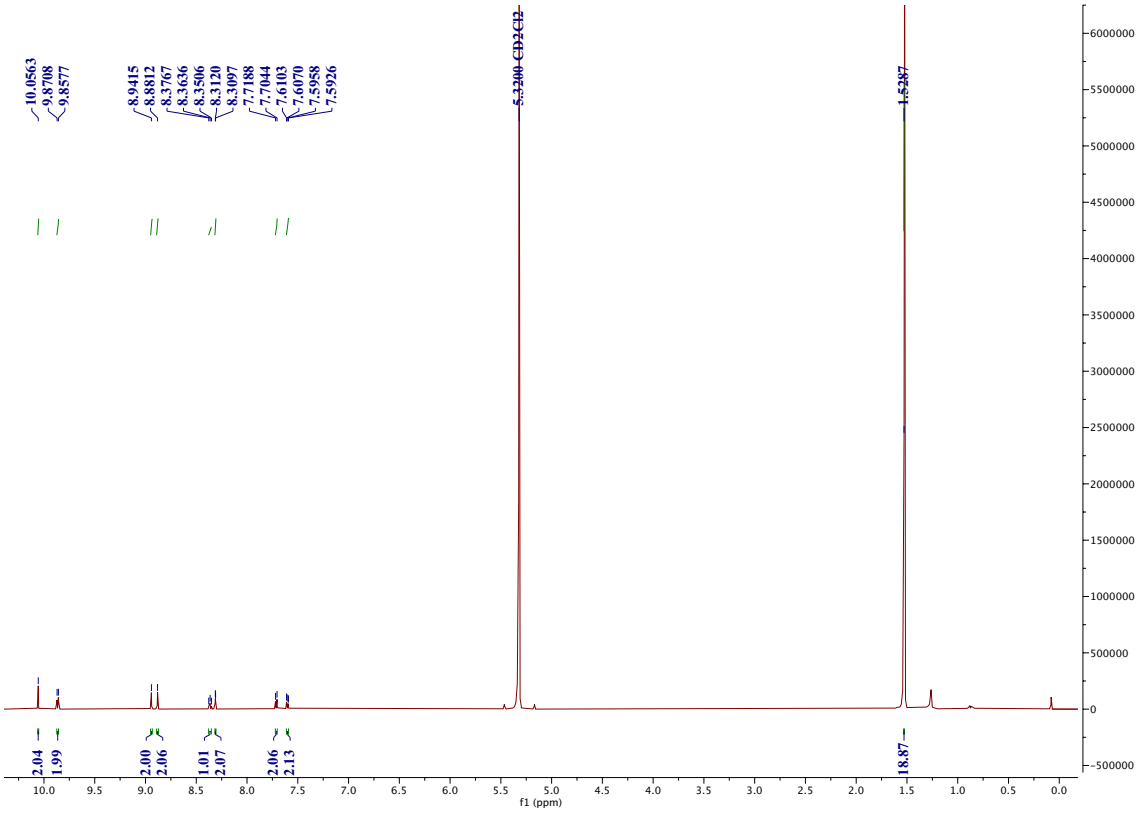

General procedure for compound **10**

20 mg (0.033 mmol) of **8** and 1.2 equivalents of 1,2-phenyldiamine were added to a mixture of 5 ml toluene and 5 ml acetic acid in a 50 ml sealed tube, and then the flask was evacuated and refilled with N_2 three times, followed by refluxing at 120 °C for 24 h. The reaction was cooled down to room temperature. The solution was dried on a rotavapor and the crude was purified by column chromatography.

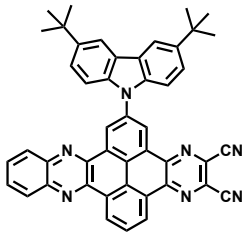

10a

Compound **10a** was obtained with an isolated yield of 99%.

^{1}H NMR (600 MHz, CD_2Cl_2) δ 10.13 (d, *J* = 2.3 Hz, 1H), 9.93 (dd, *J* = 7.8, 1.4 Hz, 1H), 9.74 (d, *J* = 2.3 Hz, 1H), 9.58 (dd, *J* = 7.9, 1.3 Hz, 1H), 8.44 (dd, *J* = 8.2, 0.9 Hz,1H), 8.40 – 8.33 (m, 2H), 8.29 (d, *J* = 1.2 Hz, 2H), 8.00 (td, *J* = 7.4, 1.2 Hz, 1H), 7.96 (td, *J* = 7.4, 1.2 Hz, 1H), 7.69 (d, *J* = 8.5 Hz, 2H), 7.59 (dd, *J* = 8.7, 2.0 Hz, 2H), 1.26 (s, 18H).

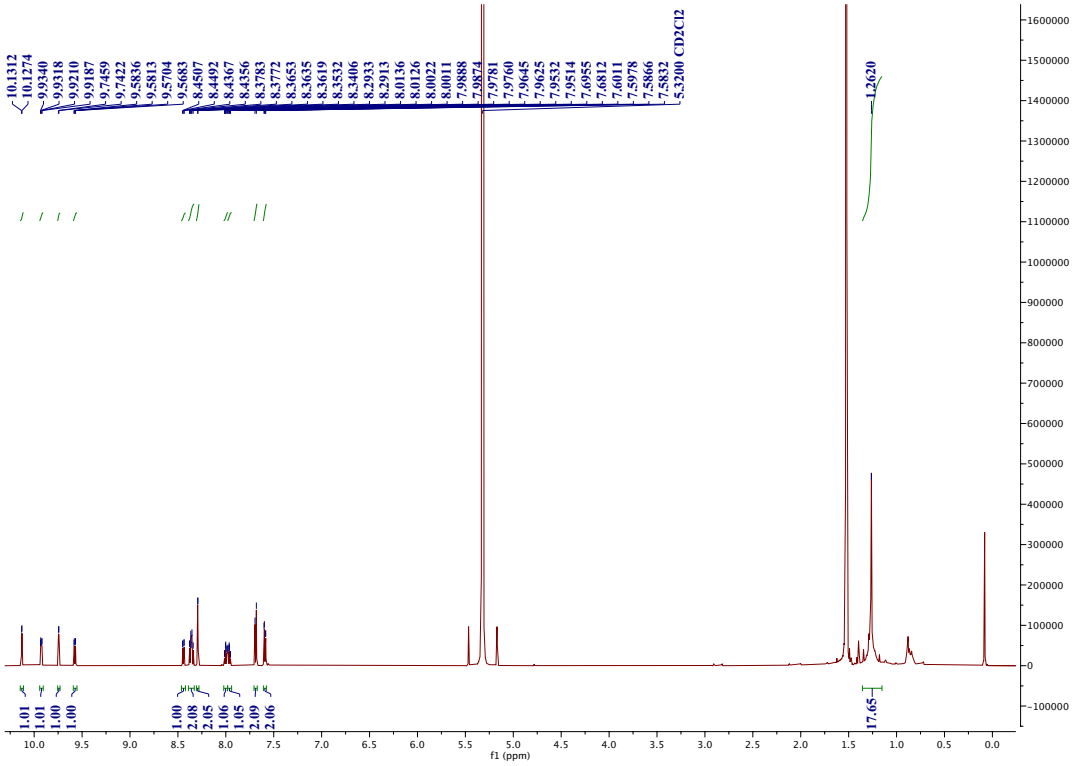
10.1312
10.1274
9.9340
9.9318
9.9210
9.9187
9.7459
9.7422
9.5836
9.5813
9.5704
9.5683
8.4507
8.4492
8.4367
8.4356
8.3783
8.3772
8.3653
8.3635
8.3619
8.3532
8.3406
8.2933
8.2913
8.0136
8.0126
8.0022
8.0011
7.9888
7.9874
7.9781
7.9760
7.9645
7.9625
7.9532
7.9514
7.6955
7.6812
7.6011
7.5978
7.5866
7.5832
5.3200 CD2Cl2
1.2620
1.01
1.01
1.00
1.00
1.00
2.08
2.05
1.06
1.05
2.09
2.06
17.65
f1 (ppm)

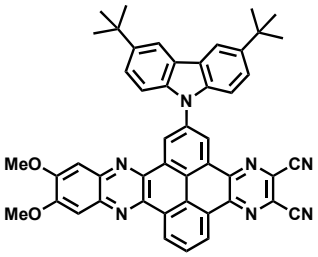

10c

Compound **10c** was obtained with an isolated yield of 99%.

^{1}H NMR (600 MHz, $CDCl_3$/TFA) δ 10.12 (d, *J* = 2.3 Hz, 1H), 9.93 (d, *J* = 2.2 Hz, 1H), 9.83 (dd, *J* = 7.9, 1.1 Hz, 1H), 9.75 (d, *J* = 7.3 Hz, 1H), 8.52 (t, *J* = 8.0 Hz, 1H), 8.28 (d, *J* = 2.0 Hz, 2H), 7.96 (s, 1H), 7.85 (s, 1H), 7.65 (d, *J* = 8.6 Hz, 2H), 7.60 (dd, *J* = 8.6, 1.9 Hz, 2H), 4.29 (s, 3H), 4.25 (s, 3H), 1.53 (s, 18H). ^{13}C NMR (151 MHz, $CDCl_3$) δ 160.54, 157.37, 144.98, 143.16, 142.72, 142.14, 140.63, 139.43, 138.90, 132.13, 131.88, 131.83, 131.61, 131.13, 130.02, 129.53, 129.33, 129.05, 128.63, 127.67, 126.92, 126.80, 125.34, 124.67, 124.53, 122.13, 113.16, 108.71, 106.13, 98.97, 58.11, 57.69, 35.11, 32.10.

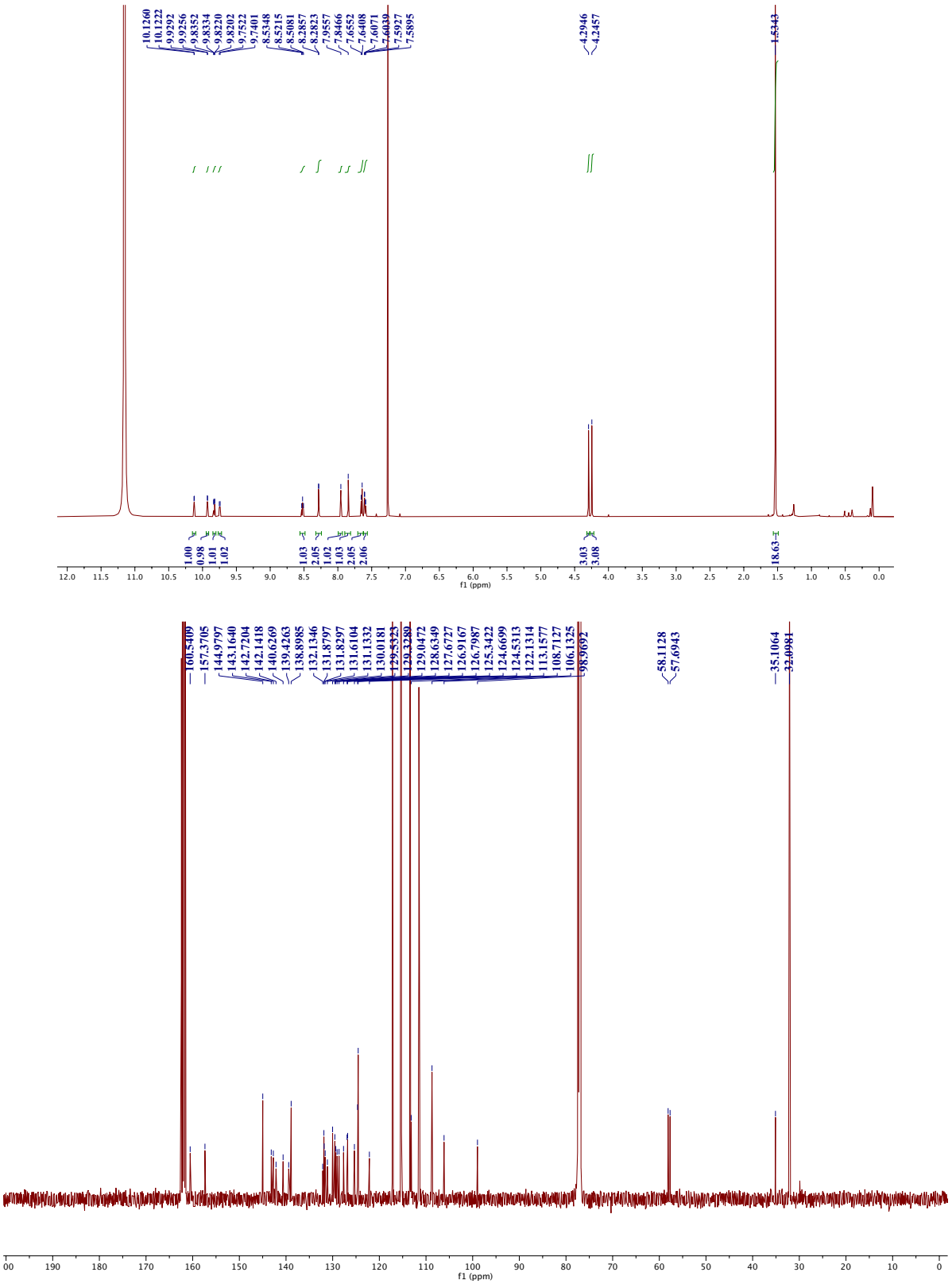
10.1260
10.1222
9.9292
9.9256
9.8352
9.8334
9.8220
9.8202
9.7522
9.7401
8.5348
8.5215
8.5081
8.2857
8.2823
7.9557
7.8466
7.6552
7.6408
7.6071
7.6039
7.5927
7.5895
4.2946
4.2457
1.5343
1.00
0.98
1.01
1.02
1.03
2.05
1.02
1.03
2.05
2.06
3.03
3.08
18.63
f1 (ppm)
160.5409
157.3705
144.9797
143.1640
142.7204
142.1418
140.6269
139.4263
138.8985
132.1346
131.8797
131.8297
131.6104
131.1332
130.0181
129.5323
129.3280
129.0472
128.6349
127.6727
126.9167
126.7987
125.3422
124.6699
124.5313
122.1314
113.1577
108.7127
106.1325
98.9692
58.1128
57.6943
35.1064
32.0981
f1 (ppm)

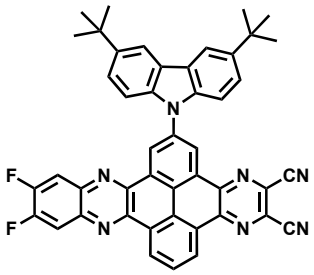

10d

Compound **10d** was obtained with an isolated yield of 99%.

^{1}H NMR (600 MHz, $CDCl_3$) δ 10.08 (d, *J* = 2.2 Hz, 1H), 9.87 (dd, *J* = 7.8, 1.3 Hz, 1H), 9.74 (d, *J* = 2.3 Hz, 1H), 9.58 (dd, *J* = 7.9, 1.3 Hz, 1H), 8.34 (t, *J* = 7.8 Hz, 1H), 8.26 (d, *J* = 1.9 Hz, 2H), 8.16 (dd, *J* = 10.1, 8.0 Hz, 1H), 8.10 (dd, *J* = 10.1, 8.1 Hz, 1H), 7.63 (d, *J* = 8.6 Hz, 2H), 7.57 (dd, *J* = 8.6, 1.9 Hz, 2H), 1.53 (s, 16H).

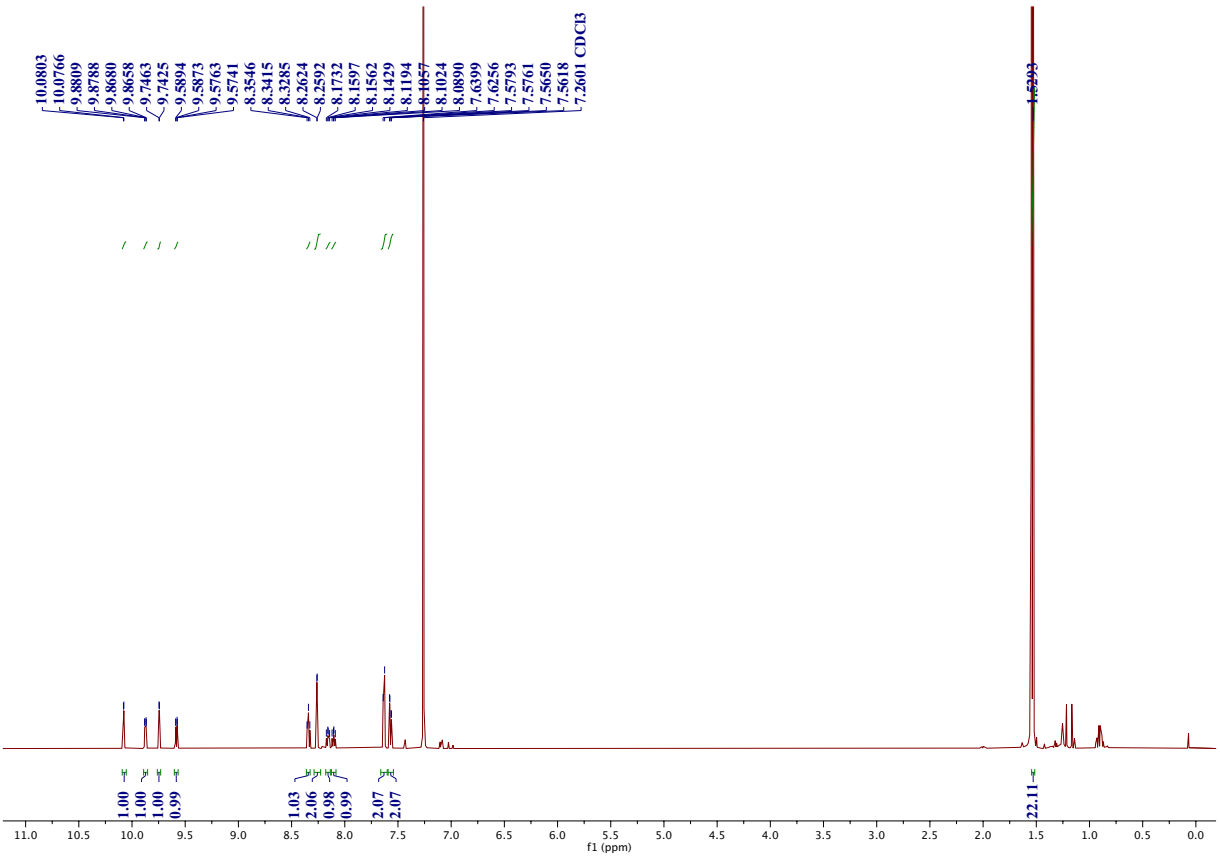

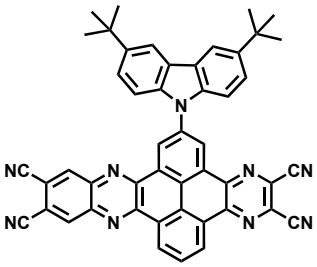

10e

Compound **10e** was obtained with a isolated yield at 99%.

^{1}H NMR (600 MHz, $CDCl_3$) δ 10.11 (d, *J* = 1.8 Hz, 1H), 9.92 (d, *J* = 7.8 Hz, 1H), 9.85 (d, *J* = 1.7 Hz, 1H), 9.70 (d, *J* = 7.9 Hz, 1H), 8.94 (s, 1H), 8.90 (s, 1H), 8.41 (t, *J* = 7.8 Hz, 1H), 8.26 (d, *J* = 1.2 Hz, 2H), 7.63 (d, *J* = 8.6 Hz, 2H), 7.58 (dd, *J* = 8.7, 1.4 Hz, 2H), 1.53 (s, 18H).

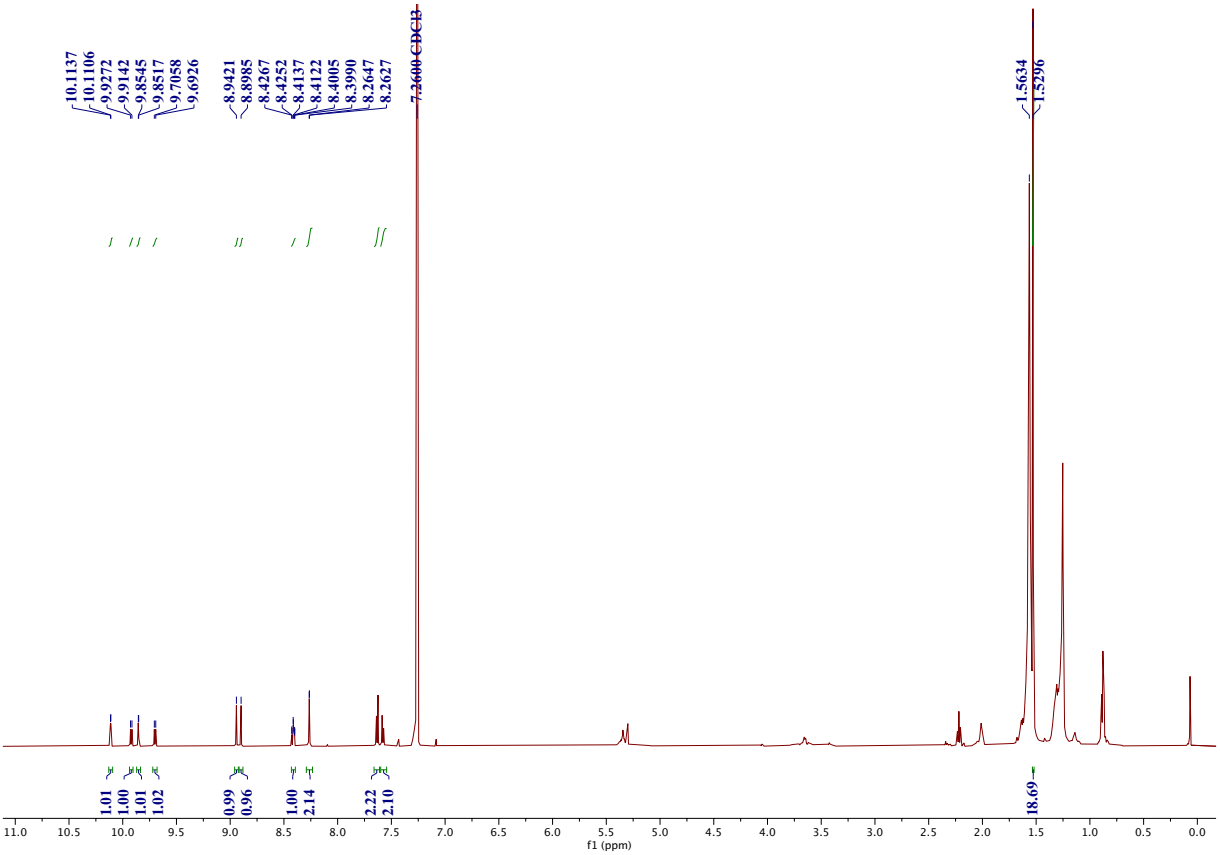

General procedure for compound **11**

20 mg (0.030 mmol) of **9**, 1.5 equivalents of 1,2-phenyldiamine were added into a 2 ml 1:1 toluene/acetic acid mixture. The reaction mixture was stirred at room temperature overnight.

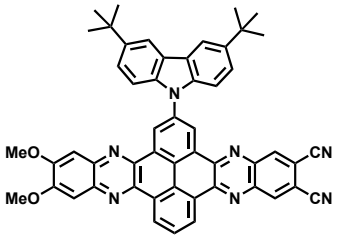

Compound **11a** was purified via column chromatography using 1%-2% methanol in DCM as the eluent, with a yield of 68%. ^{1}H NMR (600 MHz, $CDCl_3$/TFA = 10/1) δ 10.12 (d, J = 2.2 Hz, 1H), 10.06 (d, J = 2.2 Hz, 1H), 9.99 (dd, *J* = 7.7, 0.8 Hz, 1H), 9.66 (dd, *J* = 8.1, 0.8 Hz, 1H), 9.01 (s, 1H), 8.96 (s, 1H), 8.48 (t, *J* = 7.9 Hz, 1H), 8.30 (d, *J* = 1.6 Hz, 2H), 7.96 (s, 1H), 7.86 (s, 1H), 7.69 (d, *J* = 8.6 Hz, 2H), 7.60 (dd, *J* = 8.6, 1.9 Hz, 2H), 4.30 (s, 3H), 4.25 (s, 3H), 1.54 (s, 18H). ^{13}C NMR (151 MHz, $CDCl_3$/TFA = 10/1) δ 160.38, 157.21, 145.68, 145.32, 144.80, 142.88, 142.75, 141.99, 140.33, 139.63, 139.01, 138.29, 132.11, 131.86, 131.18, 131.05, 129.88, 129.41, 129.06, 128.97, 128.76, 127.44, 126.25, 125.39, 124.58, 124.43, 122.07, 117.26, 114.61, 114.56, 114.06, 113.97, 108.90, 106.18, 98.92, 58.07, 57.66, 35.10, 32.11.

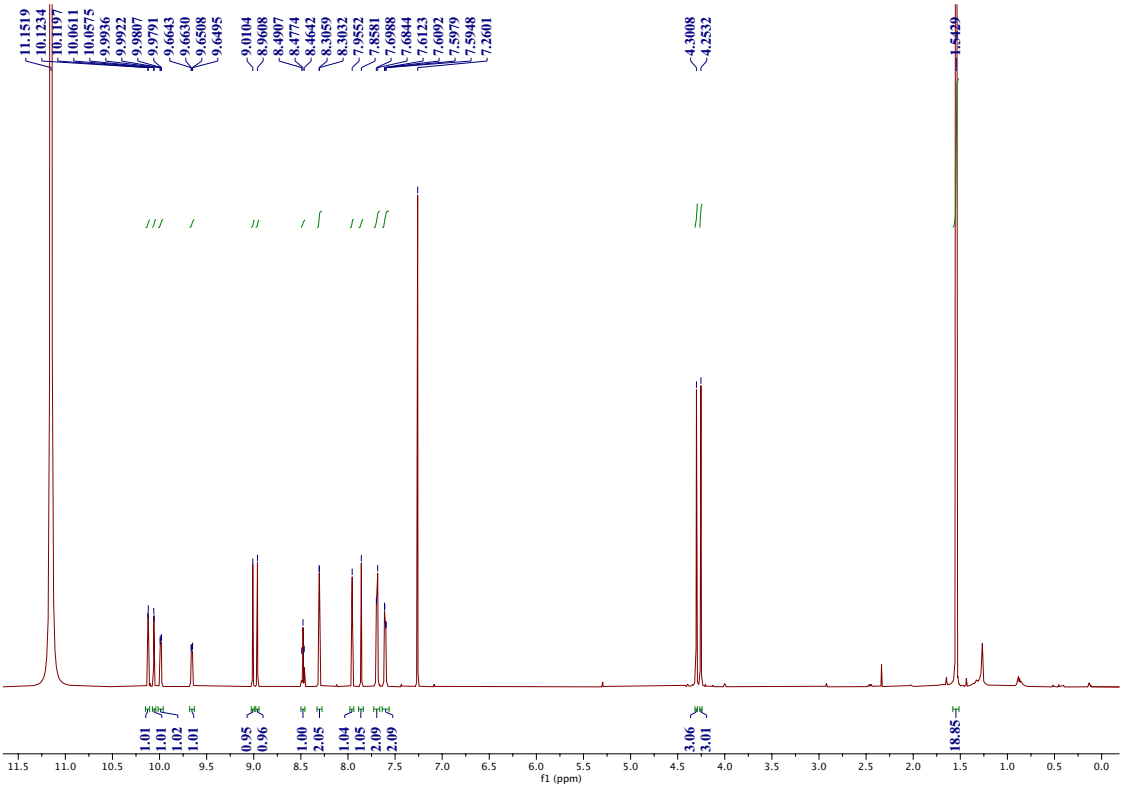
11.1519
10.1234
10.1197
10.0611
10.0575
9.9936
9.9922
9.9807
9.9791
9.6643
9.6630
9.6508
9.6495
9.0104
8.9608
8.4907
8.4774
8.4642
8.3059
8.3032
7.9552
7.8581
7.6988
7.6844
7.6123
7.6092
7.5979
7.5948
7.2601
4.3008
4.2532
1.5439
1.01
1.01
1.01
1.02
1.01
0.95
0.96
1.00
2.05
1.04
1.05
2.09
2.09
3.06
3.01
18.85
f1 (ppm)

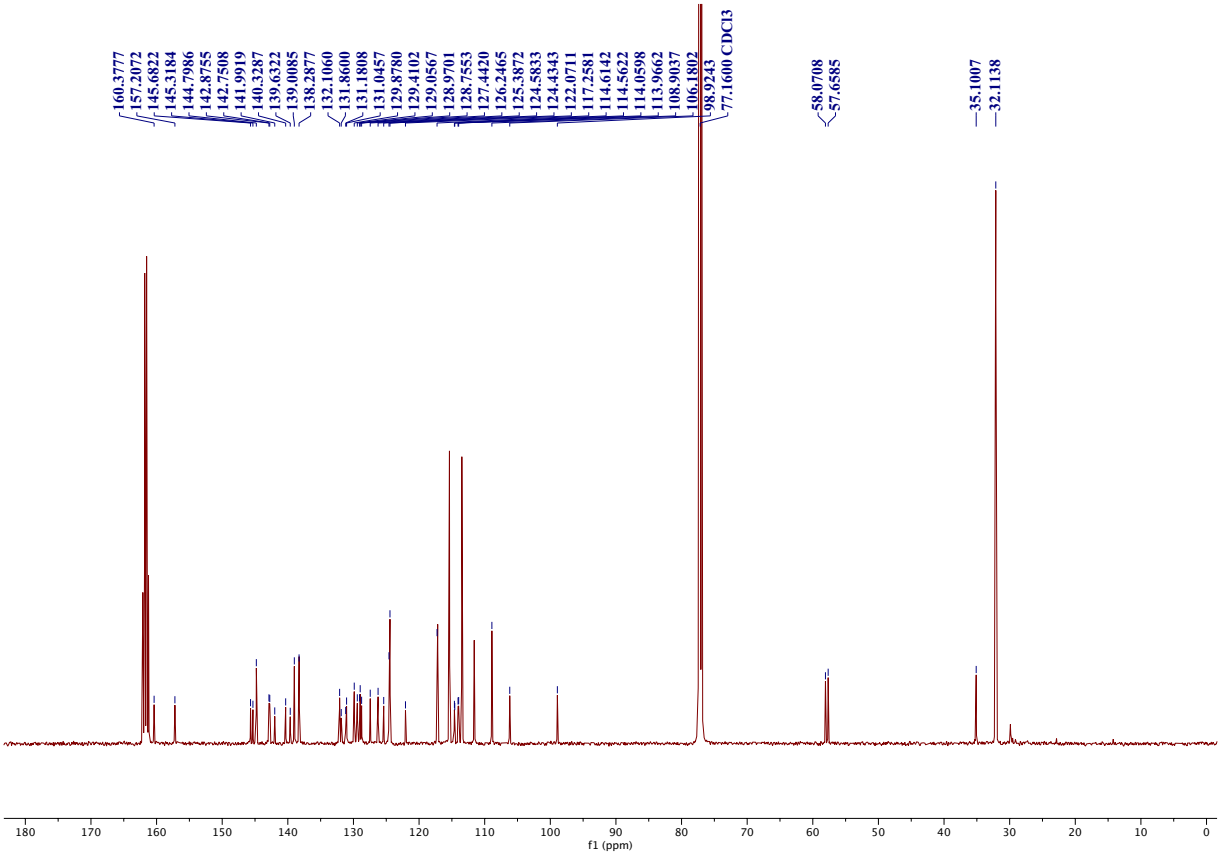
160.3777
157.2072
145.6822
145.3184
144.7986
142.8755
142.7508
141.9919
140.3287
139.6322
139.0085
138.2877
132.1060
131.8600
131.1808
131.0457
129.8780
129.4102
129.0567
128.9701
128.7553
127.4420
126.2465
125.3872
124.5833
124.4343
122.0711
117.2581
114.6142
114.5622
114.0598
113.9662
108.9037
106.1802
98.9243
77.1600 CDCl3
58.0708
57.6585
35.1007
32.1138
f1 (ppm)

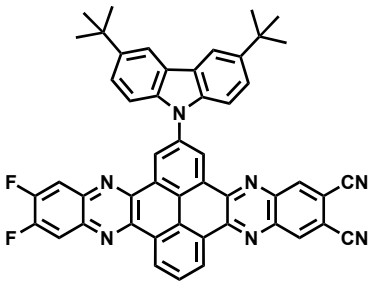

Compound **11b** was purified via column chromatography using chloroform as the eluent, with a yield of 75%. ^{1}H NMR (600 MHz, $CDCl_3$) δ 9.94 (d, *J* = 2.4 Hz, 1H), 9.86 (d, *J* = 2.3 Hz, 1H), 9.71 (dd, *J* = 7.8, 1.3 Hz, 1H), 9.63 (dd, *J* = 7.8, 1.4 Hz, 1H), 8.79 (s, 1H), 8.77 (s, 1H), 8.28 (d, *J* = 1.6 Hz, 2H), 8.22 (t, *J* = 7.8 Hz, 1H), 8.12 – 8.01 (m, 2H), 7.69 (d, *J* = 8.6 Hz, 2H), 7.58 (dd, *J* = 8.6, 2.0 Hz, 2H), 1.25 (s, 18H). ^{13}C NMR (151 MHz, $CDCl_3$) δ 155.82 (dd, *J* = 267.9, 16.4 Hz), 154.75 (dd, *J* = 265.9, 16.4 Hz), 145.72, 145.34, 144.94, 142.96, 142.85, 142.73, 140.44, 140.37, 138.95, 138.44, 138.35, 138.27, 134.22-134.09 (m, 2C), 132.47, 131.01, 130.49, 129.75, 129.70, 129.33, 129.17, 127.86, 127.06, 126.02, 124.66, 124.51, 115.62, 115.50, 114.45, 114.40, 113.81, 113.69, 111.38, 111.25, 108.92, 35.12, 32.09.

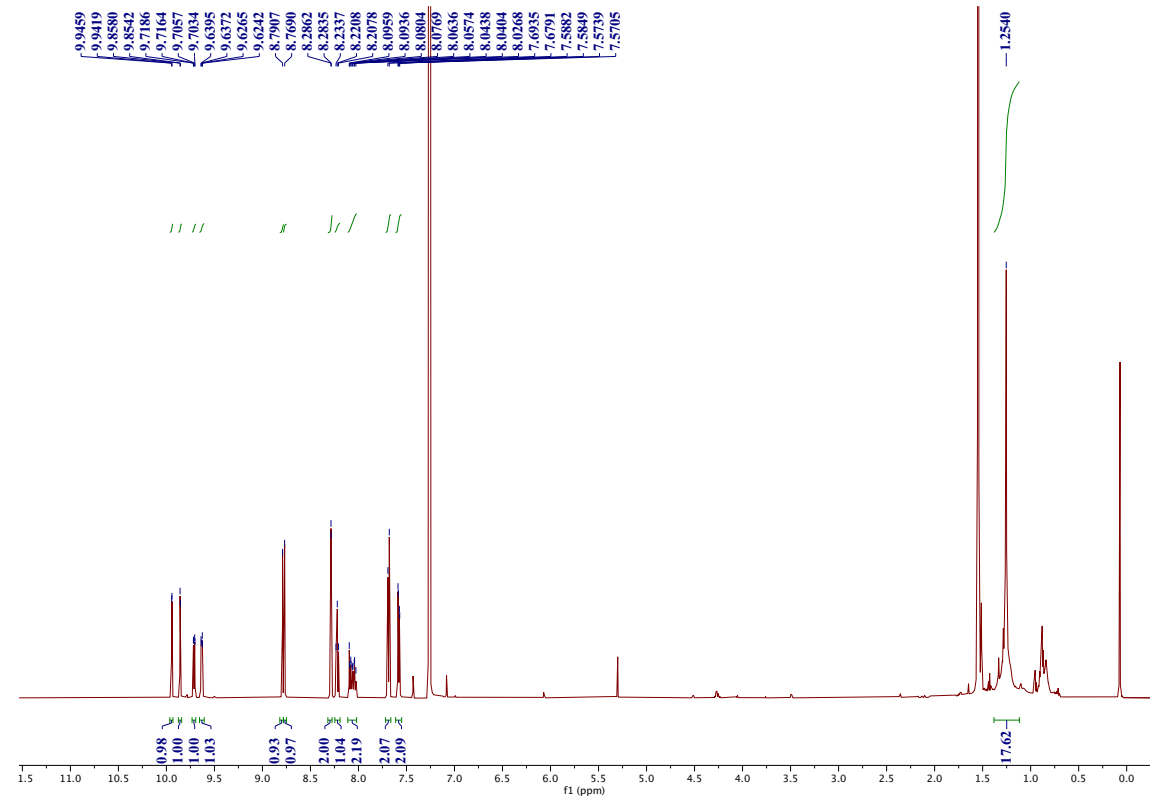
9.9459
9.9419
9.8580
9.8542
9.7186
9.7164
9.7057
9.7034
9.6395
9.6372
9.6265
9.6242
8.7907
8.7690
8.2862
8.2835
8.2337
8.2208
8.2078
8.0959
8.0936
8.0804
8.0769
8.0636
8.0574
8.0438
8.0404
8.0268
7.6935
7.6791
7.5882
7.5849
7.5739
7.5705
1.2540
0.98
1.00
1.00
1.03
0.93
0.97
2.00
1.04
2.19
2.07
2.09
17.62
f1 (ppm)

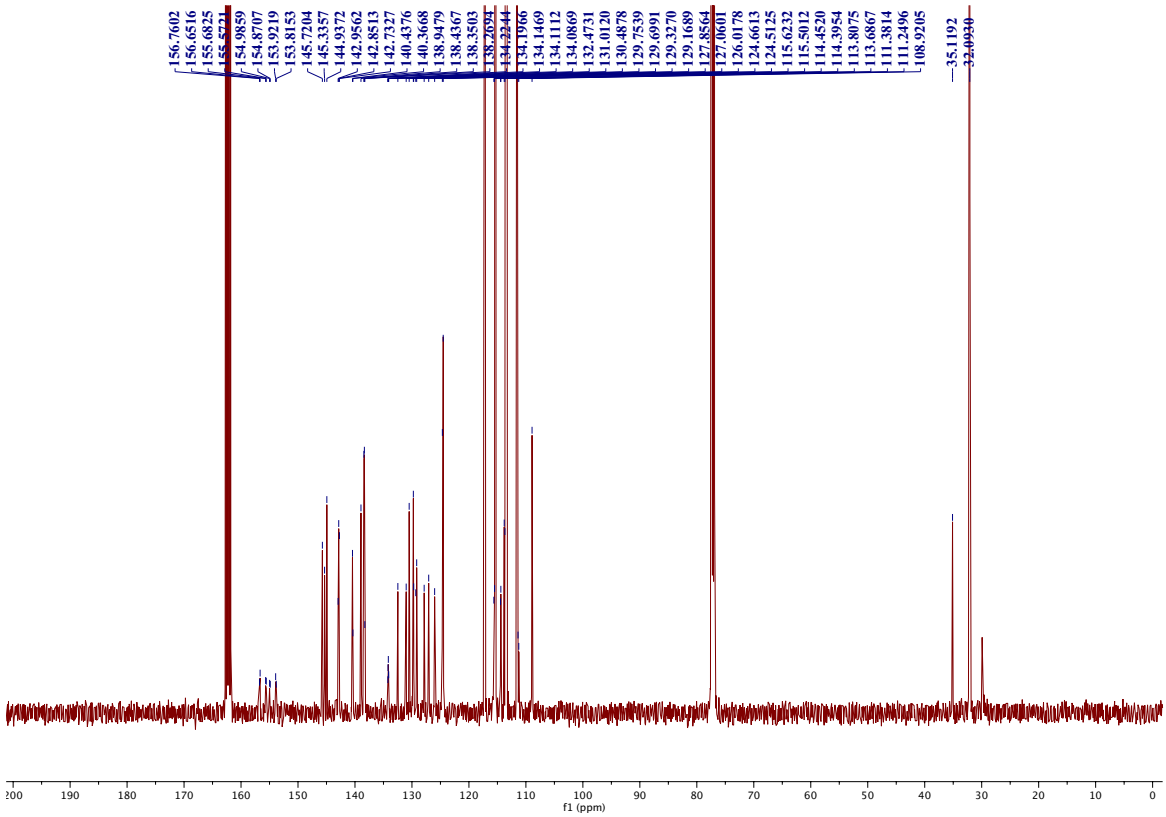
156.7602
156.6516
155.6825
155.5721
154.9859
154.8707
153.9219
153.8153
145.7204
145.3357
144.9372
142.9562
142.8513
142.7327
140.4376
140.3668
138.9479
138.4367
138.3503
138.2693
134.2244
134.1966
134.1469
134.1112
134.0869
132.4731
131.0120
130.4878
129.7539
129.6991
129.3270
129.1689
127.8564
127.0601
126.0178
124.6613
124.5125
115.6232
115.5012
114.4520
114.3954
113.8075
113.6867
111.3814
111.2496
108.9205
35.1192
32.0930
f1 (ppm)

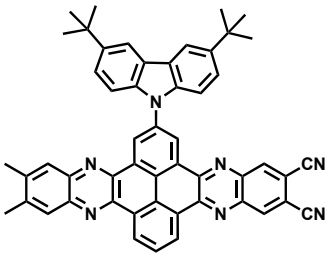

Compound **11c** was purified via recrystallization in a TFA/ethanol mixture, with a yield of 45%. ^{1}H NMR (600 MHz, $CDCl_3$/TFA = 10/1) δ 10.15 (s, 1H), 10.10 (s, 1H), 10.03 (dd, *J* = 7.8, 1.1 Hz, 1H), 9.71 (dd, *J* = 8.0, 1.1 Hz, 1H), 9.02 (s, 1H), 8.98 (s, 1H), 8.53 – 8.40 (m, 3H), 8.30 (s, 2H), 7.69 (d, *J* = 9.3 Hz, 2H), 7.60 (d, *J* = 8.4 Hz, 2H), 2.78 (s, 3H), 2.74 (s, 3H), 1.54 (s, 18H). ^{13}C NMR (151 MHz, $CDCl_3$/TFA = 10/1) δ 151.87, 147.46, 145.50, 145.20, 144.95, 142.92, 142.82, 142.32, 142.11, 140.68, 138.90, 138.38, 133.63, 133.34, 131.21, 130.91, 130.06, 130.02, 129.64, 129.60, 129.01, 128.33, 128.04, 126.79, 125.62, 124.66, 124.51, 121.80, 120.42, 117.17, 114.53, 114.48, 114.11, 114.03, 108.87, 35.10, 32.09, 21.64, 21.07.

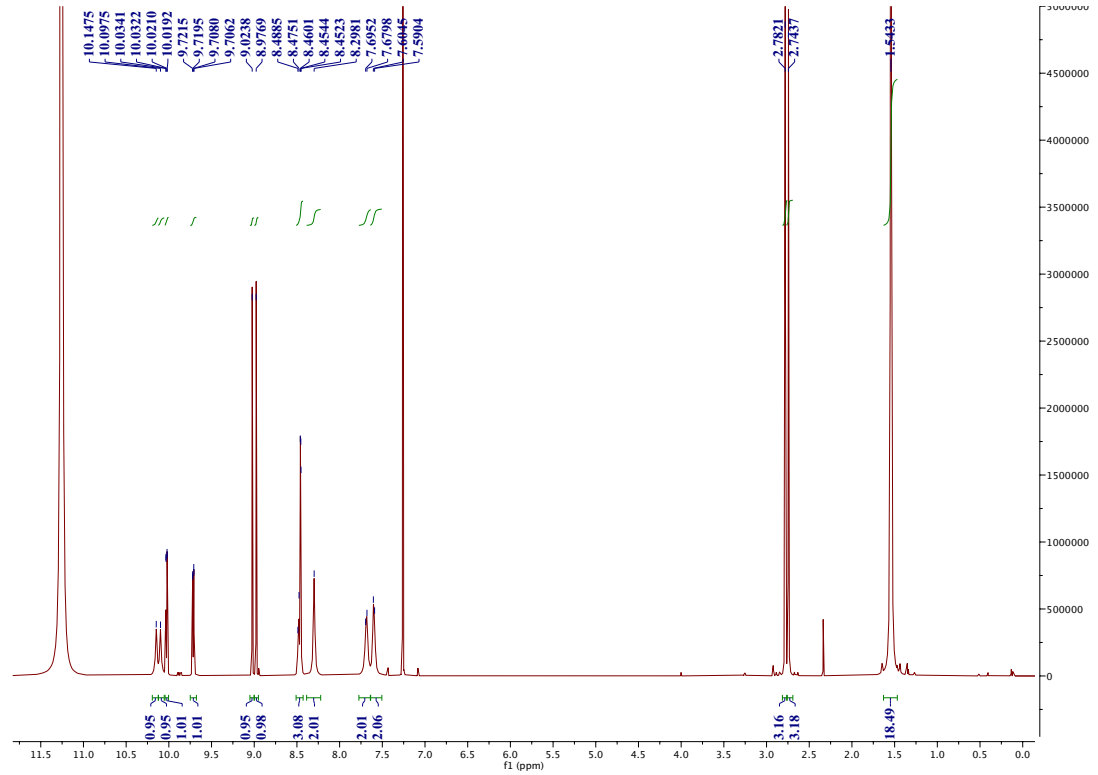
10.1475
10.0975
10.0341
10.0322
10.0210
10.0192
9.7215
9.7195
9.7080
9.7062
9.0238
8.9769
8.4885
8.4751
8.4601
8.4544
8.4523
8.2981
7.6952
7.6798
7.6045
7.5904
2.7821
2.7437
1.5433
0.95
0.95
1.01
1.01
0.95
0.98
3.08
2.01
2.01
2.06
3.16
3.18
18.49
f1 (ppm)

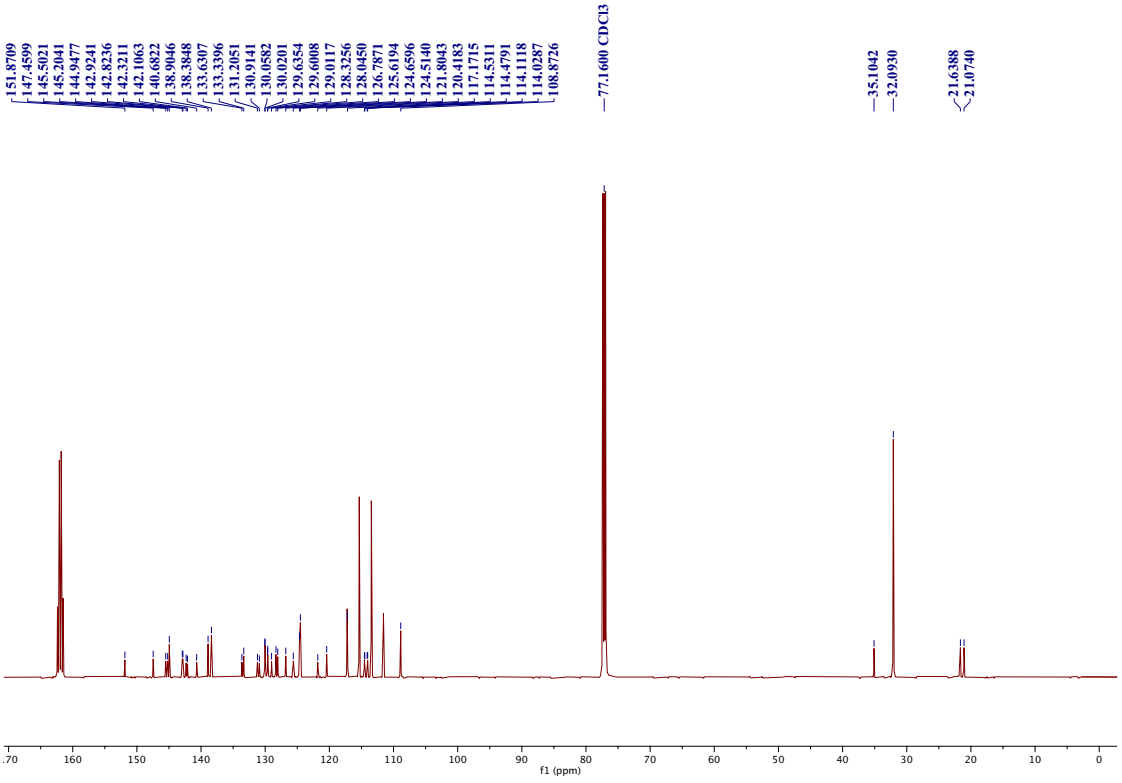
151.8709
147.4599
145.5021
145.2041
144.9477
142.9241
142.8236
142.3211
142.1063
140.6822
138.9046
138.3848
133.6307
133.3396
131.2051
130.9141
130.0582
130.0201
129.6354
129.6008
129.0117
128.3256
128.0450
126.7871
125.6194
124.6596
124.5140
121.8043
120.4183
117.1715
114.5311
114.4791
114.1118
114.0287
108.8726
77.1600 CDCl3
35.1042
32.0930
21.6388
21.0740
f1 (ppm)

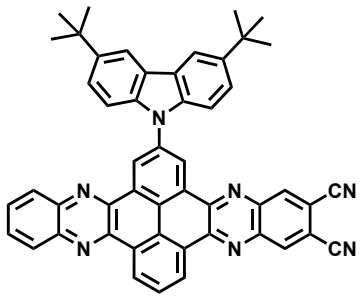

Compound **11c** was purified via recrystallization in a chloroform/ethanol mixture, with a yield of 40%. ^{1}H NMR (600 MHz, $CDCl_3$/TFA = 10/1) δ 10.21 (s, 1H), 10.16 (s, 1H), 10.10 (d, *J* = 7.8 Hz, 1H), 9.77 (d, *J* = 8.0 Hz, 1H), 9.08 (s, 1H), 9.03 (s, 1H), 8.75 (dd, *J* = 8.43, 0.9 Hz, 1H), 8.74 (dd, *J* = 8.43, 0.9 Hz, 1H), 8.50 (t, *J* = 7.9 Hz, 1H), 8.40 (ddd, *J* = 8.5, 6.8, 1.4 Hz, 1H), 8.36 – 8.29 (m, 3H), 7.70 (d, *J* = 8.9 Hz, 2H), 7.62 (d, *J* = 8.0 Hz, 2H), 1.55 (s, 18H). ^{13}C NMR (151 MHz, $CDCl_3$/TFA = 10/1) δ 145.55, 145.31, 145.20, 143.73, 143.11, 143.04, 143.00, 141.10, 138.98, 138.74, 138.72, 137.80, 135.20, 134.74, 134.34, 131.54, 131.47, 130.70, 130.31, 130.25, 130.01, 129.89, 128.89, 128.77, 127.30, 125.92, 124.83, 124.65, 121.88, 121.51, 114.36, 114.34, 114.02, 113.96, 108.90, 35.16, 32.07.

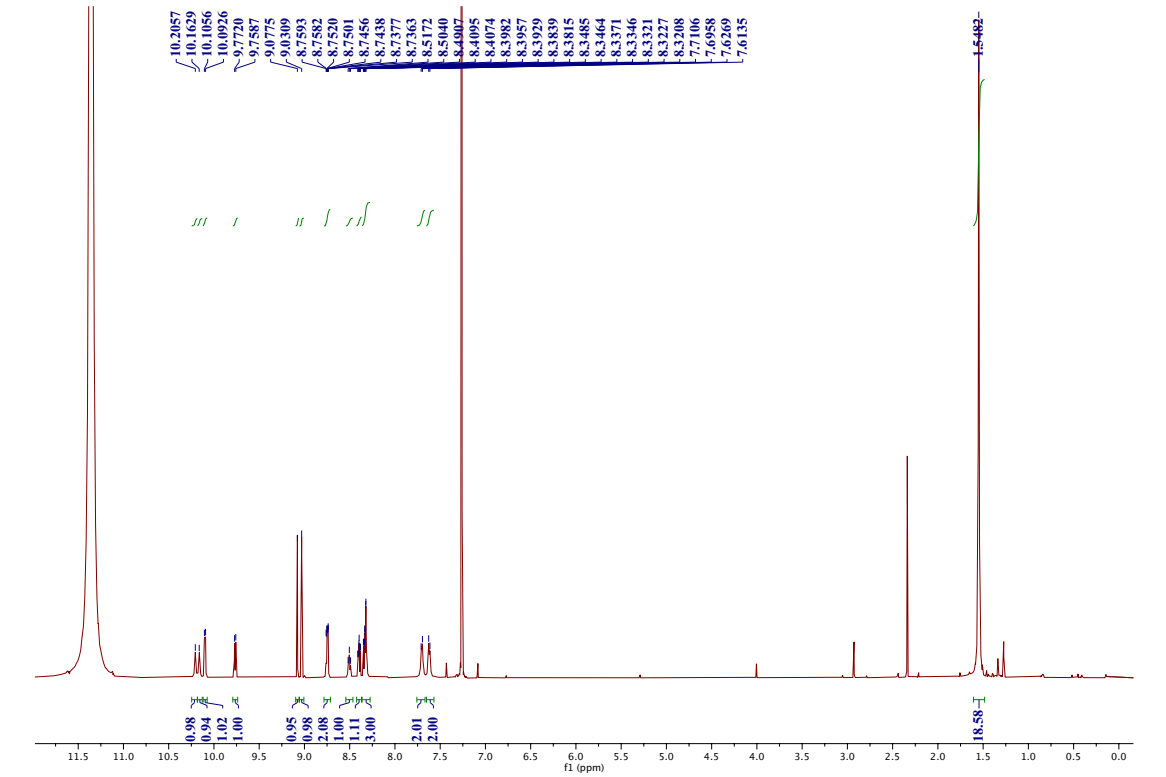
10.2057
10.1629
10.1056
10.0926
9.7720
9.7587
9.0775
9.0309
8.7593
8.7582
8.7520
8.7501
8.7456
8.7438
8.7377
8.7363
8.5172
8.5040
8.4907
8.4095
8.4074
8.3982
8.3957
8.3929
8.3839
8.3815
8.3485
8.3464
8.3371
8.3346
8.3321
8.3227
8.3208
7.7106
7.6958
7.6269
7.6135
1.5482
0.98
0.94
1.02
1.00
0.95
0.98
2.08
1.00
1.11
3.00
2.01
2.00
18.58
f1 (ppm)

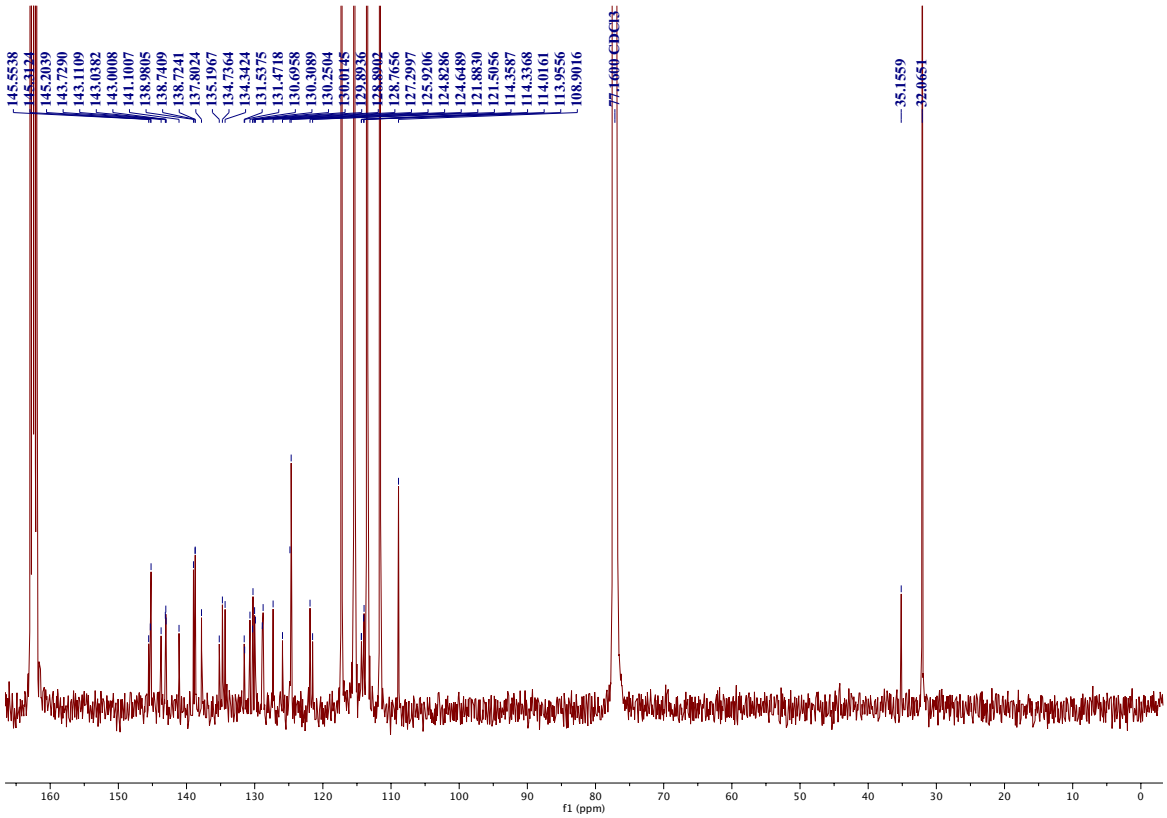
145.5538
145.2124
145.2039
143.7290
143.1109
143.0382
143.0008
141.1007
138.9805
138.7409
138.7241
137.8024
135.1967
134.7364
134.3424
131.5375
131.4718
130.6958
130.3089
130.2504
130.0145
129.8936
128.8902
128.7656
127.2997
125.9206
124.8286
124.6489
121.8830
121.5056
114.3587
114.3368
114.0161
113.9556
108.9016
77.1600 CDCl3
35.1559
32.0651
f1 (ppm)

8. References

[1]N. A. Campbell, Reece, J. B., *Biology*, Pearson Education, Inc., San Francisco **2008**.
[2]A. C. Ferrari, F. Bonaccorso, V. Fal'Ko, K. S. Novoselov, S. Roche, P. Bøggild, S. Borini, F. H. Koppens, V. Palermo, N. Pugno, *Nanoscale* **2015**, 7, 4598.
[3]A. H. Castro Neto, F. Guinea, N. M. R. Peres, K. S. Novoselov, A. K. Geim, *Reviews of Modern Physics* **2009**, 81, 109.
[4]P. Avouris, Z. Chen, V. Perebeinos, *Nature Nanotechnology* **2007**, 2, 605.
[5]N. Martín, N. Tagmatarchis, Q. H. Wang, X. Zhang, *Chemistry – A European Journal* **2020**, 26, 6292.
[6]V. Georgakilas, M. Otyepka, A. B. Bourlinos, V. Chandra, N. Kim, K. C. Kemp, P. Hobza, R. Zboril, K. S. Kim, *Chemical Reviews* **2012**, 112, 6156.
[7]A. C. Ferrari, F. Bonaccorso, V. Fal'ko, K. S. Novoselov, S. Roche, P. Boggild, S. Borini, F. H. Koppens, V. Palermo, N. Pugno, J. A. Garrido, R. Sordan, A. Bianco, L. Ballerini, M. Prato, E. Lidorikis, J. Kivioja, C. Marinelli, T. Ryhanen, A. Morpurgo, J. N. Coleman, V. Nicolosi, L. Colombo, A. Fert, M. Garcia-Hernandez, A. Bachtold, G. F. Schneider, F. Guinea, C. Dekker, M. Barbone, Z. Sun, C. Galiotis, A. N. Grigorenko, G. Konstantatos, A. Kis, M. Katsnelson, L. Vandersypen, A. Loiseau, V. Morandi, D. Neumaier, E. Treossi, V. Pellegrini, M. Polini, A. Tredicucci, G. M. Williams, B. H. Hong, J. H. Ahn, J. M. Kim, H. Zirath, B. J. van Wees, H. van der Zant, L. Occhipinti, A. Di Matteo, I. A. Kinloch, T. Seyller, E. Quesnel, X. Feng, K. Teo, N. Rupesinghe, P. Hakonen, S. R. Neil, Q. Tannock, T. Lofwander, J. Kinaret, *Nanoscale* **2015**, 7, 4598.
[8]G. Bottari, M. Á. Herranz, L. Wibmer, M. Volland, L. Rodríguez-Pérez, D. M. Guldi, A. Hirsch, N. Martín, F. D'Souza, T. Torres, *Chemical Society Reviews* **2017**, 46, 4464.
[9]A. Laurent, *Ann. Chim. Phys* **1837**, 66, 136.
[10]H. A. Favre, W. H. Powell, *Nomenclature of organic chemistry: IUPAC recommendations and preferred names 2013*, Royal Society of Chemistry, **2014**.
[11]E. Clar, in *Mobile Source Emissions Including Policyclic Organic Species*, (Eds: D. Rondia, M. Cooke, R. K. Haroz), Springer Netherlands, Dordrecht **1983**.
[12]K. Fukui, T. Yonezawa, H. Shingu, *The Journal of Chemical Physics* **1952**, 20, 722.
[13]H. Vollmann, H. Becker, M. Corell, H. Streeck, *Justus Liebigs Annalen der Chemie* **1937**, 531, 1.
[14]X. Feng, J.-Y. Hu, X.-F. Wei, C. Redshaw, T. Yamato, *Journal of Molecular Structure* **2015**, 1086, 216.
[15]H. M. Kim, Y. O. Lee, C. S. Lim, J. S. Kim, B. R. Cho, *The Journal of Organic Chemistry* **2008**, 73, 5127.
[16]S. Bernhardt, M. Kastler, V. Enkelmann, M. Baumgarten, K. Müllen, *Chemistry–A European Journal* **2006**, 12, 6117.
[17]N. J. Jeon, J. Lee, J. H. Noh, M. K. Nazeeruddin, M. Gratzel, S. I. Seok, *Journal of the American Chemical Society* **2013**, 135, 19087.
[18]J. J. Chen, I. J. Wang, *Dyes and Pigments* **1995**, 29, 305.
[19]M. Garrido, M. K. Volland, P. W. Münich, L. Rodríguez-Pérez, J. Calbo, E. Ortí, M. Á. Herranz, N. Martín, D. M. Guldi, *Journal of the American Chemical Society* **2020**, 142, 1895.
[20]S. Rajabi, F. Ebrahimi, G. Lole, J. Odrobina, S. Dechert, C. Jooss, F. Meyer, *ACS Catalysis* **2020**, 10, 10614.

[21] V. Mishyn, A. Hugo, T. Rodrigues, P. Aspermair, H. Happy, L. Marques, C. Hurot, R. Othmen, V. Bouchiat, R. Boukherroub, W. Knoll, S. Szunerits, *Sensors & Diagnostics* **2022**, 1, 235.
[22] L. Rafols, S. Torrente, D. Aguilà, V. Soto-Cerrato, R. Pérez-Tomás, P. Gamez, A. Grabulosa, *Organometallics* **2020**, 39, 2959.
[23] N.-W. Wu, J. Zhang, D. Ciren, Q. Han, L.-J. Chen, L. Xu, H.-B. Yang, *Organometallics* **2013**, 32, 2536.
[24] B. Ö. Öztürk, H. Acar, A. Balcı, S. Cihnioğlu, M. Aşkun, S. Karabulut Şehitoğlu, *Dalton Transactions* **2023**, 52, 13587.
[25] K. C. Stylianou, J. Rabone, S. Y. Chong, R. Heck, J. Armstrong, P. V. Wiper, K. E. Jelfs, S. Zlatogorsky, J. Bacsa, A. G. McLennan, C. P. Ireland, Y. Z. Khimyak, K. M. Thomas, D. Bradshaw, M. J. Rosseinsky, *Journal of the American Chemical Society* **2012**, 134, 20466.
[26] Y. Xiao, Y. Qi, X. Wang, X. Wang, F. Zhang, C. Li, *Advanced Materials* **2018**, 30, 1803401.
[27] P. P. Fu, H. M. Lee, R. G. Harvey, *The Journal of Organic Chemistry* **1980**, 45, 2797.
[28] M. Schroeder, *Chemical Reviews* **1980**, 80, 187.
[29] F. G. Oberender, J. A. Dixon, *The Journal of Organic Chemistry* **1959**, 24, 1226.
[30] J. Hu, D. Zhang, F. W. Harris, *The Journal of Organic Chemistry* **2005**, 70, 707.
[31] T. Yamato, M. Fujimoto, A. Miyazawa, K. Matsuo, *Journal of the Chemical Society, Perkin Transactions 1* **1997**, 1201.
[32] T. Yamato, A. Miyazawa, M. Tashiro, *Chemische Berichte* **1993**, 126, 2505.
[33] P. Boldt, D. Bruhnke, *JOURNAL FUR PRAKTISCHE CHEMIE-CHEMIKER-ZEITUNG* **1994**, 336, 110.
[34] H. Lee, R. G. Harvey, *The Journal of Organic Chemistry* **1986**, 51, 2847.
[35] T. Ishiyama, J. Takagi, K. Ishida, N. Miyaura, N. R. Anastasi, J. F. Hartwig, *Journal of the American Chemical Society* **2002**, 124, 390.
[36] M. Shi, C. Peng, X. Zhang, *Small* **2023**, 19, 2301449.
[37] S. Yeşilot, N. Kılıç, S. Sariyer, S. Küçükköylü, A. Kılıç, R. Demir-Cakan, *ACS Applied Energy Materials* **2021**, 4, 12487.
[38] R. Shi, L. Liu, Y. Lu, Y. Li, S. Zheng, Z. Yan, K. Zhang, J. Chen, *Advanced Energy Materials* **2021**, 11, 2002917.
[39] P. García-Arroyo, E. Martínez-Periñán, J. J. Cabrera-Trujillo, E. Salagre, E. G. Michel, J. I. Martínez, E. Lorenzo, J. L. Segura, *Nano Research* **2022**, 15, 3907.
[40] C. Wei, J. Wu, D. Zhang, W. Su, J. Xiao, Z. Cui, *Asian Journal of Organic Chemistry* **2018**, 7, 424.
[41] A. Mateo-Alonso, *Chemical Society Reviews* **2014**, 43, 6311.
[42] R. R. Ernst, *Angewandte Chemie International Edition in English* **1992**, 31, 805.
[43] M. Seah, *Surface and Interface Analysis* **1980**, 2, 222.
[44] F. A. Stevie, C. L. Donley, *Journal of Vacuum Science & Technology A* **2020**, 38.
[45] A. J. Bard, L. R. Faulkner, H. S. White, *Electrochemical Methods: Fundamentals and Applications*, John Wiley & Sons, **2022**.
[46] P. L. Taberna, P. Simon, J. F. Fauvarque, *Journal of the Electrochemical Society* **2003**, 150, A292.
[47] M. F. Dupont, A. F. Hollenkamp, S. W. Donne, *Journal of the Electrochemical Society* **2014**, 161, A648.
[48] B.-A. Mei, O. Munteshari, J. Lau, B. Dunn, L. Pilon, *The Journal of Physical Chemistry C* **2018**, 122, 194.

[49] T. S. Mathis, N. Kurra, X. Wang, D. Pinto, P. Simon, Y. Gogotsi, *Advanced Energy Materials* **2019**, 9, 1902007.
[50] R. Kötz, M. Carlen, *Electrochimica Acta* **2000**, 45, 2483.
[51] C.-L. Liu, W.-S. Dong, G.-P. Cao, J.-R. Song, L. Liu, Y.-S. Yang, *Journal of Electroanalytical Chemistry* **2007**, 611, 225.
[52] I. Yang, S.-G. Kim, S. H. Kwon, M.-S. Kim, J. C. Jung, *Electrochimica Acta* **2017**, 223, 21.
[53] C. Lei, F. Markoulidis, Z. Ashitaka, C. Lekakou, *Electrochimica Acta* **2013**, 92, 183.
[54] C. Portet, G. Yushin, Y. Gogotsi, *Carbon* **2007**, 45, 2511.
[55] Y.-R. Nian, H. Teng, *Journal of Electroanalytical Chemistry* **2003**, 540, 119.
[56] J. Lakowicz, *University of Maryland School of Medicine Baltimore* **2006**, 132.
[57] Y. Shao, M. F. El-Kady, J. Sun, Y. Li, Q. Zhang, M. Zhu, H. Wang, B. Dunn, R. B. Kaner, *Chemical Reviews* **2018**, 118, 9233.
[58] S. Chu, Y. Cui, N. Liu, *Nature Materials* **2017**, 16, 16.
[59] J. M. Gonzalez, J. E. Tomlinson, E. A. Martínez Ceseña, M. Basheer, E. Obuobie, P. T. Padi, S. Addo, R. Baisie, M. Etichia, A. Hurford, A. Bottacin-Busolin, J. Matthews, J. Dalton, D. M. Smith, J. Sheffield, M. Panteli, J. J. Harou, *Nature Sustainability* **2023**, 6, 415.
[60] Z. Fan, J. Yan, T. Wei, L. Zhi, G. Ning, T. Li, F. Wei, *Advanced Functional Materials* **2011**, 21, 2366.
[61] C. Xu, B. Li, H. Du, F. Kang, *Angewandte Chemie International Edition* **2012**, 51, 933.
[62] R. Chen, R. Luo, Y. Huang, F. Wu, L. Li, *Advanced Science* **2016**, 3, 1600051.
[63] K. Xu, *Chemical Reviews* **2004**, 104, 4303.
[64] C. Zhong, Y. Deng, W. Hu, J. Qiao, L. Zhang, J. Zhang, *Chemical Society Reviews* **2015**, 44, 7484.
[65] B. Pal, S. Yang, S. Ramesh, V. Thangadurai, R. Jose, *Nanoscale Advances* **2019**, 1, 3807.
[66] B. Pal, S. G. Krishnan, B. L. Vijayan, M. Harilal, C.-C. Yang, F. I. Ezema, M. M. Yusoff, R. Jose, *Journal of Electroanalytical Chemistry* **2018**, 817, 217.
[67] B. Pal, S. G. Krishnan, B. L. Vijayan, M. Harilal, C. C. Yang, F. I. Ezema, M. M. Yusoff, R. Jose, *Journal of Electroanalytical Chemistry* **2018**, 817, 217.
[68] H. v. Helmholtz, *Annalen der Physik* **1853**, 165, 353.
[69] M. Gouy, *Journal of Physics: Theories and Applications* **1910**, 9, 457.
[70] O. Stern, *Zeitschrift für Elektrochemie und angewandte physikalische Chemie* **1924**, 30, 508.
[71] D. C. Grahame, *Chemical Reviews* **1947**, 41, 441.
[72] H. I. Becker, Google Patents, **1957**.
[73] R. A. Rightmire, Google Patents, **1966**.
[74] T. Z. Guo, D. Zhou, L. X. Pang, S. K. Sun, T. Zhou, J. Z. Su, *Small* **2022**, 18, 2106360.
[75] V. Augustyn, P. Simon, B. Dunn, *Energy & Environmental Science* **2014**, 7, 1597.
[76] S. Fleischmann, J. B. Mitchell, R. C. Wang, C. Zhan, D. E. Jiang, V. Presser, V. Augustyn, *Chemical Reviews* **2020**, 120, 6738.
[77] Y. Q. Jiang, J. P. Liu, *Energy & Environmental Materials* **2019**, 2, 30.
[78] T. S. Mathis, N. Kurra, X. H. Wang, D. Pinto, P. Simon, Y. Gogotsi, *Advanced Energy Materials* **2019**, 9.
[79] Y. Gogotsi, R. M. Penner, *ACS Nano* **2018**, 12, 2081.
[80] Z. H. Gan, J. Y. Yin, X. Xu, Y. H. Cheng, T. Yu, *ACS Nano* **2022**, 16, 5131.
[81] P. Simon, Y. Gogotsi, B. Dunn, *Science* **2014**, 343, 1210.
[82] A. Li, M. Yi, S. M. Zhao, M. X. Luan, J. B. Hu, *Batteries & Supercaps* **2022**, 5.
[83] S. Zhang, N. Pan, *Advanced Energy Materials* **2015**, 5, 1401401.

[84] Reenu, Sonia, L. Phor, A. Kumar, S. Chahal, *Journal of Energy Storage* **2024**, 84, 110698.
[85] K. K. Patel, T. Singhal, V. Pandey, T. P. Sumangala, M. S. Sreekanth, *Journal of Energy Storage* **2021**, 44, 103366.
[86] X. F. Zhang, Z. Y. Xiao, X. F. Liu, P. Mei, Y. K. Yang, *Renewable & Sustainable Energy Reviews* **2021**, 147.
[87] M. Shi, P. Das, Z.-S. Wu, T.-g. Liu, X. Zhang, *Advanced Materials* **2023**, 35, 2302199.
[88] H. Q. Yang, J. Lee, J. Y. Cheong, Y. F. Wang, G. G. Duan, H. Q. Hou, S. H. Jiang, I. Kim, *Energy & Environmental Science* **2021**, 14, 4228.
[89] C. Peng, X. Zhang, *Chemistry* **2021**, 3, 873.
[90] Q. Wu, Y. Q. Sun, H. Bai, G. Q. Shi, *Physical Chemistry Chemical Physics* **2011**, 13, 11193.
[91] H. Zhou, A. Uysal, D. M. Anjos, Y. Cai, S. H. Overbury, M. Neurock, J. K. McDonough, Y. Gogotsi, P. Fenter, *Advanced Materials Interfaces* **2015**, 2.
[92] M. Boota, M. Bécuwe, Y. Gogotsi, *ACS Applied Energy Materials* **2020**, 3, 3144.
[93] J. Clayden, Nick Greeves, and Stuart Warren., *Organic Chemistry*, Oxford University Press., London, England **2012**.
[94] L. Jiao, F. Q. Ma, X. T. Wang, Z. M. Li, Z. A. Hu, Q. Yin, *ACS Applied Energy Materials* **2021**, 4, 7811.
[95] M. Shi, C. Peng, X. Zhang, *Small* **2023**, 19, 2301449.
[96] Y. Y. Ma, Z. W. Guo, X. L. Dong, Y. G. Wang, Y. Y. Xia, *Angewandte Chemie-International Edition* **2019**, 58, 4622.
[97] X. Yang, Y. Y. Yang, Q. C. Zhang, X. T. Wang, Y. F. An, B. S. Guo, Z. G. Hu, H. Y. Wu, *RSC Advances* **2017**, 7, 48341.
[98] C. Wang, F. Liu, J. Chen, Z. Yuan, C. Liu, X. Zhang, M. Xu, L. Wei, Y. Chen, *Energy Storage Materials* **2020**, 32, 448.
[99] K. Li, X. Wang, S. Li, P. Urbankowski, J. Li, Y. Xu, Y. Gogotsi, *Small* **2020**, 16, 1906851.
[100] M. Boota, Y. Gogotsi, *Advanced Energy Materials* **2019**, 9, 1802917.
[101] M. Hou, M. Xu, Y. Hu, B. Li, *Electrochimica Acta* **2019**, 313, 245.
[102] X. Chen, F. Su, Q. Zhou, J. Sun, *Surfaces and Interfaces* **2021**, 26, 101393.
[103] J. Zhou, Q. Kang, S. Xu, X. Li, C. Liu, L. Ni, N. Chen, C. Lu, X. Wang, L. Peng, X. Guo, W. Ding, W. Hou, *Nano Research* **2022**, 15, 285.
[104] L. Xu, Y. Zhang, W. Zhou, F. Jiang, H. Zhang, Q. Jiang, Y. Jia, R. Wang, A. Liang, J. Xu, *ACS Applied Materials & Interfaces* **2020**, 12, 45202.
[105] Z. Song, Y. Qian, M. L. Gordin, D. Tang, T. Xu, M. Otani, H. Zhan, H. Zhou, D. Wang, *Angewandte Chemie* **2015**, 127, 14153.
[106] R. B. Choudhary, S. Ansari, B. Purty, *Journal of Energy Storage* **2020**, 29, 101302.
[107]F. Fusalba, P. Gouérec, D. Villers, D. Bélanger, *Journal of the Electrochemical Society* **2001**, 148, A1.
[108] Y. T. Tan, F. Ran, L. R. Wang, L. B. Kong, L. Kang, *Journal of Applied Polymer Science* **2013**, 127, 1544.
[109] D. Dhawale, A. Vinu, C. Lokhande, *Electrochimica Acta* **2011**, 56, 9482.
[110] R. Oraon, A. De Adhikari, S. K. Tiwari, S. Bhattacharyya, G. C. Nayak, *RSC Advances* **2016**, 6, 64271.
[111] G. A. Snook, P. Kao, A. S. Best, *Journal of Power Sources* **2011**, 196, 1.
[112] A. M. Bryan, L. M. Santino, Y. Lu, S. Acharya, J. M. D'Arcy, *Chemistry of Materials* **2016**, 28, 5989.

[113] C. Wang, R. Li, Y. Zhu, Y. Wang, Y. Lin, L. Zhong, H. Chen, Z. Tang, H. Li, F. Liu, C. Zhi, H. Lv, *Advanced Energy Materials* **2024**, 14, 2302495.
[114] S. Saxena, T. A. Tyson, S. Shukla, E. Negusse, H. Chen, J. Bai, *Applied Physics Letters* **2011**, 99.
[115] Y.-R. Shen, **1984**.
[116] A. Dutt, A. Mohanty, A. L. Gaeta, M. Lipson, *Nature Reviews Materials* **2024**, 9, 321.
[117] U. Keller, *Nature* **2003**, 424, 831.
[118] S. R. Marder, D. N. Beratan, L.-T. Cheng, *Science* **1991**, 252, 103.
[119] C. Xu, F. W. Wise, *Nature Photonics* **2013**, 7, 875.
[120] W. R. Zipfel, R. M. Williams, W. W. Webb, *Nature Biotechnology* **2003**, 21, 1369.
[121] T. Y. Choi, C. P. Grigoropoulos, *Journal of Applied Physics* **2002**, 92, 4918.
[122] X. Xue, H. Wang, Y. Han, H. Hou, *Dalton Transactions* **2018**, 47, 13.
[123] E. Garmire, *Optics Express* **2013**, 21, 30532.
[124] L. R. Dalton, P. A. Sullivan, D. H. Bale, *Chemical Reviews* **2010**, 110, 25.
[125] P. A. Sullivan, L. R. Dalton, *Accounts of Chemical Research* **2010**, 43, 10.
[126] P. G. Lacroix, I. Malfant, C. Lepetit, *Coordination Chemistry Reviews* **2016**, 308, 381.
[127] G. New, *Introduction to Nonlinear Optics*, Cambridge University Press, Cambridge **2011**.
[128] S. R. Marder, J. W. Perry, *Advanced Materials* **1993**, 5, 804.
[129] S. Di Bella, *Chemical Society Reviews* **2001**, 30, 355.
[130] S. Nath, A. Puthukkudi, J. Mohapatra, B. P. Biswal, *Angewandte Chemie International Edition* **2023**, 62, e202218974.
[131] A. Autere, H. Jussila, Y. Dai, Y. Wang, H. Lipsanen, Z. Sun, *Advanced Materials* **2018**, 30, 1705963.
[132] Y. Yan, Y. Yuan, B. Wang, V. Gopalan, N. C. Giebink, *Nature Communications* **2017**, 8, 14269.
[133] P. Franken, A. E. Hill, C. e. Peters, G. Weinreich, *Physical Review Letters* **1961**, 7, 118.
[134] W. Wu, G. Xu, C. Li, G. Yu, Y. Liu, C. Ye, J. Qin, Z. Li, *Chemistry – A European Journal* **2013**, 19, 6874.
[135] V. L. Brudny, B. S. Mendoza, W. L. Mochán, *Physical Review B* **2000**, 62, 11152.
[136] C. S. Tian, Y. R. Shen, *Surface Science Reports* **2014**, 69, 105.
[137] H. Shang, Z. Ding, Y. Shen, B. Yang, M. Liu, S. Jiang, *Chemical Science* **2020**, 11, 2169.
[138] W. Kaiser, C. G. B. Garrett, *Physical Review Letters* **1961**, 7, 229.
[139] F. Dutto, C. Raillon, K. Schenk, A. Radenovic, *Nano Letters* **2011**, 11, 2517.
[140] D. Wei, C. Wang, H. Wang, X. Hu, D. Wei, X. Fang, Y. Zhang, D. Wu, Y. Hu, J. Li, S. Zhu, M. Xiao, *Nature Photonics* **2018**, 12, 596.
[141] J. Jerphagnon, S. K. Kurtz, *Physical Review B* **1970**, 1, 1739.
[142]Y. Mori, I. Kuroda, S. Nakajima, T. Sasaki, S. Nakai, *Applied Physics Letters* **1995**, 67, 1818.
[143] M. Feng, H. Zhan, L. Miao, *ACS Applied Materials & Interfaces* **2010**, 2, 1129.
[144] H. Yu, J. Young, H. Wu, W. Zhang, J. M. Rondinelli, S. Halasyamani, *Advanced Optical Materials* **2017**, 5, 1700840.
[145] R. C. Eckardt, H. Masuda, Y. X. Fan, R. L. Byer, *IEEE Journal of Quantum Electronics* **1990**, 26, 922.
[146] F. Bonaccorso, Z. Sun, T. Hasan, A. C. Ferrari, *Nature Photonics* **2010**, 4, 611.
[147] S. Kumar, M. Anija, N. Kamaraju, K. S. Vasu, K. S. Subrahmanyam, A. K. Sood, C. N. R. Rao, *Applied Physics Letters* **2009**, 95.
[148] Z. Sun, A. Martinez, F. Wang, *Nature Photonics* **2016**, 10, 227.

[149] S. Yu, X. Wu, Y. Wang, X. Guo, L. Tong, *Advanced Materials* **2017**, 29, 1606128.
[150] O. Ostroverkhova, *Handbook of organic materials for optical and (opto) electronic devices: properties and applications*, Elsevier, **2013**.
[151] J. Xu, S. Semin, D. Niedzialek, P. H. J. Kouwer, E. Fron, E. Coutino, M. Savoini, Y. Li, J. Hofkens, H. Uji-I, D. Beljonne, T. Rasing, A. E. Rowan, *Advanced Materials* **2013**, 25, 2084.
[152] M. Duguay, S. Shapiro, P. Rentzepis, *Physical Review Letters* **1967**, 19, 1014.
[153] M. Bass, D. Bua, R. Mozzi, R. Monchamp, *Applied Physics Letters* **1969**, 15, 393.
[154] J. Xu, X. Liu, J. Lv, M. Zhu, C. Huang, W. Zhou, X. Yin, H. Liu, Y. Li, J. Ye, *Langmuir* **2008**, 24, 4231.
[155] R. Hu, E. Lager, A. Aguilar-Aguilar, J. Liu, J. W. Y. Lam, H. H. Y. Sung, I. D. Williams, Y. Zhong, K. S. Wong, E. Peña-Cabrera, B. Z. Tang, *The Journal of Physical Chemistry C* **2009**, 113, 15845.
[156] Z. Chen, G. Gallo, V. A. Sawant, T. Zhang, M. Zhu, L. Liang, A. Chanthapally, G. Bolla, H. S. Quah, X. Liu, *Angewandte Chemie International Edition* **2020**, 59, 833.
[157] A. J.-T. Lou, S. Righetto, C. Barger, C. Zuccaccia, E. Cariati, A. Macchioni, T. J. Marks, *Journal of the American Chemical Society* **2018**, 140, 8746.
[158] J. d. Oudar, *The Journal of Chemical Physics* **1977**, 67, 446.
[159] C. Teng, A. Garito, *Physical Review B* **1983**, 28, 6766.
[160] A. Ulman, *The Journal of Physical Chemistry* **1988**, 92, 2385.
[161] F. Terenziani, C. Katan, E. Badaeva, S. Tretiak, M. Blanchard-Desce, *Advanced Materials* **2008**, 20, 4641.
[162] V. G. Sreeja, G. Vinitha, R. Reshmi, E. I. Anila, M. K. Jayaraj, *Optical Materials* **2017**, 66, 460.
[163] G.-K. Lim, Z.-L. Chen, J. Clark, R. G. S. Goh, W.-H. Ng, H.-W. Tan, R. H. Friend, P. K. H. Ho, L.-L. Chua, *Nature Photonics* **2011**, 5, 554.
[164] Z. Sun, T. Hasan, F. Torrisi, D. Popa, G. Privitera, F. Wang, F. Bonaccorso, D. M. Basko, A. C. Ferrari, *ACS Nano* **2010**, 4, 803.
[165] Q. Bao, H. Zhang, Y. Wang, Z. Ni, Y. Yan, Z. X. Shen, K. P. Loh, D. Y. Tang, *Advanced Functional Materials* **2009**, 19, 3077.
[166] L. Fu, H. Li, Y. Fang, Z. Guan, Z. Wei, N. Shan, F. Liu, Y. Zhao, M. Zhang, Z. Huang, M. G. Humphrey, C. Zhang, *Nano Research* **2023**, 16, 5909.
[167] A. Ganesan, A. Husain, M. Sebastian, S. Makhseed, *Dyes and Pigments* **2021**, 196, 109794.
[168] J. A. Letizia, S. Cronin, R. P. Ortiz, A. Facchetti, M. A. Ratner, T. J. Marks, *Chemistry – A European Journal* **2010**, 16, 1911.
[169] S.-i. Kawano, M. Baumgarten, D. Chercka, V. Enkelmann, K. Müllen, *Chemical Communications* **2013**, 49, 5058.
[170] S. More, R. Bhosale, S. Choudhary, A. Mateo-Alonso, *Organic Letters* **2012**, 14, 4170.
[171] S. More, R. Bhosale, A. Mateo-Alonso, *Chemistry – A European Journal* **2014**, 20, 10626.
[172] P. Zhou, M. Nazari Haghighi Pashaki, H.-M. Frey, A. Hauser, S. Decurtins, A. Cannizzo, T. Feurer, R. Häner, U. Aschauer, S.-X. Liu, *Chemical Science* **2023**, 14, 12715.
[173] L. Ueberricke, I. Ciubotaru, F. Ghalami, F. Mildner, F. Rominger, M. Elstner, M. Mastalerz, *Chemistry – A European Journal* **2020**, 26, 11634.